

A multiwavelength study of  $170\,\mu\text{m}$  selected sources

by

Anna Sajina

B.Sc., The University of British Columbia, 2000

A THESIS SUBMITTED IN PARTIAL FULFILMENT OF  
THE REQUIREMENTS FOR THE DEGREE OF

MASTER OF SCIENCE

in

THE FACULTY OF GRADUATE STUDIES

(Department of Physics and Astronomy)

We accept this thesis as conforming  
to the required standard

THE UNIVERSITY OF BRITISH COLUMBIA

October 9, 2002

© Anna Sajina, 2002

In presenting this thesis in partial fulfilment of the requirements for an advanced degree at the University of British Columbia, I agree that the Library shall make it freely available for reference and study. I further agree that permission for extensive copying of this thesis for scholarly purposes may be granted by the head of my department or by his or her representatives. It is understood that copying or publication of this thesis for financial gain shall not be allowed without my written permission.

Department of Physics and Astronomy

The University Of British Columbia  
Vancouver, Canada

Date Oct. 11, 2002

# ABSTRACT

We present results from sub-mm observations of sources selected from the *ISO* FIRBACK (Far IR BACKground) survey, along with UKIRT near-IR imaging of a sub-sample. This gives valuable insight to the brightest 10% of galaxies which contribute to the Cosmic Infrared Background (CIB). We estimate the photometric redshifts and luminosities of these sources by fitting their Spectral Energy Distributions (SEDs). The data appear to show a bimodal galaxy distribution, with normal star-forming galaxies at  $z \simeq 0$ , and the  $z \sim 0.4\text{--}0.9$  tail of a much more luminous population. These are similar to the ultraluminous infrared galaxies which are found to evolve rapidly with redshift in other surveys. We are biased away from much higher redshift objects by the detectability threshold of FIRBACK. Nevertheless, the handful of  $z \sim 0.5$  sources which we identify are likely to be the low- $z$  counterparts of the typically higher- $z$  sources found in blank field sub-mm observations. The sources we identify here have the virtue of being relatively easy to study in the optical. Hence their detailed investigation could help elucidate the nature of the sub-mm bright galaxies.

# CONTENTS

<b>Abstract</b> . . . . .	ii
<b>Contents</b> . . . . .	iii
<b>List of Tables</b> . . . . .	v
<b>List of Figures</b> . . . . .	vi
<b>Acknowledgements</b> . . . . .	xii
<b>1 Introduction</b> . . . . .	1
1.1 The Cosmic Infrared Background . . . . .	1
1.2 The Multiwavelength Approach . . . . .	5
<b>2 The Data</b> . . . . .	8
2.1 Sample . . . . .	8
2.2 The instrument . . . . .	9
2.3 SCUBA sub-mm observations . . . . .	13
2.4 SCUBA data reduction . . . . .	16
2.5 UKIRT near-IR observations . . . . .	21
<b>3 Results &amp; Analysis</b> . . . . .	25
3.1 Assembling the multiwavelength data . . . . .	25
3.2 Linear Correlations . . . . .	29
3.3 Sub-mm/Radio redshifts . . . . .	37
3.4 Sub-mm vs. near-IR . . . . .	38
3.5 SED fits . . . . .	44

3.6	Luminosity and SFR . . . . .	46
4	A Model . . . . .	53
5	Summary & Discussion . . . . .	63
5.1	Comparison with related studies . . . . .	67
5.2	Bimodality . . . . .	68
5.3	Comparison with evolutionary models . . . . .	69
5.4	Future Direction . . . . .	72
	Bibliography . . . . .	74
A	Photometry with SCUBA . . . . .	79
B	Cosmology . . . . .	83

# LIST OF TABLES

2.1	Source coordinates . . . . .	22
2.1	<i>continued</i> ... . . . .	23
2.2	Calibration values . . . . .	24
3.1	Multiwavelength data for our sample <sup>a</sup> . . . . .	26
3.1	<i>continued</i> ... . . . .	27
3.2	Results for the linear fits to the data . . . . .	31
3.3	The sub-mm/radio spectral indices and derived redshifts . . . . .	39
3.3	<i>continued</i> ... . . . .	40
3.4	$\chi^2$ -range occupancy for various $\beta$ fits. . . . .	45
3.5	Fit results for $\beta = 1.5$ . . . . .	48
3.5	<i>continued</i> ... . . . .	49
3.6	Fit results for the higher- $z$ sources <sup>a</sup> . . . . .	50
3.7	Estimating the Star Formation Rates <sup>a</sup> . . . . .	52

# LIST OF FIGURES

- 1.1 This figure [58] is a compilation showing the different extragalactic backgrounds including the CIB (called FIB here for Far-Infrared Background). Notice in particular that the power output in the far-IR spectral region is comparable to that in the optical region. . . . . 4
- 2.1 Shows the VLA coverage of the ELAIS-N1 field where our sample is located. Here the asterixes show the ISOPHOT pointings while the circles are  $\sim 30\%$  sensitivity of their centers for the VLA pointings (the absolute radio sensistivity varies from region to region)[15]. . . . . 10
- 2.2 This roughly estimates the selection cut off of the FIRBACK survey in  $(L, z)$  space. The solid line is the  $3\sigma$  limis ( $=135$  mJy), the dashed line is the  $4\sigma$  limit ( $=180$  mJy). The thin lines roughly estimate the region of influence of the radio selection. See text for details. . . . . 11
- 2.3 Distribution of the  $S_{170}/S_{1.4\text{GHz}}$  ratio. The solid histogram represents all the sources from the FIRBACK catalogue which have been observed in the radio. The dashed histogram is our sample. The dotted line shows our high- $z$  candidates (discussed in Chapter 3). . . . . 12
- 2.4 This shows the performance of the new SCUBA wide-band filters measured in the winter of 2000 compared to the old filters. Notice in particular the dramatic improvement in the  $450\text{ }\mu\text{m}$  filter (30-40% depending on the weather). The black curve is the atmospheric transmission on Mauna Kea (1 mm PWV=precipitative water vapour). This figure was taken from the JCMT website. The filters were measured by D.Naylor and W.Holland. 14

- 2.5 The SCUBA arrays (courtesy of the JCMT website ). Here shown is both the physical scale of the arrays ( $\sim 25$  mm) as well as the field of view ( $\sim 2.3$  arcmin). Note that the closely packed arrays shown here are misleading – the arrays are in fact highly undersampled. Using the basic jiggle mode of observing requires 64-point jiggles to create a fully sampled map in both bands (the spacing between 2 jiggle points is roughly  $2''$ ). The photometry mode, that we use, involves a 9-point jiggle pattern with spacings of  $1''$ . This is much more efficient at quickly reaching the desired SNR in a given bolometer, but the other bolometers produce a very undersampled map. . . . . 15
- 2.6 Relations between optical depths derived from 26 skydip observations in 2001 (note the weighting towards grade 1 weather). The left hand panels show the entire range, while the right hand panels zoom to the grade 1 data ( $\tau_{\text{CSO}} < 0.05$ ) only. Here the dashed lines are the standard relations [1], while the solid lines are simple linear fits to our data (the same fit is shown in both columns). The two are sufficiently similar overall, considering the uneven weighting, and the inclusion of outliers. However, the relations with the CSO  $\tau$  seem to be shallower for the grade 1 data than the single slope relation, which may be due to the uncertainty in  $\tau_{\text{CSO}}$ . . . . . 18
- 2.7 This shows the percentage error in the flux estimate as a function of optical depth  $\tau$ . Here crosses are  $450\ \mu\text{m}$  and stars are  $850\ \mu\text{m}$  data. The airmass is 1.3 (i.e.  $y$ -axis scales as  $\sim A/1.3$ ). The fit is  $y = -0.58 + 5.24\tau - 6.97\tau^2 + 5.56\tau^3$ . Notice that our May 2001 data is off the scale here in  $450\ \mu\text{m}$ , and that with the above relation a  $\tau \sim 3$  gives roughly 100% error. This figure is reproduced from [25]. . . . . 19
- 3.1 The available UKIRT  $K$ -band images – centered on the radio positions. These images are about  $15'' \times 15''$ , or roughly one SCUBA FWHM  $850\ \mu\text{m}$  beam size. The exception is N1-004 where the SCUBA beam is the white circle, as the galaxy itself is larger than this. . . . . 28



- 3.2 This figure is meant to illustrate, in their most obvious cases, the systematic effects that must be kept in mind when trying to interpret the data at hand. Both images are roughly the size of ISO's beam. On the left is N1-004 with the SCUBA 850  $\mu\text{m}$  beam shown to the side (the 450  $\mu\text{m}$  one is about half of that). On the right is N1-008 with the positions of the two radio detections indicated. Our observation is for the stronger of the two – a 3.0 mJy radio source. Notice that the other radio detection (0.3 mJy) has a fainter near-IR counterpart which potentially could be a higher- $z$  source. We will explore this further with upcoming observations. . . . . 30
- 3.3 The scatter plots with their fits and  $\pm 1\sigma$  scatter. The fit parameters are given in Table 3.2. Notice that the order here is: the first column is mainly sensitive to the location of the thermal peak, the second column to the sub-mm slope, and the third column to the trough between the thermal and non-thermal parts of the SED. The error bars are representative for our data. . . . . 32
- 3.4 The histogram is the result of 1000 Monte Carlo simulations of the sub-mm fluxes of our sample. The dotted line shows the actual value of  $\chi^2$  for the observations. Only about  $\sim 2\%$  of the simulations have a value this low (note that the binning is too crude to show that clearly). . . . . 34
- 3.5 The shows the best fit  $[\beta, T/(1+z)]$  combined from the 170/450 and 450/850 slopes, which is [1.5, 31 K] along with the 68, 90, and 95% confidence levels. Notice that  $\beta$  is more poorly constrained. We exclude N1-001, N1-002, N1-034, and N1-059 from the fit due to their discrepant colours. . . . . 36

- 3.6 The sub-mm/radio spectral index as a redshift indicator. The thick solid line is the relation based on the SLUGS sample (104 galaxies - IRAS selected), with the dashed lines being its  $\pm 1\sigma$  envelope. The thin solid line is the standard CY relation [8] (17 galaxies - IRAS and NRAO selection) with dotted  $\pm 1\sigma$  envelope. The circles are 5 galaxies from our sample with spectroscopic redshifts. . . . . 41
- 3.7  $S_{850}$  vs  $K$  magnitude for our sample (crosses and circles). The filled squares and  $K$ -band upper limits are from the lens survey of Smail et al. [61], while the pentagons are from the UK 8mJy survey [40]. The circles are our high- $z$  candidates which populate a similar region to these SCUBA survey sources. The lines are the results from fitting a model to the 6 sources where  $z_{\text{spec}}$  is available (see text) and are labelled with redshift. The bottom panel shows the  $K$ - $z$  relationship obtained above (solid, for  $S_{850}=5$  mJy), compared with the Willot et al. [66] relation for radio galaxies (dashed). The error bar in the lower right-hand corner is a representative one for our measurements. . . . . 43
- 3.8 The SED fits for our sample with  $\beta = 1.5$ . The  $x,y$ -ranges in all panels are the same (shown in the labels), and the sources are arranged with decreasing  $170\mu\text{m}$  flux. The IRAS  $100\mu\text{m}$  point is not used in the fit. For the sake of clarity, we rescale the flux via  $(\lambda/170\mu\text{m})^2$ . . . . . 47
- 4.1 This is the luminosity function used for our models and its evolution with redshift. The dashed line is a non-evolving cold, dusty galaxy population, while the dotted line is an evolving ULIG population - the solid line is the sum of the two. See text for details. . . . . 55

4.2	This shows the cold galaxy template (solid) compared with the starburst galaxy template (dashed) at the same luminosity ( $\sim 10^{11} L_{\odot}$ ). These were used in our model, but are shown here also as an illustration of the effect of cold dust on the SED shape. These templates are the work of Guilaine Lagache and are used in her model [45]. . . . .	57
4.3	This shows the starburst galaxy template for a $L \sim 10^{12} L_{\odot}$ galaxy. The template is evolved with redshift – from top to bottom $z=0.1, 0.5, 1.0, 3.0$ , and $5.0$ . Notice that this figure also illustrates the negative $k$ -correction at $850 \mu\text{m}$ (see next figure). . . . .	58
4.4	Here we plot the $850 \mu\text{m}$ flux vs. redshift for a $4 \times 10^{12} L_{\odot}$ starburst (template) galaxy. This serves the double purpose of illustrating the effect of the negative $k$ -correction at $850 \mu\text{m}$ , and predicting what our 5 higher- $z$ sources would look like at different redshifts. We cut the curve at $z = 0.5$ for scaling purposes. . . . .	59
4.5	The result of our model for the predicted number counts at $170 \mu\text{m}$ with limiting flux of $135 \text{ mJy}$ ( $=3\sigma$ for FIRBACK) . . . . .	60
4.6	The result of our model for the predicted number counts at $850 \mu\text{m}$ with limiting flux of $3.5 \text{ mJy}$ ( $=3\sigma$ for our sample) . . . . .	61
5.1	Here we test the hypothesis of our sample being bimodal by comparing the $\chi^2$ of a single-line fit for the entire sample (right panel) to a two-line fit to each sub-sample (left panel). The dashed lines are $\pm 1\sigma$ where $\sigma$ is the rms scatter in the $y$ -direction. Notice that, apart from N1-048, even with the single-line fit to the entire sample, our high- $z$ candidates are $> 2\sigma$ away from the best-fit line. . . . .	70
5.2	One example of redshift contributions to the CIB. Here the dot-dashed line represents normal, starforming galaxies, the dotted line is the ULIGs, and the dashed line is the LIGs (reproduced from Chary & Elbaz 2001 [14]).	71

A.1	This is an example of the raw bolometer variances which are used to select the bad bolometers. Here, any bolometer above the dashed line ( $=1.25\sigma_{\text{array}}$ ) is excluded from the sky calculation. Note that since, the sky level is later estimated as a weighted mean, the effect of the outliers is reduced. . . . .	80
A.2	The upper panel shows the extinction-corrected timestream of the central bolometer. The middle panel is the weighted mean of all the bolometers (excluding those containing signal or excessive variance). The lower panel is the residual after subtracting the middle from the top. Notice that the vertical scales are the same in each case. . . . .	82
B.1	The effects of different cosmological models on the luminosity distance estimation. In terms of $[\Omega_{\text{tot}}, \Omega_{\Lambda}, \Omega_{\text{M}}]$ , the solid line is $[1, 0.7, 0.3]$ , while the dashed line is $[1, 0, 1]$ . Here $H_0=75 \text{ kms}^{-1}\text{Mpc}^{-1}$ . . . . .	85
B.2	The volume element. . . . .	86

## *Acknowledgements*

This thesis was done under the supervision of Douglas Scott and with the collaboration of (in alphabetical order) Colin Borys, Scott Chapman, Hervé Dole, Mark Halpern, and Guilaine Lagache who all contributed to this work with useful discussions, and suggestions. In particular thanks go to Scott Chapman who provided the near-IR data (and the section on UKIRT observations), Guilaine Lagache who provided the galaxy templates and whose models inspire most of Chapter 4, and Mark Halpern who pointed out the problem with the sub-mm errors. Special thanks goes to Douglas Scott for his critical reading of the text, which greatly improved this thesis.

# CHAPTER 1

## INTRODUCTION

### 1.1 The Cosmic Infrared Background

What makes up the Cosmic Infrared Background (CIB) (Fig. 1.1) detected from the *COBE*-FIRAS data [53, 31, 46, 47, 35, 26, 32]? This remains an open question, and details of galaxy types, their redshift distribution, and how they appear in other wavebands, remain sketchy. The FIRBACK (Far IR BACKground) survey [54, 21] addressed this question by performing some of the deepest blank field *ISO* surveys near the peak of that radiation at  $170\ \mu\text{m}$ . About 200 sources were detected above  $3\sigma$  ( $=135\ \text{mJy}$ ) accounting for about 7% of the background flux.

In general far-IR sources such as the FIRBACK ones sample the low-to-moderate redshift regime, and thus provide a link between the local Universe and high- $z$  sources, such as the SCUBA-bright ‘blank-sky’ population. Understanding the nature of these sources, their emission mechanisms, and their dust properties is crucial to our understanding of galaxy formation and evolution from high redshift until today. This in turn informs us about the cosmic background, as well as the nuclear activities, star formation distributions, and the role of dust obscuration in star formation through a large fraction of the history of the Universe.

It has become increasingly clear that such questions of global galaxy formation cannot be adequately addressed without turning to IR/sub-mm wavelengths. Much of the star formation history is hidden from us at shorter wavelengths by dust obscuration. The result is that up to a 2/3 contribution to the total integrated light from the UV to the sub-mm is in the FIR/sub-mm region [26, 34]. In order to better understand the sources detected by FIRBACK we have been carrying out follow-up observations with SCUBA at  $450\ \mu\text{m}$  and  $850\ \mu\text{m}$ . Selection from *ISO*  $170\ \mu\text{m}$  ( $S_{170} > 135\ \text{mJy}$ ) blank sky surveys,

means that a strong bias away from high- $z$  objects is present, although we expect to detect objects out to  $z \simeq 1$  (see Fig. 2.1). The FIRBACK galaxies represent the brightest contributors to the CIB, and are a different selection than SCUBA-selected galaxies. ‘Blank-sky’ sub-mm bright galaxies, although so far accounting for up to 50% of the *sub-mm* background (e.g.[17]), make up an insignificant fraction of the total CIB which is primarily accounted for by more nearby ( $z < 1.5$ ) sources [14, 28]. The combination of far-IR and sub-mm observations is thus very powerful in establishing a link between high- $z$  dusty starbursts and their local counterparts.

*IRAS* revealed a new population of heavily dust-obscured galaxies with luminosities as high as  $L_{\text{IR}} \geq 10^{12} L_{\odot}$  [62], consistent with high rates of star formation. These are the Ultraluminous Infrared Galaxies (ULIGs) believed to be the interaction/merger of two spiral galaxies (e.g.[55]), with the stage of the merger plausibly being related to the dust temperature and luminosity. Observations reveal a dramatic rise in the relative (to the local Universe) importance of ULIGs in the past, consistent with hierarchical structure formation scenarios (e.g.[48, 3], and references therein). In this sense, a popular scenario involves an evolutionary sequence of duration of order  $10^8$  years, involving increasing dust temperature ( $T_d=20$  to  $50$  K), accompanied by rising IR luminosity ( $10^{10}$  to  $10^{12} L_{\odot}$ ), and with the related phenomenon of the formation of a massive, nuclear black hole. In this scenario, there are two competing heating sources in ULIGs – star formation ( $\sim 100 M_{\odot} \text{yr}^{-1}$ ), and accretion onto the central black hole (i.e. AGN activity). The second contribution appears to be necessary to explain the highest luminosity ULIGs, which would otherwise require implausibly large ( $> 1000 M_{\odot} \text{yr}^{-1}$ ) SFRs. However, the fractional contribution of AGN [29, 37, 30] is hard to assess as, if present at all, the majority are likely to be buried in the dust associated with the surrounding starbursting region. Investigations into AGN contributions have involved both observations of nearby ULIGs [19, 39], and searches for X-ray detectability [2]. While the precise fraction is still debated, it is generally accepted that the bulk of the far-IR/sub-mm background is due to the emission by dust principally heated by star formation. The range of temperatures, emissivity indices and how they correlate with luminosity and AGN activity, are still

open questions. In addition there is the possibility of more than one significant dust component in some galaxies [23].

Using long wavelength data alone, it has been difficult to distinguish between cooler local starbursts and warmer, more luminous sources at higher  $z$ . This is because the spectral energy distributions (SEDs), for a fixed emissivity index  $\beta$ , are degenerate in the parameter combination  $(1+z)/T_d$ . There are additional complications of course caused by variations in  $\beta$ ,  $T_d$ , and luminosity, changing the shape of the SED. A similar degeneracy exists when trying to derive the photometric redshifts from the well-known sub-mm/radio relation [4]. For example a cooler, starforming galaxy will have different thermal and non-thermal spectral indices from a warmer galaxy with an AGN contribution. Blindly applying the same values to both will then make the cooler galaxy look warmer and at higher- $z$  than it is in reality. Fundamentally, our understanding of dust in extragalactic sources, its properties, and interaction with the radiation field is poor, which is a major impediment in our interpretation of the observational evidence.

Our approach to these issues is by detailed multiwavelength studies of samples representing key elements in the above puzzle which will help us better understand the nature of the sources making up the CIB, as well as improving our understanding of galaxy formation and evolution.

The data we present here is now a large enough sample, including near-IR, far-IR, sub-mm and radio observations, to be able to tackle some of these issues. We do this through a combination of direct SED fitting, statistical analysis, consistency with other observations and comparison with model predictions, trying to use the minimum number of a priori assumptions. We have thus improved our knowledge of the nature of the sources in our sample, and through them the entire FIRBACK sample of which ours is representative.

Throughout we assume a flat Universe with  $H_0=75 \text{ km s}^{-1} \text{ Mpc}^{-1}$ ,  $\Omega_M=0.3$ , and  $\Omega_\Lambda=0.7$ .



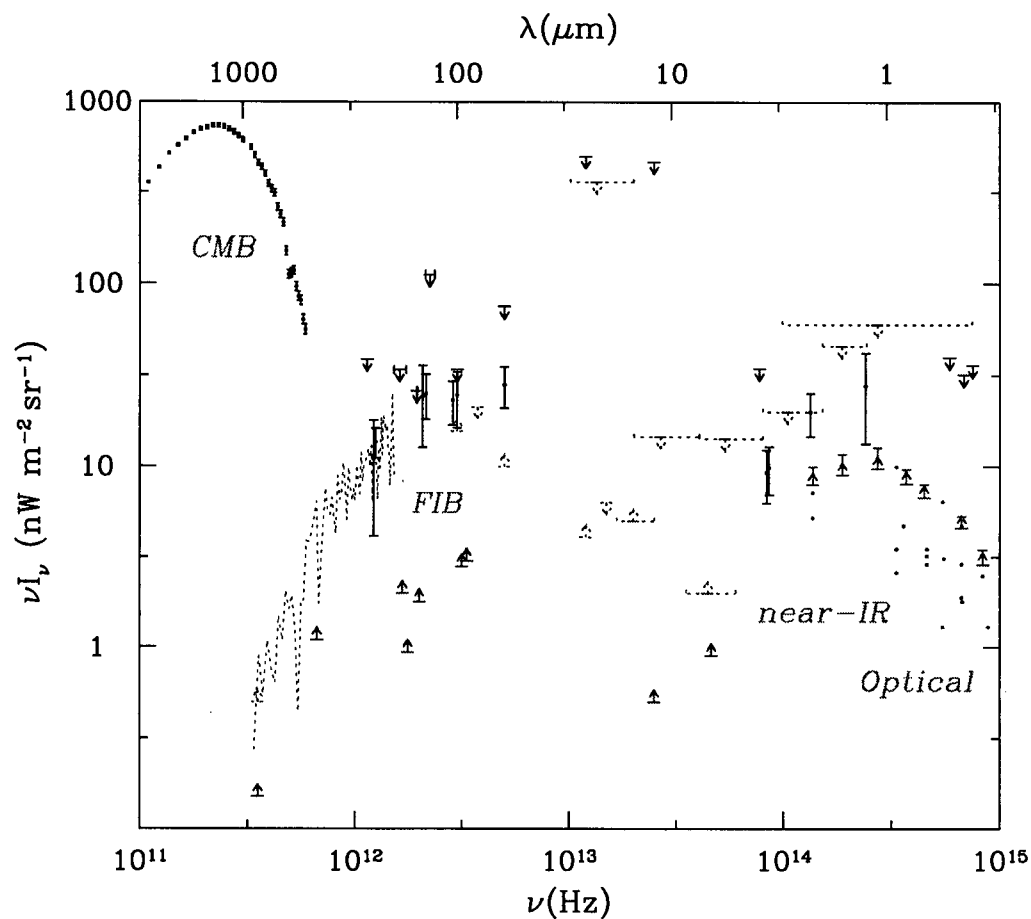


Figure 1.1: This figure [58] is a compilation showing the different extragalactic backgrounds including the CIB (called FIB here for Far-Infrared Background). Notice in particular that the power output in the far-IR spectral region is comparable to that in the optical region.

## 1.2 The Multiwavelength Approach

As stated in the previous section, we address the issues at hand via a multiwavelength study of our sample, which helps us infer information about the physical nature of the sources. Thus it is useful to review the sources of emission for each relevant part of the spectrum.

Near-IR: The near-IR emission is mostly direct starlight from an old quiescent stellar population. The  $K$ -band flux is about  $10\times$  less obscured by dust than the optical flux is. This makes it an almost independent (of the dust obscuration) gauge of the luminosity. However, in extreme conditions, such as exist in ULIGs, the extinction becomes substantial even in the near-IR and thus the stellar emission is attenuated by dust absorption resulting in power-law like spectra. This results in the  $K$  magnitude becoming more rapidly faint with increasing luminosity than can be accounted for by the distance dimming alone.

Far-IR: In our case this is  $170\mu\text{m}$  flux. It is due to thermal dust emission characterized by a grey-body spectrum – i.e. the Planck function multiplied by a dust emissivity term which is proportional to  $\nu^\beta$  in the optically thin limit:

$$S \propto B(\nu, T)\nu^\beta, \quad \text{where} \quad B(\nu, T) \propto \frac{\nu^3}{(e^{h\nu/kT} - 1)}. \quad (1.1)$$

In principle the ISM of a galaxy constitutes a spectrum of dust grain sizes with different emissivities and radiating at a range of temperatures, depending among other things on the metallicity, geometry, and radiation field of the galaxy. Exploring these in full is beyond the scope of this work, especially since it means dealing with a lot more free parameters than the available data can tackle. We will assume throughout a simple single dust component (ie. one  $\beta$ , one  $T_d$ ) which is not unreasonable if we restrict ourselves only to the  $\lambda \geq 170\mu\text{m}$  regime, which we address in a later chapter. The  $170\mu\text{m}$  data point is particularly important as it is near the peak of the CIB. It is also near enough to the peak of the dust emission for cold dust (larger grains)<sup>1</sup> that the ratio with  $850\mu\text{m}$  flux

---

<sup>1</sup>This can be argued simply by Wien's Law: a  $T \sim 30\text{K}$  source will peak at  $\lambda \sim 100\mu\text{m}$ , and a  $T \sim 15\text{K}$  source will peak at  $\lambda \sim 200\mu\text{m}$ .

has a non-trivial dependence on redshift – by  $z \sim 1$  there already is a significant change in slope (as the curvature near the peak of the SED begins to affect it). This allows us to fit the dust model with more precision than the sub-mm data alone would allow.

For higher luminosity sources, the dust emission is primarily the reprocessed UV-light of young, massive stars and thus is correlated with the SFR. For less active galaxies this may be more complicated due to the higher importance of the cirrus component, where the power originates in optically-bright older stars. Since, the estimated total luminosity of the IR/sub-mm spectrum is directly related to the dust mass (assuming the dust is optically thin), we can thus also estimate  $M_d$  (a lower limit in fact, since we use a single dust component).

Sub-mm: Apart from providing extra data points to fit the dust emission spectrum, the 850  $\mu\text{m}$  band is especially important in that it is almost redshift independent, due to the negative  $k$ -correction (discussed in more detail in a later chapter). It is thus primarily a luminosity measure rather than a distance measure. Since it is near the end of the thermal spectrum (the non-thermal spectrum begins to emerge roughly near rest-frame 1 mm), it is sensitive to the coldest dust component contributing to it. Using the sub-mm spectral slope in conjunction with the radio spectral index (see next) pin-points the location of the trough between the thermal and non-thermal parts of the SED, which can be used to estimate the redshift of the source (with some dust model dependence).

Radio: The radio flux is due to the well known synchrotron radiation caused by charged particles (electrons) gyrating about magnetic field lines. The emission is a power law of the form  $S \propto \nu^\alpha$ . The radio spectral index  $\alpha$  is related to the exponent of the energy distribution. The high energy electrons that generate this radiation could originate in AGN, but more commonly in supernovae which come from the death of the most massive stars. Thus the electron flux is also a gauge of the SFR. This is the physical reason behind the radio-IR(sub-mm) correlation since the power for both processes ultimately comes from the same massive stars whose lifetimes are short enough that the probe is almost instantaneous (at lower luminosities this would break down as explained above). At the highest luminosities, when it is almost certain that an AGN is present, it will contribute

power to both types of emission, thus the relation also approximately holds. We have insufficient information to explore variations in  $\alpha$  so we assume the canonical -0.75 [6].

# CHAPTER 2

## THE DATA

### 2.1 Sample

Targets were selected from the FIRBACK ( $> 3\sigma$ ) catalogue [21] in the ELAIS N1 field. Confusion remains a major issue with the ISO beam size, which is  $\sim 90''$ , and work is underway (by others) to address that. Our main selection criterion has been the availability of radio detections [15] inside the ISO beam. These are required for pointing since ISO's beam has roughly the area of the entire SCUBA array. Since the array is under-filled (in SCUBA photometry mode, see next section), targetting is very much less efficient if no better position is available than that determined by ISO. When we subtract from these sources radio-bright AGN, as well as sources with several radio detections per beam, we are left with 41 possible sources to draw from – we have followed up 30 (and additionally one N2 source) – listed in Table. 2.1. Notice that if only the  $> 4\sigma$  ( $=180$  mJy) catalogue is considered there are 24 sources with radio detections, of which we have followed up 21. Whereas with our 1999 observations we tried to bias our data toward higher detectability in the sub-mm [57], with the 2001 observations our philosophy was that since too little is known about these sources to be able to reliably select for sub-mm detectability, we would try to diversify our sample, and simply target FIRBACK sources with radio positions.

Fig. 2.1 shows the VLA coverage of the N1 field which is the primary source of radio fluxes for this field [15]. This incomplete coverage is the main reason for the lack of radio fluxes for a large fraction of the FIRBACK sources. Fig. 2.2 shows roughly the relative selection (based on a starburst galaxy template, see Chapter 4) in  $(L, z)$  space due to the  $170\ \mu\text{m}$  FIRBACK and the 21 cm VLA observations (assuming a detection limit of 0.15 mJy). The range plotted is meant to cover a range of galaxy properties. It is

estimated via two separate redshift estimators (discussed in detail in Chapter. 3). This plot makes it clear that the requirement that a radio position is available does not bias our sample additionally up to redshift  $z \sim 1$ , but is a possible factor for higher redshifts (depending on the specific galaxy properties).

Due to the broadness of selection criteria we believe our sample represents a fair cross-section of the FIRBACK population, rather than focusing on a specific sub-population. This can be seen in Fig. 2.3, where we compare the distribution of  $S_{170}/S_{1.4\text{GHz}}$  for all 41 possible sources with that of the 30 sources in our sample. We discuss the dotted line in later sections. The close agreement between the shape of the total distribution and that of our sample shows that even though this is a targetted follow-up and not a “blank-field” survey, trends for our sub-sample qualitatively correspond to those in the entire FIRBACK sample. This is reasonable, since apart from the brightest one or two sources, the 170  $\mu\text{m}$  fluxes (Table 3.1) span only a range of about a factor of 2.

Six of our sources have spectroscopic redshifts – N1-001 at  $z=0.03$ , N1-002 at  $z=0.07$  (Guilaine Lagache, private communication), N1-008 at  $z=0.26$  [50], N1-012 at  $z=0.02$  [60], N1-040 at  $z=0.45$ , and N1-064 at  $z=0.91$  [11].

## 2.2 The instrument

Currently the foremost sub-millimetre camera is the Sub-mm Common User Bolometer Array – SCUBA [36] on the James Clerk Maxwell Telescope (JCMT) located on Mauna Kea, Hawaii. At this altitude ( $\sim 4000\text{ m}$ ) the telescope is well above most of the water vapor (scale height  $\sim 2000\text{ m}$ ) which is the principal source of atmospheric opacity in the sub-mm. This leaves windows of transmission at certain wavelengths (see Fig. 2.4) making ground-based sub-mm astronomy possible. SCUBA consequently has filters designed for these windows at around 350  $\mu\text{m}$ , 450  $\mu\text{m}$ , 750  $\mu\text{m}$ , and 850  $\mu\text{m}$ . The instrument consists of a 37-bolometer long-wavelength (typically 850  $\mu\text{m}$ ) array, and 91-bolometer short-wavelength (typically 450  $\mu\text{m}$ ) array which operate simultaneously by means of a dichroic beam-splitter. The whole is cooled to 75 mK to maximize sensitivity (without

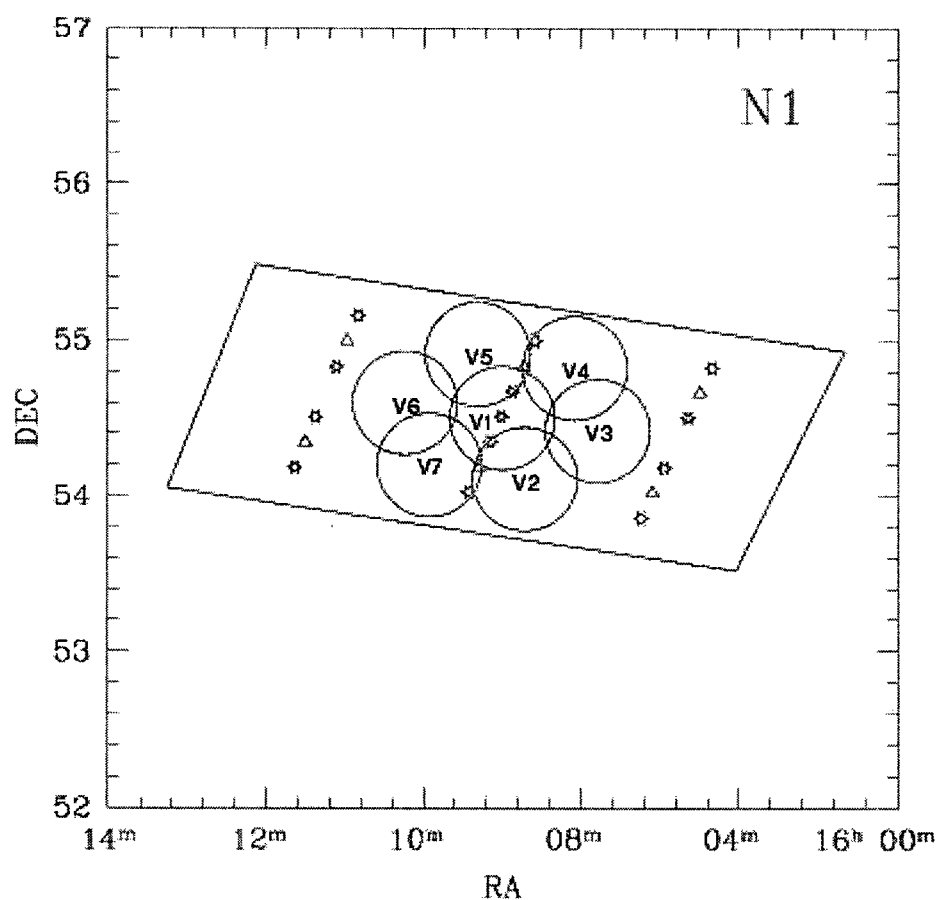


Figure 2.1: Shows the VLA coverage of the ELAIS-N1 field where our sample is located. Here the asterixes show the ISOPHOT pointings while the circles are  $\sim 30\%$  sensitivity of their centers for the VLA pointings (the absolute radio sensitivity varies from region to region)[15].

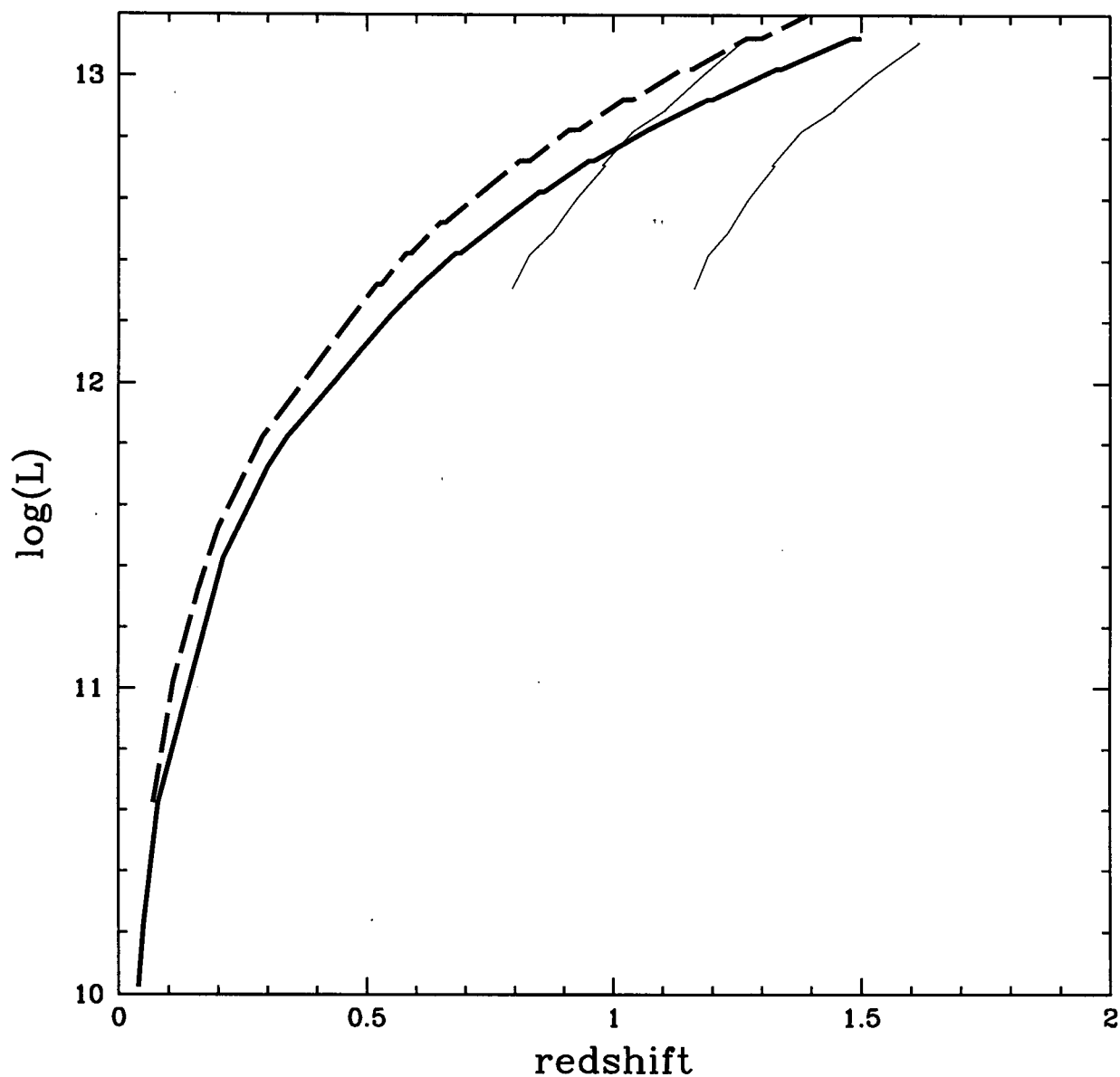


Figure 2.2: This roughly estimates the selection cut off of the FIRBACK survey in  $(L, z)$  space. The solid line is the  $3\sigma$  limit ( $=135$  mJy), the dashed line is the  $4\sigma$  limit ( $=180$  mJy). The thin lines roughly estimate the region of influence of the radio selection. See text for details.



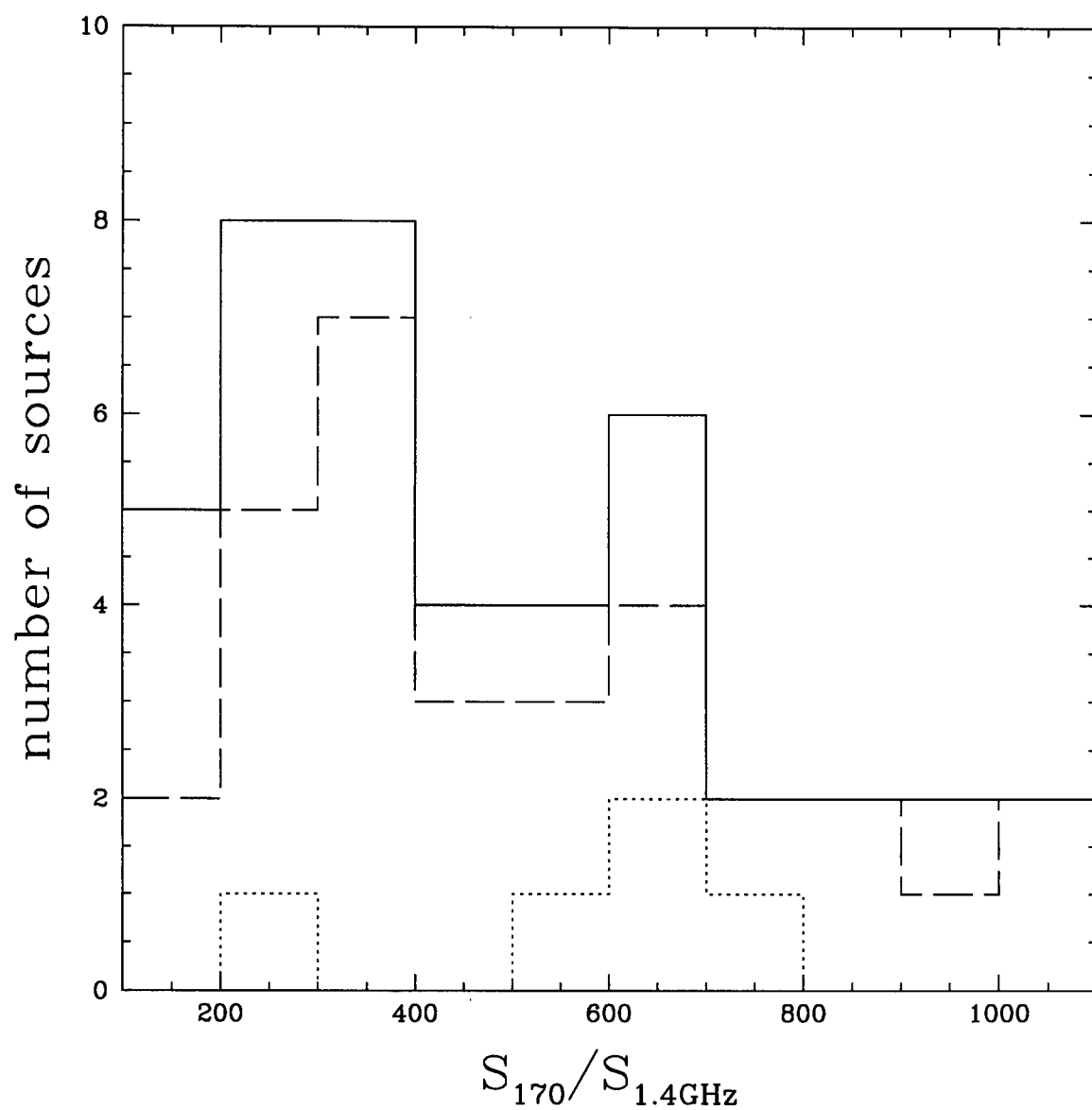


Figure 2.3: Distribution of the  $S_{170}/S_{1.4\text{GHz}}$  ratio. The solid histogram represents all the sources from the FIRBACK catalogue which have been observed in the radio. The dashed histogram is our sample. The dotted line shows our high- $z$  candidates (discussed in Chapter 3).

such cooling, thermal emission from the instrument itself would overwhelm the signal). The SCUBA long-wave beam FWHM is  $\sim 15''$  whereas the short-wave beam is  $\sim 8''$ .

Most of the sky signal is a "DC" offset, due primarily to sky emission, which is orders of magnitude larger than the astronomic signal. It is removed by chopping with the secondary mirror at a frequency of 7.8 Hz. In addition, nodding is performed every 10–20 s to take out more slowly varying sky gradients, and a huge telescope emission signal. This involves starting from the ON position (usually central bolometer on the source), placing the source onto the OFF position, and then reversing to the other side so that the final sequence is ON-OFF-OFF-ON. Each nod pair is combined by subtracting the signals at the two positions [25] giving a triple-beam  $(-0.5, +1.0, -0.5)$  pattern on the sky. Since this nodding is rather slow, the process still leaves us with a small, but non-zero mean in the non-source bolometers, as well as with some left over correlated sky noise. Thus further sky removal is necessary, which is done at the data reduction stage (see section 2.4 and Appendix A).

## 2.3 SCUBA sub-mm observations

The observations presented here were taken with SCUBA in March 1999 and in March and May 2001. In order to avoid biasing our data, we attempted to observe each source until a predetermined rms ( $\sim 1.5$  mJy) was reached, irrespective of whether the source appeared to be a possible detection or not. The March 2001 data were taken in exceptional grade 1 weather ( $\tau_{225} \sim 0.04^1$ , and as low as 0.02), whereas the 1999 data were taken in a merely 'good' weather ( $\tau_{225} \sim 0.07$  or better). The May 2001 data were taken in worse conditions of  $\tau_{225} > 0.1$ . Throughout we used the 2-bolometer chopping mode. This involves chopping in array coordinates in order to always align one negative beam exactly with a specific off-centre bolometer. Thus the negative beams can be folded in,

---

<sup>1</sup>The value of  $\tau_{225}$  (at 225 GHz=1.3 mm) is taken every 10 min at the Caltech Submillimetre Observatory (CSO), and thus has become a standard weather monitor. It is strongly correlated with  $\tau$  at 850  $\mu$ m and 450  $\mu$ m (see next section).

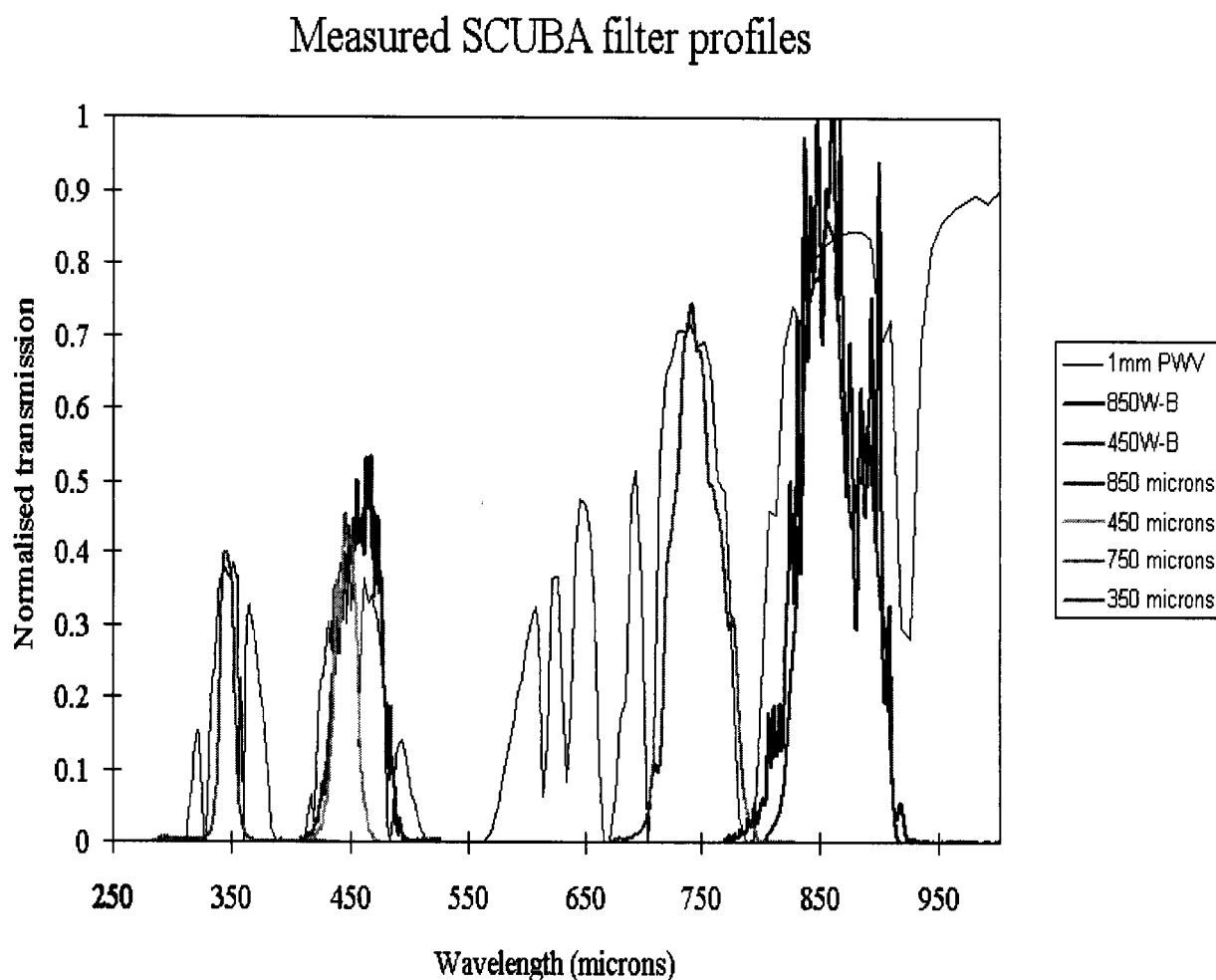


Figure 2.4: This shows the performance of the new SCUBA wide-band filters measured in the winter of 2000 compared to the old filters. Notice in particular the dramatic improvement in the 450  $\mu\text{m}$  filter (30-40% depending on the weather). The black curve is the atmospheric transmission on Mauna Kea (1mm PWV=precipitative water vapour). This figure was taken from the JCMT website. The filters were measured by D.Naylor and W.Holland.

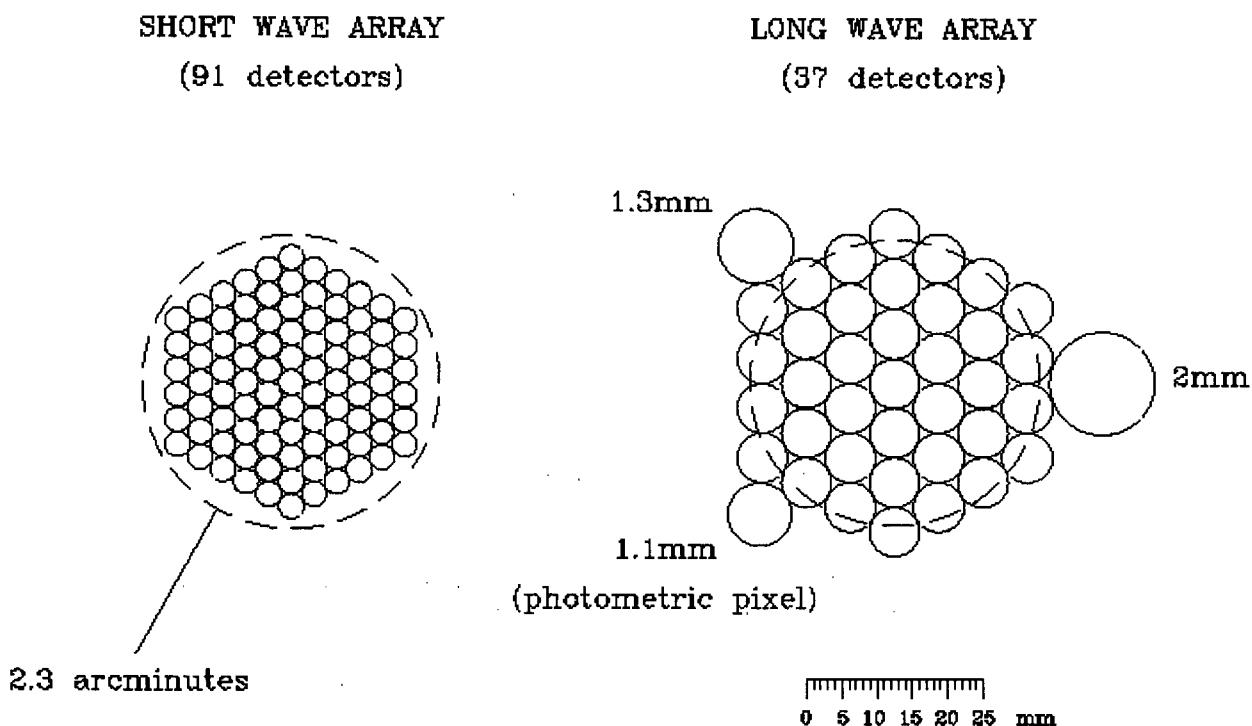


Figure 2.5: The SCUBA arrays (courtesy of the JCMT website ). Here shown is both the physical scale of the arrays ( $\sim 25$  mm) as well as the field of view ( $\sim 2.3$  arcmin). Note that the closely packed arrays shown here are misleading – the arrays are in fact highly undersampled. Using the basic jiggle mode of observing requires 64-point jiggles to create a fully sampled map in both bands (the spacing between 2 jiggle points is roughly  $2''$ ). The photometry mode, that we use, involves a 9-point jiggle pattern with spacings of  $1''$ . This is much more efficient at quickly reaching the desired SNR in a given bolometer, but the other bolometers produce a very undersampled map.

improving the rms by a factor of  $\sqrt{2/3}$  (see Appendix A). Unfortunately, for our 2001 run, software problems with the new telescope control system resulted in SCUBA not chopping onto another bolometer, making the negative beam unrecoverable. Thus the 2001 data presented here are from the central bolometer only, whereas the 1999 data have the negative beams folded in with the central signal. This is balanced by the exceptional weather conditions during observing. As a result, the 2001 data (March) have slightly higher rms at  $850\ \mu\text{m}$ , but considerably better rms at  $450\ \mu\text{m}$  (due to better weather and the new wide-band filter).

The data were taken in photometry mode which involves integrating in a 9-point jiggle pattern (taking  $\sim 18\text{ s}$  per integration) which is the most efficient way to reach the desired rms in a given bolometer, but leaves us with an undersampled map (see Fig. 2.5). However the other bolometers are still valuable for subtracting the residual sky emission. Nightly calibration observations were carried out on Mars, Uranus, CRL618, and CRL2688 (the last two are among the standard calibrator sources for SCUBA), typically at the beginning and end of the night (Table 2.2). Pointing checks were done between each change in source (or roughly every  $(200 \times 18\text{ s}) = 1\text{ hour}$ ). The drift was never greater than a few arcseconds, and usually was on the order of  $2''$ .

## 2.4 SCUBA data reduction

The data were reduced using the SCUBA User Reduction Facility – SURF package [42] for the preliminary stages of the reduction (up to the extinction correction), and custom written software for all subsequent stages. This allows us better control over and understanding of the process, as well as making it computationally more efficient.

The extinction correction was performed using skydip observations<sup>2</sup> whenever available,

---

<sup>2</sup>For 1999 data, the default temperatures (used by the SKYDIP routine in deriving  $\tau$ ) were incorrect (the problem was discovered October, 1999). This is particularly severe for  $450\ \mu\text{m}$  data. This is an additional reason requiring some re-reduction of that data.

and with a derived optical depth from the  $\tau_{\text{CSO}} - \tau_{\text{SCUBA}}$  relations otherwise<sup>3</sup>:

$$\tau_{850} = 4.02(\tau_{\text{CSO}} - 0.001) \quad \text{and} \quad \tau_{450} = 26.2(\tau_{\text{CSO}} - 0.014). \quad (2.1)$$

Our data (Fig. 2.6) seem to suggest that the standard relations given above should not be used in the grade 1 ( $\tau_{225} < 0.05$ ) regime. Thus we prefer to use the SKYDIP derived opacities for the observations taken in that regime whenever possible. Notice also that in poor weather (high  $\tau$ ) the scatter is considerable. The  $450 \mu\text{m}$  data in particular are not reliable, as was already shown by L. Dunne [25]. We reproduce her figure below as it is illustrative for our purposes. Also Archibald et al. [1] find that  $\tau_{450}$  in grade 4 weather tends to be higher than predicted, which our data support (although not strongly due to small numbers).

Thus for most of our March 2001 data where the scatter is small in both bands, the error introduced at this stage is negligible compared to the noise (see next Chapter). For the weather conditions of most of 1999, March 19 and May 14, 2001, the error in the  $450 \mu\text{m}$  fluxes is  $\sim 5 - 10\%$  (read off figure). For the rest of May, 2001, the  $450 \mu\text{m}$  error is  $\sim 25 - 100\%$  so derived fluxes should be viewed with greater suspicion (affected are N1-016, N1-039, and N1-041).

When calibrating SCUBA data, it is typical to use standard gains – i.e. flux conversion factors between Volts and Janskys. It is clear that using individual calibration observations is not ideal as various factors (such as pointing errors, extended source emission, intrinsic source variability) can introduce significant scatter. However it is also clear that using the same gains for data taken in different instrument and/or atmospheric conditions may also be inaccurate. The gains were derived using the JCMT FLUXES program (standard error  $\sim 5\%$ ) to obtain the flux of a planet, in Jy, for the time of observation (for non-planetary calibrator fluxes we use the JCMT standard calibrators page), and taking its ratio to the signal in Volts. The standard gains for the post-upgrade 2001 data are  $197 \pm 13 \text{ Jy/V}$  at  $850 \mu\text{m}$  and  $384 \pm 82 \text{ Jy/V}$  at  $450 \mu\text{m}$  (from the JCMT website), with

---

<sup>3</sup>For the 1999 (taken with the pre-upgrade narrow-band filters) the relations are:  $\tau_{850} = 3.99(\tau_{\text{CSO}} - 0.004)$  and  $\tau_{450} = 23.5(\tau_{\text{CSO}} - 0.012)$

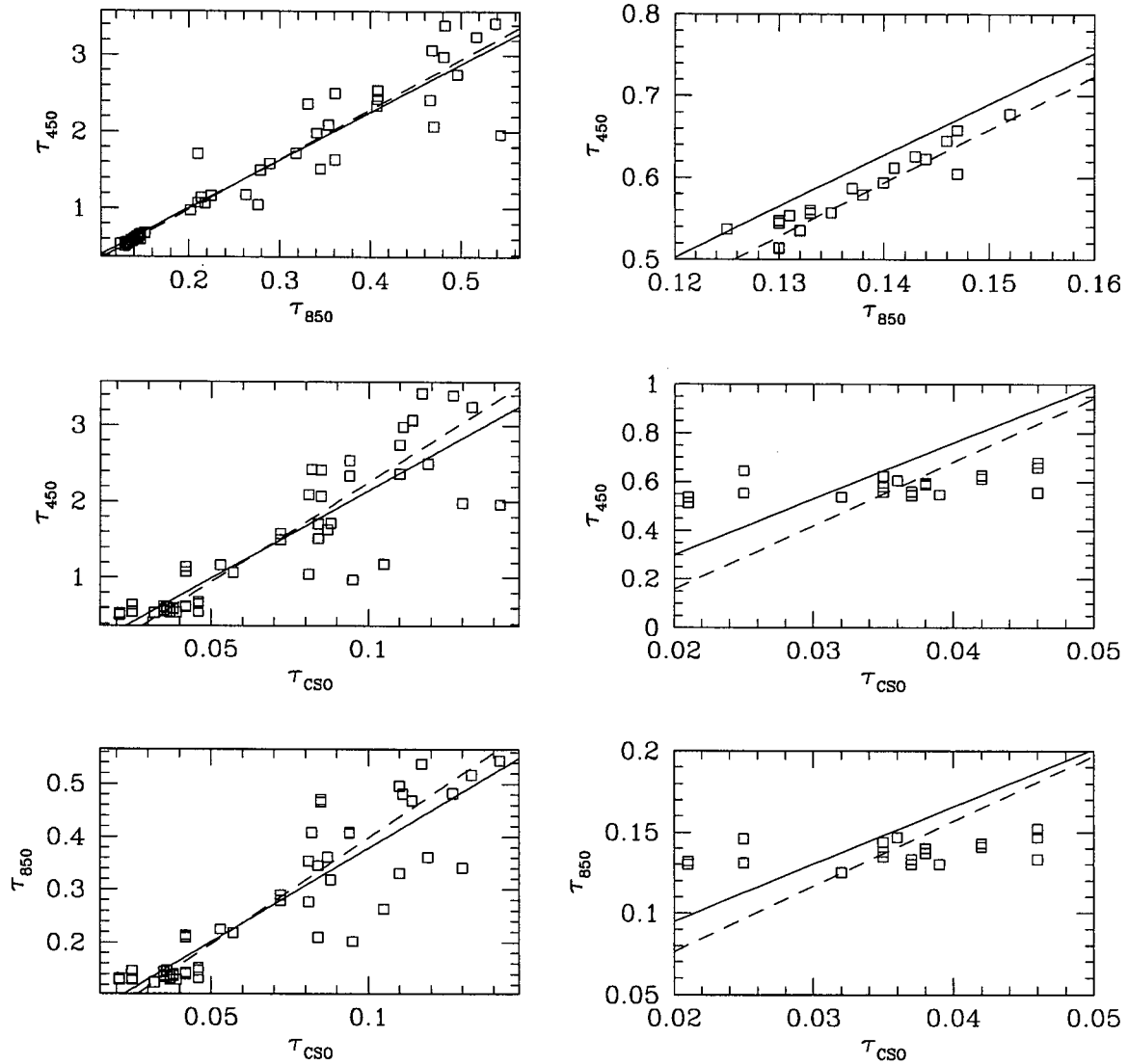


Figure 2.6: Relations between optical depths derived from 26 skydip observations in 2001 (note the weighting towards grade 1 weather). The left hand panels show the entire range, while the right hand panels zoom to the grade 1 data ( $\tau_{CSO} < 0.05$ ) only. Here the dashed lines are the standard relations [1], while the solid lines are simple linear fits to our data (the same fit is shown in both columns). The two are sufficiently similar overall, considering the uneven weighting, and the inclusion of outliers. However, the relations with the CSO  $\tau$  seem to be shallower for the grade 1 data than the single slope relation, which may be due to the uncertainty in  $\tau_{CSO}$ .

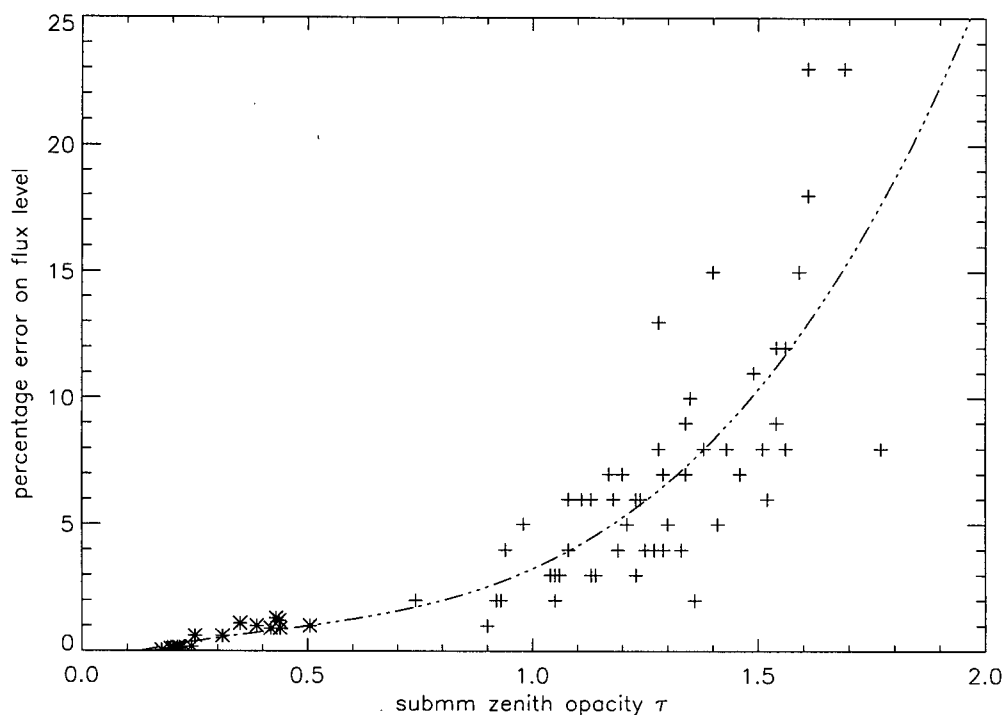


Figure 2.7: This shows the percentage error in the flux estimate as a function of optical depth  $\tau$ . Here crosses are 450  $\mu\text{m}$  and stars are 850  $\mu\text{m}$  data. The airmass is 1.3 (i.e.  $y$ -axis scales as  $\sim A/1.3$ ). The fit is  $y = -0.58 + 5.24\tau - 6.97\tau^2 + 5.56\tau^3$ . Notice that our May 2001 data is off the scale here in 450  $\mu\text{m}$ , and that with the above relation a  $\tau \sim 3$  gives roughly 100% error. This figure is reproduced from [25].



roughly 250 Jy/V and 800 Jy/V for the pre-upgrade 1999 observations (the difference is mostly due to the new wide-band filters – see previous section).

The gains we derive are presented in Table 2.3. We estimate the calibration uncertainties as the standard deviation from the run mean using all calibration observations in a given month. For March 2001 we obtain average gains of  $G_{450}=371\pm118$  Jy/V and  $G_{850}=210\pm18$  Jy/V. For May 2001  $G_{850}=237\pm15$  Jy/V ( $G_{450}$  is poorly constrained as described above). For 1999  $G_{450}=748\pm142$  Jy/V and  $G_{850}=237\pm15$  Jy/V. These last include all observations; however, we find that Mars calibration observations (total 2) give gains that are far lower:  $\sim 220$ -230 Jy/V in 850  $\mu$ m and  $\sim 400$ -600 Jy/V at 450  $\mu$ m, while Uranus-derived gains are more consistent with the standards. We are unsure of the cause of this discrepancy, however note that Mars was fairly extended at the time (diameter  $\sim 12''$ ) which makes modelling the flux/beam from it less certain. If we discard these, we are left for the entire run (6 days) with only 2 Uranus calibration observations that are more trustworthy (one IRC\_10216 observation is also dubious as the source is quite extended and variable). The calibration observations do not agree internally, and are too few to feel secure about the uncertainties arising from systematic effects (see above). We therefore, conservatively, decide to use the standard gains for our 1999 run which moreover are consistent with the averages within their uncertainties. Our lesson here is that if calibration is important (as in this study) a sufficient number of calibration observations must be performed and the calibrators must be well matched to the observing mode: for photometry they need to be stable and pointlike for SCUBA's beams.

Notice that the values for May 2001 also differ from the standard. This is most likely due to observing being done in grade 3 weather with consequent large uncertainties both in sky opacities (which is the most likely culprit here) and gains. Only three sources (see above) were partially observed at that time, and none are individually detected ( $\ll 2\sigma$  signals in both bands). At this stage we have not worried about these apparently excessive gains as their impact on our results is negligible.

Systematic uncertainties in the opacity and calibration estimates are hard to quantify, but it should be noted in later sections that we will be quoting statistical errors only.

The next step is sky-subtraction, or removal of the average level at each time step, which is well known to be a crucial step in reducing SCUBA data (see previous section). The sky was subtracted as a mean level for the entire array excluding the signal bolometers as well as any bad bolometers, as revealed by excessive noise levels. Appendix A gives some more detail on the process of reducing SCUBA photometry data (specifically as performed by our code).

## 2.5 UKIRT near-IR observations

Most of our SCUBA detected FIRBACK sources could not be identified in DPOSS images. As the sources are expected to be extinguished by dust and therefore have red spectra, we obtained deep observations in the  $K$ -band at UKIRT using the Fast Track Imager (UFTI) for maximum sensitivity to obscured components. The small UFTI field ( $50'' \times 50''$ ) was centered on the source positions taken from the radio/SCUBA identifications. Each source was imaged for a total of 1800 s, with individual exposures of 60 s each, reaching a limiting magnitude in a  $2''$  diameter aperture of  $K = 20.4(5\sigma)$ . The fast tip/tilt, adaptively corrected imaging resulted in seeing better than median conditions at  $0.4''$  FWHM. Data were reduced using the Starlink, UKIRT/UFTI image processing tools under the ORACDR environment [7]. We wrote custom ORACDR scripts to optimize point source sensitivity in our essentially blank field observations, creating flat fields from each 9-point dither, and high signal-to-noise thermal background images from 60 minutes of data centered around the observing period of the given FIRBACK source.

The  $K$ -band images for the 12 sources observed in this way are presented in Fig. 3.1.

Table 2.1: Source coordinates

Source	RA [hh:mm:ss]	DEC [dd:mm:ss]
N1-001	16:07:36.37	53:57:32.72
N1-002 <sup>†</sup>	16:10:05.83	54:10:29.81
N1-004	16:11:09.38	53:58:07.54
N1-007	16:13:31.25	54:16:28.50
N1-008 <sup>†</sup>	16:08:57.98	54:18:16.83
N1-009	16:08:03.89	54:53:02.39
N1-010	16:09:34.91	53:52:23.61
N1-012	16:12:14.35	54:08:32.78
N1-013 <sup>†</sup>	16:07:41.15	55:01:53.87
N1-015	16:07:24.44	54:12:08.53
N1-016	16:07:38.12	54:46:03.08
N1-024	16:09:37.44	54:12:59.69
N1-029	16:11:17.43	54:16:28.27
N1-031 <sup>†</sup>	16:11:03.74	54:43:19.79
N1-032	16:12:42.34	54:37:38.37
N1-034 <sup>†</sup>	16:07:19.34	54:43:06.99
N1-039	16:08:48.78	54:51:52.54
N1-040 <sup>†</sup>	16:09:28.01	54:28:32.56
N1-041	16:08:14.00	54:28:35.92
N1-045	16:08:53.76	54:47:34.71
N1-048 <sup>†</sup>	16:11:02.53	54:23:28.81
N1-056	16:11:43.46	54:16:24.05

Table 2.1: *continued ...*

Source	RA [hh:mm:ss]	DEC [dd:mm:ss]
N1-059	16:07:58.05	54:23:52.98
N1-064 <sup>†</sup>	16:08:25.33	54:38:09.52
N1-068	16:10:41.36	54:10:29.37
N1-077	16:07:09.46	54:49:24.09
N1-078	16:12:34.96	54:29:17.63
N1-083 <sup>†</sup>	16:10:19.24	54:21:53.73
N1-101	16:09:45.95	54:21:23.77
N1-153 <sup>†</sup>	16:09:59.67	54:36:44.83
N2-013	16:34:05.78	40:51:09.80

<sup>†</sup> These sources form the 1999 sample.

Table 2.2: Calibration values

Date	850 $\mu\text{m}$ gain [Jy/V]	450 $\mu\text{m}$ gain [Jy/V]	Calibrator
<b>1999</b>			
March 18	225(250) <sup>a</sup>	406(800)	Mars
March 19	240(250)	670(800)	Mars+Uranus
March 20	227(250)	608(800)	irc_10216
March 21	257(250)	1338(800)	Uranus
March 22	(250)	(800)	none
March 23	(250)	(800)	none
<b>2001</b>			
March 13	206	343	crl618
March 15	225	374	Mars+crl2688
March 17	198	327	Mars+Uranus
March 18	198	340	Mars+Uranus
March 19	212	328	Mars+Uranus
May 14	(250)	(390)	none
May 22	(250)	(390)	none
May 25	252	361	crl2688
May 26	256	406	Uranus+crl2688
May 28	241	404	Mars+Uranus

<sup>a</sup> The values in brackets are for days with no calibration observations, or the data quality was too poor. When both are given, the value in brackets is used. When more than one calibrator is given, the gain quoted is the average. See text for details, especially on 1999 calibration.

# CHAPTER 3

## RESULTS & ANALYSIS

### 3.1 Assembling the multiwavelength data

The 1999 data presented here were previously discussed in Scott et al. (2000)<sup>1</sup>. However we re-reduced the data again concurrently with the 2001 data in order to ensure uniformity (especially as an upgraded version of SURF and a custom-written code was used). We confirm all previously reported detections. The 2001 data have three unambiguous detections at  $450\ \mu\text{m}$  (N1-004, N1-024, N1-078). This high detection rate at a difficult band is due to the exceptional atmospheric conditions during our observing run as well as the far superior performance of the new wide-band filter (see Fig. 2.2). In addition there are three new detections at  $850\ \mu\text{m}$  (N1-001, N1-059, N-078). Note that the few arcsecond pointing uncertainty (see previous) has only a small effect on the long wavelength data, but may be a significant reason for the apparently missing  $450\ \mu\text{m}$  flux (where the beam FWHM is only  $\sim 7''$ ) in sources where one would expect to find some (e.g. N1-059).

The sample as a whole is detected at the  $10.6\sigma$  level at  $850\ \mu\text{m}$ , and at the  $9.0\sigma$  level at  $450\ \mu\text{m}$  ( $\langle S_{850} \rangle = 2.5 \pm 0.2\ \text{mJy}$  and  $\langle S_{450} \rangle = 16.7 \pm 1.9\ \text{mJy}$ ).

Our results for the entire sample are presented in Table 3.1, which, in addition to the sub-mm data, includes the near-IR, far-IR, and radio (discussed below).

The near-IR data are from the UKIRT observations where available, and from the 2MASS catalogue elsewhere (sources with  $K \sim 14-15$  were not in the 2MASS catalogue, but we estimated their magnitudes directly from the calibrated catalogue images via aperture photometry in GAIA), except for N2-013 since the N2 field was not observed.

---

<sup>1</sup>Note that we use the naming scheme of Dole et al. (2001), which differs from the earlier convention used. In particular N1-038, N1-061, N1-063 from Scott et al. (2000) correspond to the new N1-040, N1-048, N1-064.

Table 3.1: Multiwavelength data for our sample<sup>a</sup>

Source	$K$	$S_{100}$	$S_{170}$	$S_{450}$	$S_{850}$	$S_{1.4\text{GHz}}$
N1-001	12.4±0.1	430±87	597±72	-3.0±14.0	6.1±1.6	0.74±0.23
N1-002	12.7±0.1	340±121	544±69	14.4±12.4	4.4±1.1	0.64±0.04
N1-004	12.4±0.0	300±73	391±58	32.5±7.2	3.6±1.4	0.88±0.13
N1-007	13.2±0.1	480±73	338±54	23.4±8.1	4.4±1.6	1.04±0.12
N1-008	14.2±0.1	160±73	335±54	25.9±14.0	1.9±1.1	2.98±0.04
N1-009	12.0±0.0	310±58	313±52	10.6±7.6	3.5±1.5	1.15±0.11
N1-010	13.0±0.0	360±99	309±52	15.2±10.8	1.8±1.4	1.05±0.20
N1-012	13.9±0.2	320±122	302±51	9.2±10.0	1.5±1.6	0.31±0.07
N1-013	16.8±0.1	350±75	294±51	18.8±9.9	0.0±1.5	0.52±0.15
N1-015	14.8±0.1	230±41	294±51	-3.4±7.7	1.4±1.6	0.52±0.07
N1-016	13.2±0.1	470±20	289±50	34.8±16.7	1.5±1.2	1.55±0.13
N1-024	14.2±0.0	220±69	266±49	32.3±7.5	2.9±1.3	0.75±0.02
N1-029	14.3±0.1	340±83	229±46	20.0±14.2	0.5±1.7	0.69±0.05
N1-031	13.5±0.1	110±78	225±46	9.2±13.2	1.9±1.1	0.43±0.06
N1-032	18.5-19.5	220±53	224±46	14.9±7.7	1.3±1.4	0.21±0.05
N1-034	19.3±0.8	270±71	221±46	95.1±27.5	1.3±1.3	0.33±0.07
N1-039	15.8±0.2	230±0	205±44	10.9±86.8	-0.1±2.3	0.58±0.07
N1-040	19.4±0.6	0±0	205±44	29.2±20.5	5.4±1.1	0.33±0.03
N1-041	14.7±0.1	150±55	204±44	20.4±156.7	-0.1±2.5	0.76±0.06
N1-045	14.4±0.0	280±46	198±44	15.3±8.3	3.0±1.4	0.43±0.06
N1-048	19.3±0.9	250±51	192±44	15.5±11.6	4.2±1.1	0.37±0.05
N1-056	15.9±0.2	160±71	179±43	-8.6±8.4	0.0±1.6	0.24±0.02

Table 3.1: *continued...*

Source	$K$	$S_{100}$	$S_{170}$	$S_{450}$	$S_{850}$	$S_{1.4\text{GHz}}$
N1-059	$20.4 \pm 0.9$	$230 \pm 66$	$175 \pm 42$	$6.9 \pm 34.5$	$6.4 \pm 1.9$	$0.60 \pm 0.06$
N1-064	$18.2 \pm 0.3$	$260 \pm 79$	$166 \pm 42$	$35.2 \pm 13.9$	$5.1 \pm 1.2$	$0.23 \pm 0.04$
N1-068	$15.3 \pm 0.1$	$320 \pm 95$	$165 \pm 42$	$15.1 \pm 7.6$	$2.2 \pm 1.4$	$0.44 \pm 0.05$
N1-077	$15.5 \pm 0.2$	$200 \pm 89$	$159 \pm 41$	$5.9 \pm 7.3$	$1.1 \pm 1.3$	$0.40 \pm 0.10$
N1-078	$18.0 \pm 0.4$	$240 \pm 63$	$158 \pm 41$	$35.2 \pm 8.7$	$5.7 \pm 1.3$	$0.24 \pm 0.04$
N1-083	$15.4 \pm 0.2$	$300 \pm 73$	$150 \pm 41$	$16.2 \pm 16.0$	$0.7 \pm 1.2$	$0.55 \pm 0.03$
N1-101	$15.2 \pm 0.2$	$210 \pm 73$	$136 \pm 40$	$19.8 \pm 7.5$	$0.9 \pm 1.5$	$0.39 \pm 0.05$
N1-153	$15.5 \pm 0.2$	$140 \pm 58$	$103 \pm 37$	$9.6 \pm 15.3$	$-0.2 \pm 1.0$	$0.24 \pm 0.03$
N2-013	$0.0 \pm 0.0$	$310 \pm 75$	$244 \pm 53$	$23.5 \pm 15.9$	$3.5 \pm 1.4$	$0.30 \pm 0.07$

<sup>a</sup> The  $K$  band values are in magnitudes, the other values are in mJy. The errors are  $1\sigma$ .

The IRAS fluxes (100  $\mu\text{m}$  here only) were obtained using the XSCANPI facility. We quote them here for the sake of completeness as well as to help in comparison with IRAS galaxies where the typically quoted detection limit is  $\sim 1$  Jy. The errors quoted are purely statistical; however, at this faint level systematic errors (including, among other things IR cirrus and mapping artefacts) in estimating the flux dominate to the point of making such estimates of little statistical use.

The radio fluxes are from a VLA survey of the field [15] (see Fig. 2.2), as well as from FIRST observations in this region (see [50]) (which also give a highly inhomogeneous/incomplete coverage).

Two possible sources of systematic uncertainty in comparing the far-IR and SCUBA fluxes are: 1) the different sizes of the ISO (about  $90''$ ) and SCUBA (about  $14''$ ) beams, and thus the possibility of multiple sources within the beam – this is also complicated by the issue of clustering, and possibly lensing; and 2) the relative proximity of the bulk of our sources and thus the possibility of at least a few being extended beyond the SCUBA beam. This is especially severe for the  $450 \mu\text{m} \sim 8''$  beam – e.g. N1-001 can be viewed



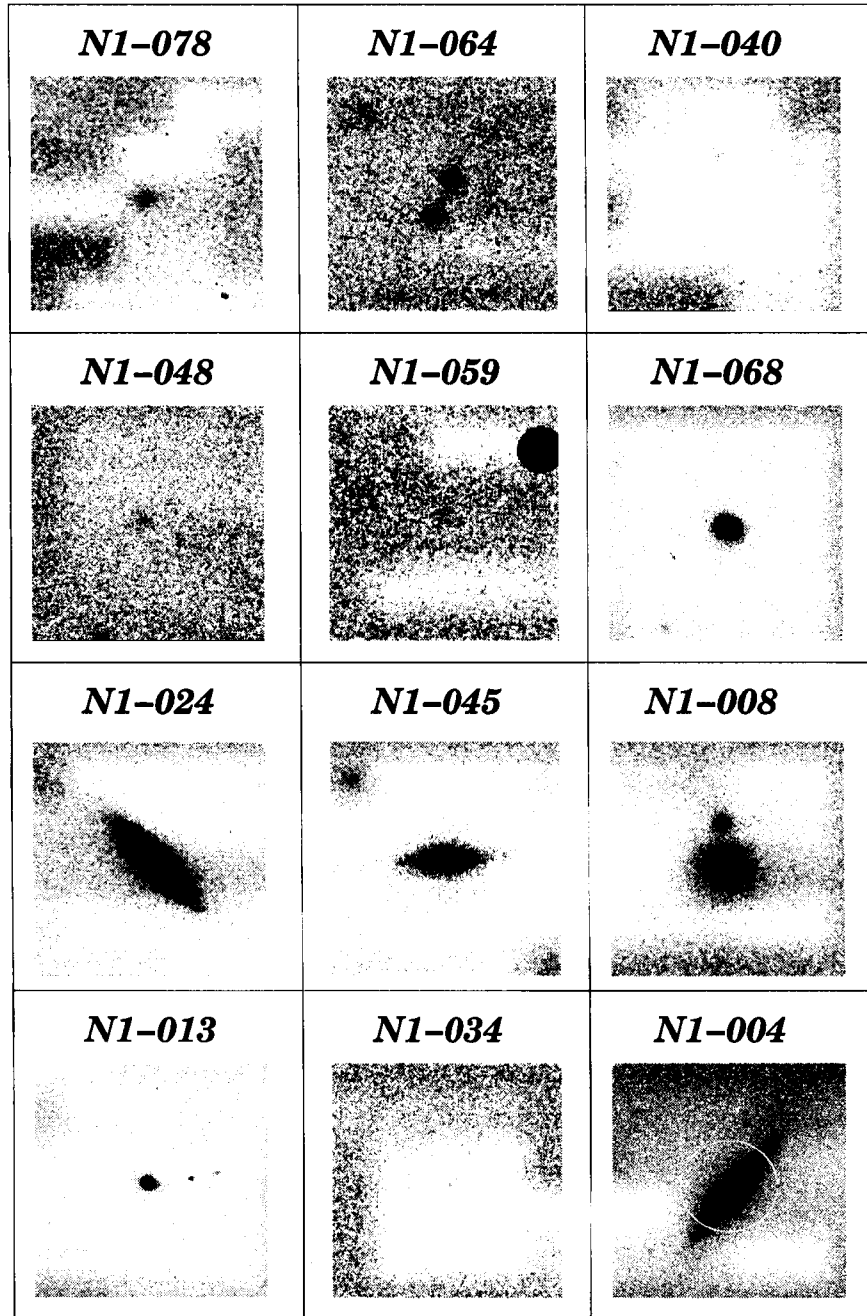


Figure 3.1: The available UKIRT *K*-band images – centered on the radio positions. These images are about  $15'' \times 15''$ , or roughly one SCUBA FWHM  $850 \mu\text{m}$  beam size. The exception is N1-004 where the SCUBA beam is the white circle, as the galaxy itself is larger than this.

as an ellipse in its 2MASS image with major and minor axes of about  $20''$  and  $7''$ , respectively. In general, however, other wavelengths images, are insufficient to determine precisely how much flux is being lost in this way, as it is not clear how concentrated the sub-mm emission would be – how it is distributed in comparison with other wavebands. The flux estimate itself is likely to be less accurate in photometry mode if the source size is on the order the beam size. These effects, of course, become more important with increasing  $S_{170}$ . Fig. 3.2 shows these effects in some more pronounced cases.

## 3.2 Linear Correlations

Looking at the black-body function (eq-n 3.1), we see that when observing a redshifted source the term  $hc/\lambda kT$  becomes  $hc(1+z)/\lambda_{\text{obs}}T$ . So it is immediately apparent that interpretations of the far-IR/sub-mm data will be degenerate in the dust model and redshift (mainly the  $(1+z)/T_d$  parameter, with some  $\beta$ -dependence as well). Essentially cold, nearby sources look similar to warm, far away ones. To a large degree this degeneracy holds for the near-IR, and radio data as well. However, we can still succeed in differentiating somewhat among these parameters due to the large size and spectral coverage of our sample. This allows us to look at a variety of projections, allowing some breaking of the degeneracy. Since a fifth of our sample has available spectroscopic redshifts (4 local, and 2 higher  $z$ ), we can use those as a test for the validity of any conclusions we make. Fig. 3.3 shows a variety of projections for our data from far-IR to radio, where each plot has been treated through the same analysis: a fit is made to all points using a straight line passing through the origin, i.e.  $y = mx$  (except when ratios are fitted, when the zero intercept requirement is lifted), excluding the  $> 2\sigma$  outliers, then a new fit is made and is plotted along with the  $1\sigma$  scatter. Table 3.2 shows the results. Notice that for the colour-colour plot we followed a different recipe. There we excluded the outliers (six sources are far outside the boundaries of the plot) by hand, and fit the rest with a standard  $\chi^2$  without forcing a zero intercept. Since in most cases, the errors in the two directions are of comparable size, rather than use the conventional 1-D  $\chi^2$ , we minimize



Figure 3.2: This figure is meant to illustrate, in their most obvious cases, the systematic effects that must be kept in mind when trying to interpret the data at hand. Both images are roughly the size of ISO's beam. On the left is N1-004 with the SCUBA  $850\,\mu\text{m}$  beam shown to the side (the  $450\,\mu\text{m}$  one is about half of that). On the right is N1-008 with the positions of the two radio detections indicated. Our observation is for the stronger of the two – a  $3.0\,\text{mJy}$  radio source. Notice that the other radio detection ( $0.3\,\text{mJy}$ ) has a fainter near-IR counterpart which potentially could be a higher- $z$  source. We will explore this further with upcoming observations.

Table 3.2: Results for the linear fits to the data

Relation	slope	$y$ -intercept <sup>a</sup>	rms	$\chi^2$
850 $\mu\text{m}$ vs. 170 $\mu\text{m}$	0.01	0.00	1.23	18.07
450 $\mu\text{m}$ vs. 850 $\mu\text{m}$	7.05	0.00	11.74	13.95
850 $\mu\text{m}$ vs. 1.4 GHz	3.66	0.00	2.18	70.76
850 $\mu\text{m}$ vs. 850 $\mu\text{m}/450 \mu\text{m}$	20.00	0.00	1.36	7.04
850 $\mu\text{m}/1.4 \text{ GHz}$ vs. 850 $\mu\text{m}$	1.82	0.00	2.46	12.19

<sup>a</sup> Notice that for all flux-flux fits a  $y$ -intercept of zero has been forced.

the following:

$$\chi_{2D}^2 = \sum_{i=1}^N \frac{(y_i - mx_i)^2}{(\sigma_{yi}^2 + m^2 \sigma_{xi}^2)} \quad (3.1)$$

and show the results in Table 3.2.

In general, it appears that the typical uncertainties of our sub-mm data points are larger than the  $1\sigma$  scatter of the fits. This implies that our errors are overestimated. We test this explicitly for the  $S_{450}$  vs.  $S_{850}$  plot by estimating the probability of a given  $\chi_{2D}^2$  via Monte Carlo simulations of the data. The procedure followed was to generate random 850  $\mu\text{m}$  fluxes within the range of our data, and find their 450  $\mu\text{m}$  analogues using the best-fit slope of the data (the  $y$ -intercept was set to zero). We smear both directions with gaussian errors which we read off the true data in order to make the simulated distributions as close to the true one as possible. We obtain a  $\chi^2$  of 30 when fitting all our data using the above. However if we exclude the clear outliers (N1-001, N1-034, and N1-059 which have highly discrepant colours as we show later) from the analysis we obtain a  $\chi^2$  of 14, whose probability is  $\sim 2\%$ . This is shown in Fig. 3.4. At present we do not have an explanation for this. The procedure followed in deriving the fluxes and errors from our code is described in Appendix A; however, note that the same inconsistency is observed when using SURF derived values. This holds also for each of the 1999 and 2001 data separately. We conclude that there is some as yet unidentified source of correlation in the errors which we have not taken into account, or else they are overestimated by a factor of  $\sim \sqrt{2}$  (which is needed to account for the roughly factor of

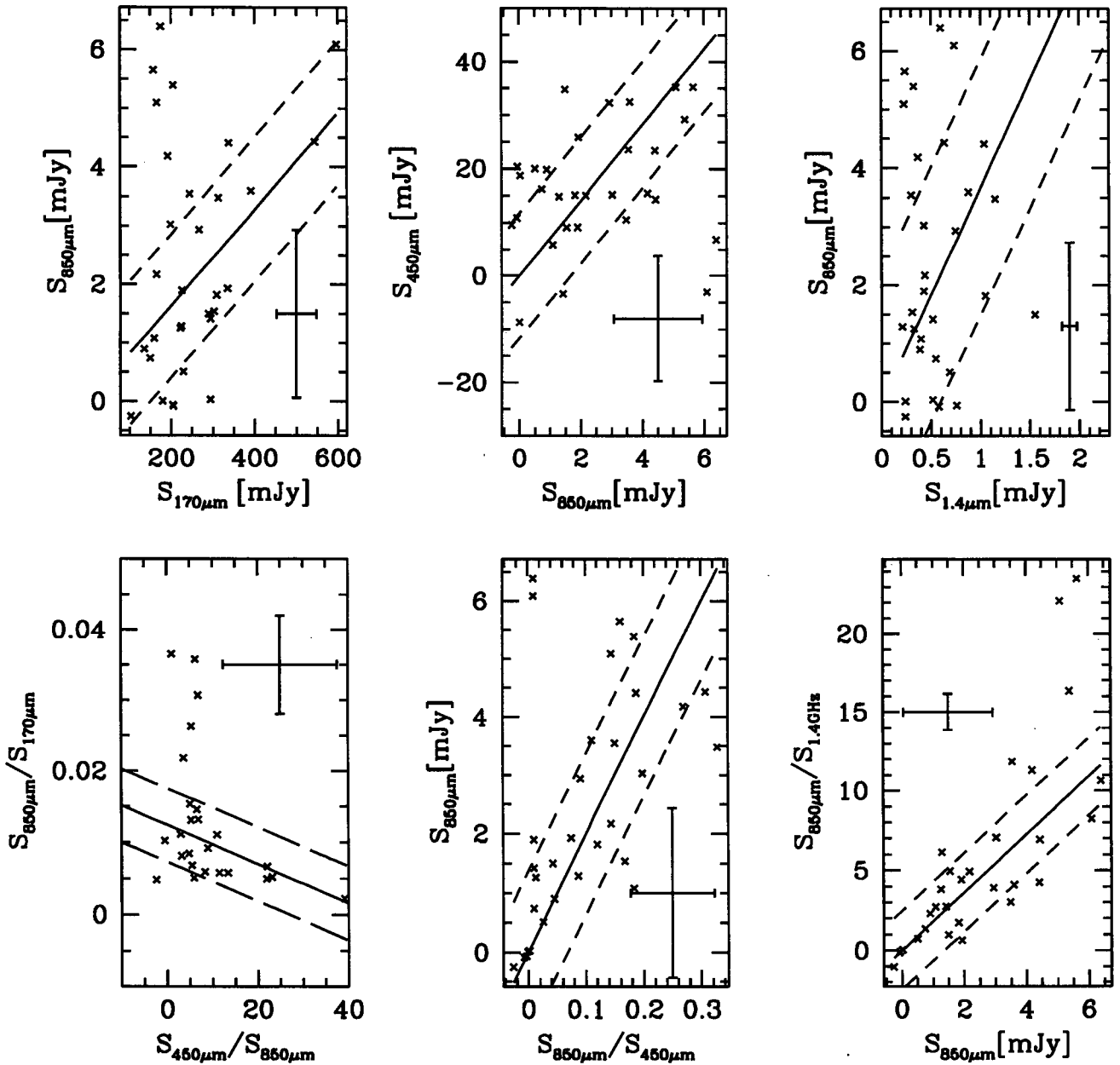


Figure 3.3: The scatter plots with their fits and  $\pm 1\sigma$  scatter. The fit parameters are given in Table 3.2. Notice that the order here is: the first column is mainly sensitive to the location of the thermal peak, the second column to the sub-mm slope, and the third column to the trough between the thermal and non-thermal parts of the SED. The error bars are representative for our data. Extreme outliers are not shown for clarity.

2 discrepancy between the expected and obtained  $\chi^2$ ). We will, however, be conservative and leave the errors as they are, since we cannot properly account for the source of the discrepancy.

After this cautionary aside, we return to Fig. 3.3. It is organized such that in it, the column order roughly follows the main features of the long wavelength SED: the first column is largely sensitive to the thermal peak, the middle column corresponds to the sub-mm slope, and the last column traces the trough between the thermal and non-thermal emission.

First, we will concentrate on the  $S_{850}$  vs.  $S_{170}$  plot. We immediately notice, that after the above described fitting procedure, a number of sources occupy a locus  $> 2\sigma$  away from the best-fit line. Notice that in the colour-colour plot, these five sources stand out again. Assuming a grey-body, these sources are either at higher redshift or lower temperature than the rest of the  $170\mu\text{m}$  sources (or a combination of both).

To understand which, we turn to the  $S_{450}$  vs.  $S_{850}$  plot. Here we are mainly exploring the slope of the spectrum in the sub-mm. What we notice in this plot is that there is not a population of outliers like there was in the  $S_{850}$  vs.  $S_{170}$  plot (the only outliers are N1-001, N1-034, and N1-059 which all have sub-mm slopes which cannot be fit by any sensible dust/redshift combination and thus we assume suffer from some systematic effect such as pointing error – which we discuss more explicitly later. This common distribution implies that a single  $[\beta, T/(1+z)]$  combination describes the sample reasonably well. The lack of outliers, which were present in the  $S_{850}$  vs.  $S_{170}$  plot, means that their location in the previous plot is most likely due to somewhat higher  $z$  rather than a different SED shape. In addition, their redshift cannot be too high – roughly up to  $z \sim 1$  as roughly the shift between  $170\mu\text{m}$  and  $450\mu\text{m}$  (a higher redshift, much warmer population would have to be very finely tuned to still fall on the same distribution, which seems improbable).

For the benefit of later sections, we present in Fig. 3.5 the combined best-fit and confidence levels from both the  $S_{170}/S_{450}$  and  $S_{450}/S_{850}$  slopes. Notice that since there are outliers with discrepant colours, we have somewhat artificially tightened the constraints by using the known best-fit  $S_{450}/S_{850}$  slope, and only allowed for the  $S_{170}/S_{450}$  slope to

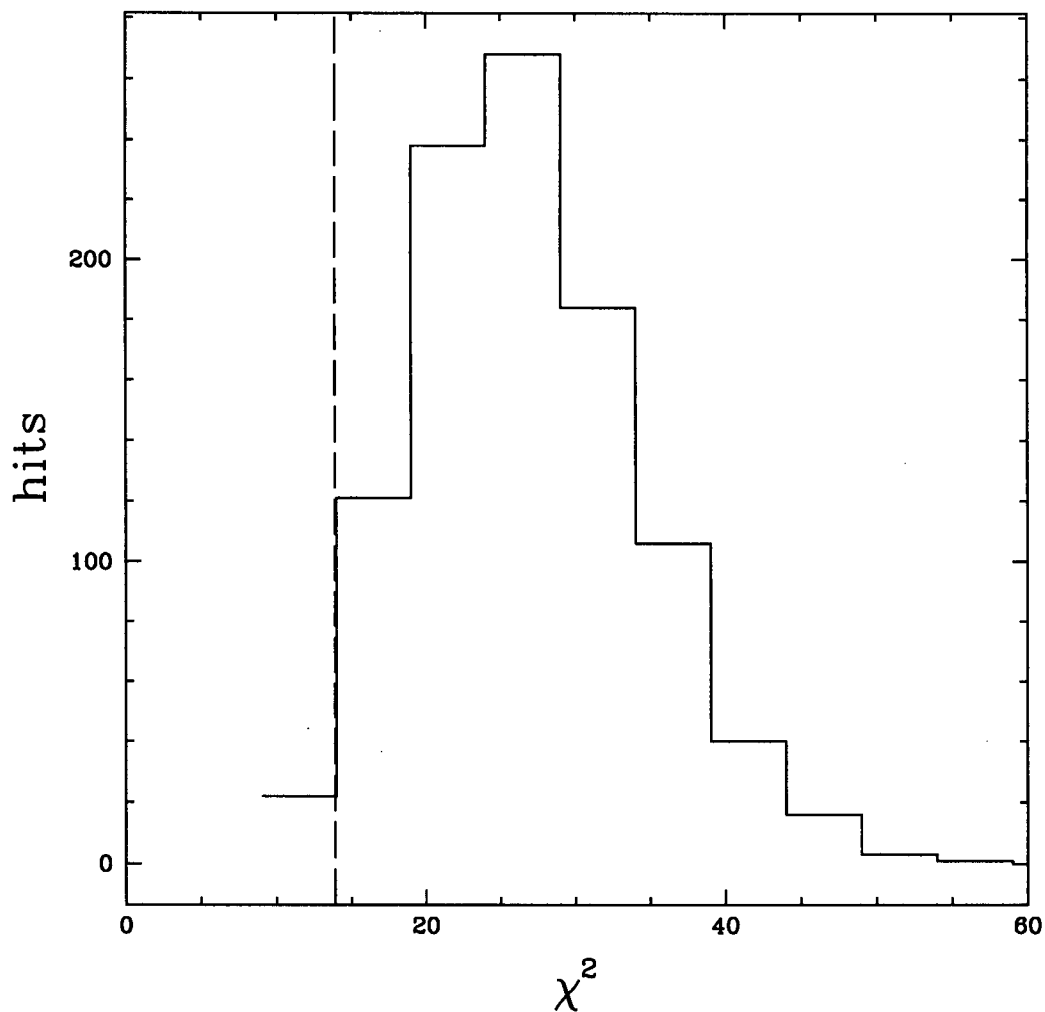


Figure 3.4: The histogram is the result of 1000 Monte Carlo simulations of the sub-mm fluxes of our sample. The dotted line shows the actual value of  $\chi^2$  for the observations. Only about  $\sim 2\%$  of the simulations have a value this low (note that the binning is too crude to show that clearly).

be read off the data directly. This was necessary, since (as can be seen in the figure) the  $\beta$  contours are highly elongated, thus the best-fit value is highly dependent on which sources are included/excluded from the fit. Thus, a more robust approach here is to use our prior knowledge of the best-fit  $S_{450}/S_{850}$  slope (Table 3.2). This only affects the best-fit  $\beta$  value (which is the more uncertain quantity), leaving the best-fit temperature essentially the same.

Notice that since the contours in Fig. 3.5 should be regarded with caution, as different choices of including/excluding outliers, using best-fit slopes, or not affect this (particularly the  $\beta$  value). When we look at the fits from each slope individually, we notice the same thing – the temperature is usually 30 K, but ranges from 20–50 K depending on various choices (i.e. extremely cold and very warm sources are excluded), but the acceptable  $\beta$  range is essentially the entire 1–2 range. It thus seems that Fig. 3.5 roughly represents what we could consider an acceptable range for our sample as a whole. With these caveats in mind, we can assume that it is reasonable to model our data as a single temperature grey body in the limited spectral range considered (i.e.  $170\ \mu\text{m} \rightarrow 850\ \mu\text{m}$ ) provided we explore the effects of varying the parameters within the accepted range we found here. This model is incorrect in detail for the entire thermal spectrum, as has been shown by several authors (e.g. [23], [4], [63], [44]). In general, any grey-body model, be it one, two, or three temperatures, remains only an approximation to the underlying far more complex dust properties. Thus, at this point, we cannot claim much knowledge of the true state of the dusty ISM of our galaxies, but merely seek the best parameters of an equivalent grey-body describing the far-IR/sub-mm spectrum.

We now turn to the third column in Fig. 3.3, where the 5 outliers (except for N1-059 which has an unusually high radio emission) return as such, confirming that indeed redshift, rather than dust properties is the main difference between them and the rest of the sample. The tracking of the trough between the thermal and non-thermal emission is commonly used as a redshift indicator (e.g.[8]). We discuss it in the context of our sample in the following section.



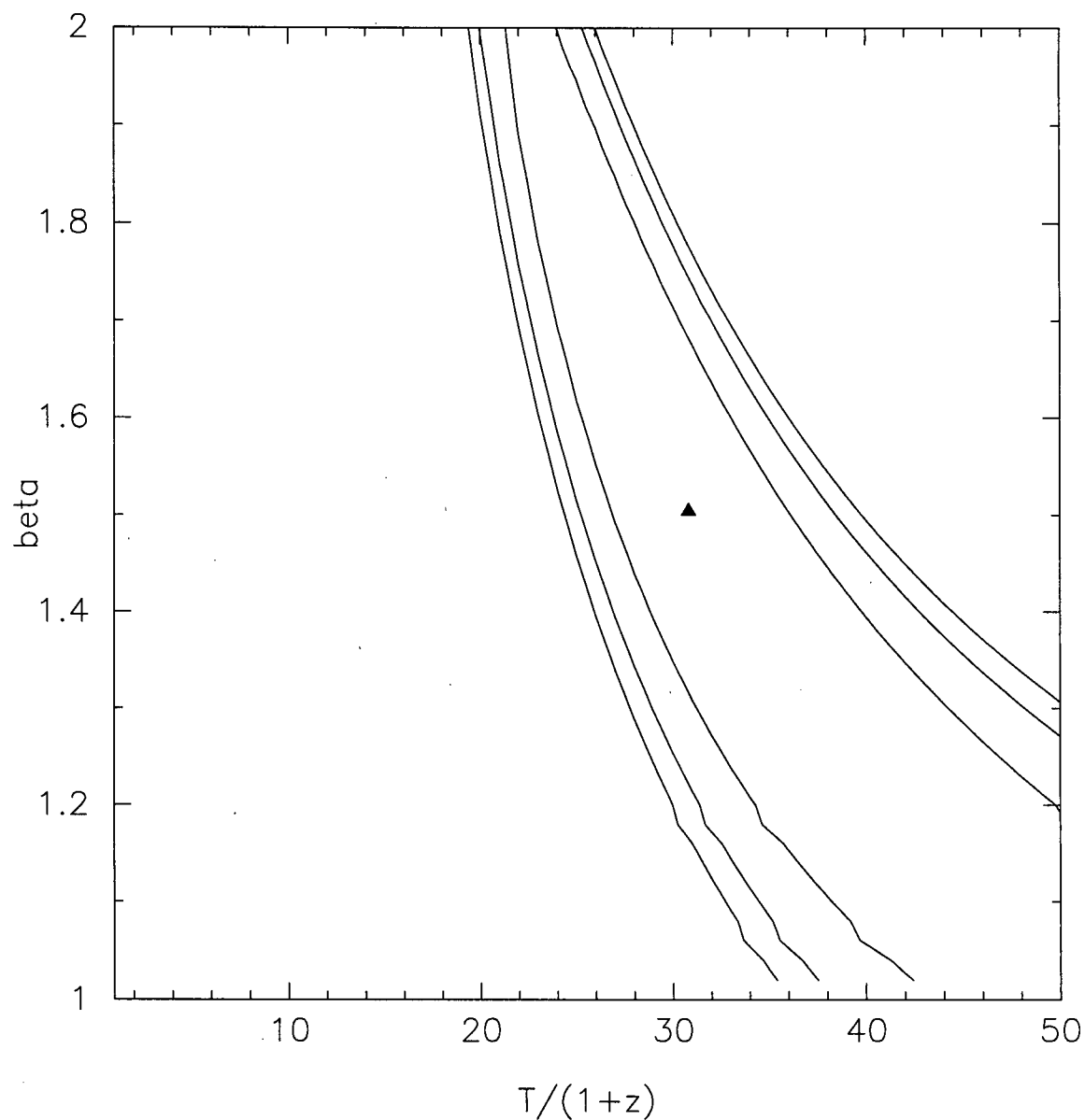


Figure 3.5: The shows the best fit  $[\beta, T/(1+z)]$  combined from the 170/450 and 450/850 slopes, which is  $[1.5, 31 \text{ K}]$  along with the 68, 90, and 95% confidence levels. Notice that  $\beta$  is more poorly constrained. We exclude N1-001, N1-002, N1-034, and N1-059 from the fit due to their discrepant colours.

### 3.3 Sub-mm/Radio redshifts

As described in the introduction,  $S_{850}/S_{1.4\text{GHz}}$  is a redshift indicator [8]. It is, however, degenerate in dust properties for galaxies cooler than  $\sim 60\text{ K}$  [4]. Since we are clearly in that regime (see previous section), here we will look at the relation calibrated on samples with different selections.

The Carilli & Yun relation (CY hereafter) is explicitly:

$$\alpha_{1.4}^{350} = -0.24 - [0.42(\alpha_{\text{rad}} - \alpha_{\text{sm}}) \ln(1+z)], \text{ where } 350\text{ GHz} = 850\text{ }\mu\text{m}. \quad (3.2)$$

For the radio spectral index we use  $-0.75$ , which is fairly typical for a wide variety of sources (particularly optically thin, star-forming galaxies)[6]. For star-forming galaxies, the Rayleigh-Jeans spectrum tends to be  $S_\nu \propto \nu^{3-4}$  (e.g. Arp220 with  $\alpha = 3.4$ , or M82 with  $\alpha = 3.0$ ) [8]. From the best fit  $450\text{ }\mu\text{m}$  to  $850\text{ }\mu\text{m}$  slope of our sample (Table 3.2), we arrive at  $\alpha_{\text{sm}} = 3.1 \pm 0.2^1$ , although this is based on the mean source, and there are many outliers.

Eq-n 3.2 is well parametrized (for the mean galaxy in the CY sample of 17 which include radio-loud galaxies) by a fourth order polynomial in  $\alpha$  (i.e.  $\alpha_{1.4}^{350}$ ) such that [8]:

$$z_{\text{CY}} = 0.050 - 0.308\alpha + 12.4\alpha^2 - 23.0\alpha^3 + 14.9\alpha^4. \quad (3.3)$$

A different parametrization is derived for the SLUGS (SCUBA Local Universe Galaxy Survey) sample by Dunne, Clements & Eales [24] (DCE hereafter), which selection has more dusty local galaxies, many of which show significant cold dust components [23]. Their result is:

$$z_{\text{DCE}} = 0.551 - 6.652\alpha + 25.57\alpha^2 - 30.56\alpha^3 + 13.75\alpha^4. \quad (3.4)$$

In Fig. 3.4 we compare the two, and overlay 5 of our sources which have spectroscopic redshifts. Notice that N1-040 ( $z = 0.45$ ) and N1-064 ( $z = 0.91$ ) are reasonably well

<sup>1</sup>The spectral index is defined as  $\alpha = \frac{\log[S_{450}/S_{850}]}{\log[850/450]}$  and so the associated error is  $\log e(S_{850}/S_{450}) \sqrt{(\frac{\Delta S_{850}}{S_{850}})^2 + (\frac{\Delta S_{450}}{S_{450}})^2} / \log(850/450)$ . The values for  $\alpha_{1.4}^{350}$  were found in an analogous way. In general we use the convention  $\log = \log_{10}$  and  $\ln = \log_e$ .

described by the DCE relation, but in general, their redshifts are overestimated by the CY relation. The local galaxies on the other hand, are poorly fit by either relation. This may suggest that the local FIRBACK selection represents a different population than those selected using IRAS. This is sensible since we have no indication of our local sample being IRAS-bright.

In Table 3.3, we explicitly derive the redshifts for our sample using both of these relation, as well as from eq. 3.2 with individual spectral indices for each source. We also list the sub-mm/radio and sub-mm spectral indices as a guide to interpreting some of the derived redshifts. Notice that the DCE relation vastly overestimates the redshift of very low (or negative)  $\alpha$  sources. A source such as N1-002 ( $z_{\text{spec}}=0.07$ ) which has a high  $\alpha$  value has its redshift poorly estimated by all of these methods (it is even outside the CY quoted uncertainty of  $\sim 0.5$ ). DCE quote smaller errors; however, they fail to fit our local galaxies (their sample is local but IRAS-bright and thus may have somewhat different dust properties). We discuss the effects of selection in Chapter 5.

We conclude that such relations, although useful in estimating the redshift distribution of sources over larger  $z$ -ranges, provide too weak a constraint locally, due to the large scatter in intrinsic galaxy properties (giving an uncertainty of  $\Delta z \sim 0.5$ ). However, as a very crude redshift indicator this approach still confirms our prior selection of N1-040, N1-064, N1-059, N1-078, and probably N1-048 as being at somewhat higher redshifts than the rest of the galaxies in our sample.

### 3.4 Sub-mm vs. near-IR

Here we examine the correlation between the  $K$  magnitude and  $850\mu\text{m}$  fluxes of our sources. The  $S_{850}$  flux density by itself is not a good redshift indicator due to its  $k$ -correction behavior. It is however a good luminosity tracer. The  $K$  magnitude (in the restframe) is also a luminosity indicator; as it is 10 times less obscured than the optical. The  $S_{850}$  to  $K$  magnitude relation can be used as a redshift indicator [3, 18] because of the rest-frame shorter wavelengths (that are much more dust obscured) moving with

Table 3.3: The sub-mm/radio spectral indices and derived redshifts

Source	$\alpha_{1.4}^{350}$	$\alpha_{\text{sm}}$	$z_{\text{our}}^a$	$z_{\text{DCE}}^b$	$z_{\text{CY}}^c$
N1-001	0.38±0.07	0.00±0.00	0.00	0.34	0.78
N1-002	0.35±0.05	1.85±1.41	0.72	0.26	0.71
N1-004	0.26±0.08	3.46±0.70	0.32	0.07	0.46
N1-007	0.26±0.07	2.62±0.79	0.43	0.08	0.48
N1-008	-0.08±0.10	4.08±1.22	0.08	1.25	0.16
N1-009	0.20±0.08	1.75±1.31	0.52	0.02	0.33
N1-010	0.10±0.14	3.33±1.62	0.22	0.11	0.12
N1-012	0.29±0.20	2.81±2.38	0.43	0.13	0.55
N1-013	0.00±0.00	10.12±78.61	-0.06	0.00	0.00
N1-015	0.18±0.21	0.00±0.00	0.00	0.02	0.29
N1-016	-0.01±0.14	4.94±1.44	0.10	0.59	0.05
N1-024	0.25±0.08	3.77±0.79	0.29	0.06	0.44
N1-029	-0.06±0.62	5.77±5.48	0.07	1.00	0.11
N1-031	0.27±0.11	2.48±2.44	0.46	0.09	0.50
N1-032	0.33±0.21	3.84±1.94	0.34	0.21	0.65
N1-034	0.24±0.19	6.80±1.65	0.17	0.06	0.43
N1-039	0.00±0.00	0.00±0.00	0.00	0.00	0.00
N1-040	0.51±0.04	2.66±1.15	0.69	0.68	1.07
N1-041	0.00±0.00	0.00±0.00	0.00	0.00	0.00
N1-045	0.36±0.09	2.54±1.12	0.54	0.27	0.71
N1-048	0.44±0.05	2.06±1.25	0.78	0.49	0.92
N1-056	0.00±0.00	0.00±0.00	0.00	0.00	0.00

Table 3.3: *continued...*

Source	$\alpha_{1.4}^{350}$	$\alpha_{\text{sm}}$	$z_{\text{our}}^a$	$z_{\text{DCE}}^b$	$z_{\text{CY}}^c$
N1-059	$0.43 \pm 0.06$	$0.12 \pm 7.89$	5.30	0.46	0.89
N1-064	$0.56 \pm 0.05$	$3.04 \pm 0.73$	0.66	0.84	1.20
N1-068	$0.29 \pm 0.12$	$3.05 \pm 1.29$	0.40	0.13	0.55
N1-077	$0.18 \pm 0.22$	$2.67 \pm 2.72$	0.34	0.02	0.28
N1-078	$0.58 \pm 0.05$	$2.88 \pm 0.54$	0.71	0.88	1.23
N1-083	$0.05 \pm 0.29$	$4.86 \pm 2.95$	0.13	0.26	0.07
N1-101	$0.15 \pm 0.31$	$4.86 \pm 2.72$	0.18	0.03	0.22
N1-153	$0.00 \pm 0.00$	$0.00 \pm 0.00$	0.00	0.00	0.00
N2-013	$0.45 \pm 0.08$	$2.97 \pm 1.22$	0.56	0.52	0.94

<sup>a</sup> Derived from the CY relation (eq. 3.2) using our measured values of  $\alpha_{\text{sm}}$  and fixing  $\alpha_{1.4}^{350} = -0.75$ .

<sup>b</sup> Derived from the relation of DCE [24].

<sup>c</sup> Redshifts derived using the CY [8] 4th order polynomial fit.

Note that, we have set to zero all instances when  $\alpha_{\text{sm}} < 0$ . At negative  $\alpha_{1.4}^{350}$  the DCE relation gives unphysical values.

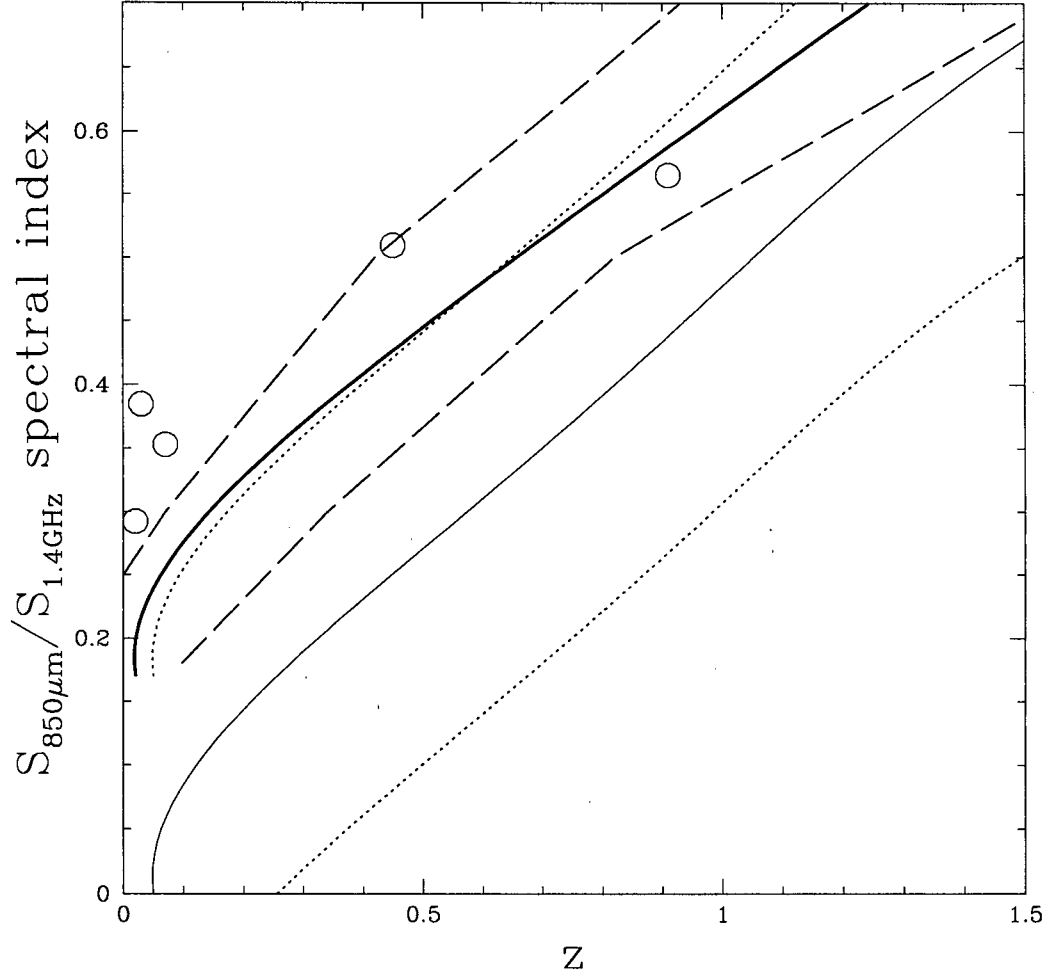


Figure 3.6: The sub-mm/radio spectral index as a redshift indicator. The thick solid line is the relation based on the SLUGS sample (104 galaxies - IRAS selected), with the dashed lines being its  $\pm 1\sigma$  envelope. The thin solid line is the standard CY relation [8] (17 galaxies - IRAS and NRAO selection) with dotted  $\pm 1\sigma$  envelope. The circles are 5 galaxies from our sample with spectroscopic redshifts.

increasing redshift into the observer-frame near-IR. Thus the  $K$  magnitude for a given sub-mm flux is dependent on both redshift and dust obscuration. Fig. 3.5 plots the flux at  $850\,\mu\text{m}$  against  $K$  magnitude, where the higher- $z$  sources clearly populate a different locus from the nearby galaxies. They are roughly  $3\sigma$  removed from the best-fit line for the other sources, with a distinct gap between the two groups (apart perhaps from two sources which we discuss later). The gap is more pronounced than in Fig. 3.3 as here the  $(1+z)/T_d$  degeneracy is somewhat broken.

Using the 6 spectroscopic redshifts available (see beginning of chapter), we fit a model for  $\ln(1+z) = aK + b\log(S_{850}) + c$ , arriving at the lines overlaid in the figure. Explicitly,

$$\ln(1+z) = (0.07 \pm 0.03)K + (0.09 \pm 0.30)\log(S_{850}) - (0.86 \pm 0.39). \quad (3.5)$$

This should be interpreted as only a very rough indicator of redshift, since only 6 sources were used in the fit. Due to the parameter space not being equally sampled, there is little sensitivity for varying sub-mm flux for a given  $K$  magnitude. In particular, information is lacking at the faint sub-mm/faint near-IR end.

The fact that the  $K$ -magnitude of distant faint galaxies can be used as a redshift indicator was also discussed in a recent paper by Willot et al. [66] who derive the following relation from their sample of radio galaxies:

$$K = 17.37 + 4.53\log_{10} z - 0.31(\log_{10} z)^2. \quad (3.6)$$

We compare this (dashed line) with our relation (solid line) in the bottom panel of Fig. 5.6. Since ours is more heavily biased towards local, starforming galaxies, whereas Willot et al.'s relation is based on radio galaxies, these lines can be regarded as a rough envelope encompassing a wide variety of galaxy types. A redshift relation based solely on the  $K$  magnitude is bound to be degenerate in some other galaxy properties (amount of dust, luminosity etc), and can only work for a very homogeneous sample of galaxies. The addition of sub-mm flux would make this relation more general as the  $K$ -band is dust absorption attenuated (specifically for distant, luminous galaxies), whereas the sub-mm flux is due to dust emission, and thus the combination of the two will somewhat break

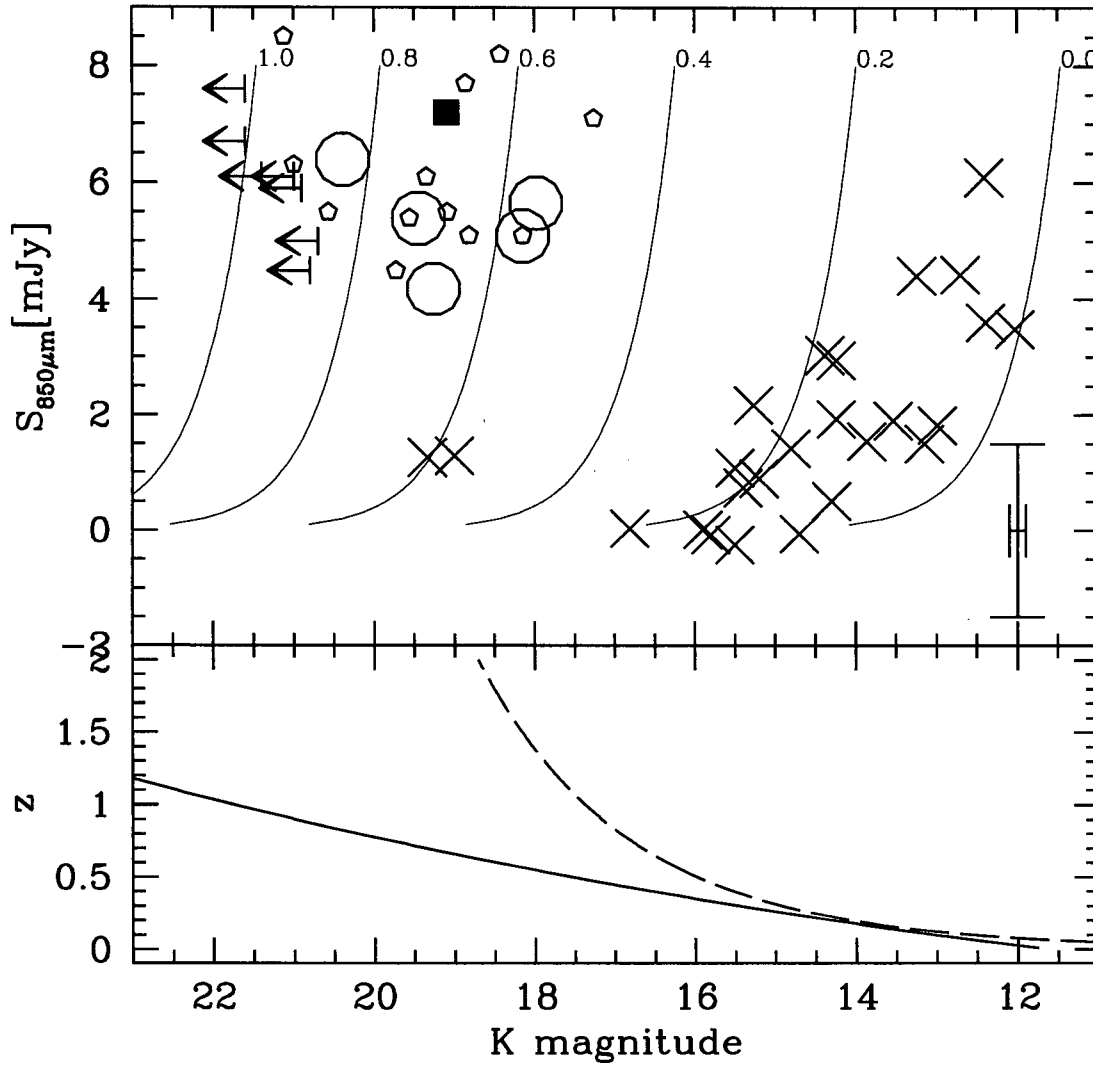


Figure 3.7:  $S_{850}$  vs  $K$  magnitude for our sample (crosses and circles). The filled squares and  $K$ -band upper limits are from the lens survey of Smail et al. [61], while the pentagons are from the UK 8 mJy survey [40]. The circles are our high- $z$  candidates which populate a similar region to these SCUBA survey sources. The lines are the results from fitting a model to the 6 sources where  $z_{\text{spec}}$  is available (see text) and are labelled with redshift. The bottom panel shows the  $K$ - $z$  relationship obtained above (solid, for  $S_{850}=5$  mJy), compared with the Willot et al. [66] relation for radio galaxies (dashed). The error bar in the lower right-hand corner is a representative one for our measurements.



the dust degeneracy. This diagnostic of both the absorption and emission spectrum, would allow for a more robust redshift indicator over different galaxy types, although our particular relation is not well constrained due to the limited spectroscopic sample. However, it is clear that in general, objects which are detected at  $850\,\mu\text{m}$ , and are faint at  $K$ -band, are at higher redshift.

The two possible exceptions to this are the sources N1-032, and N1-034 which have  $K$  magnitudes of  $\sim 19$  and sub-mm fluxes of  $\sim 1\,\text{mJy}$ . Without redshifts and other detailed follow-up, it is not clear what their nature is and why they occupy this part of the diagram. One possibility is multiple sources within the beam and related confusion issues. We can use the predictions of the galaxy evolution model of Devriendt et al. [20] for the  $K$  magnitudes and sub-mm fluxes for a variety of galaxy types to estimate the most likely type of source to occupy this location. It appears that a LIRG galaxy (such as M82) at  $z \sim 0.3$  would be similarly faint at both sub-mm and near-IR bands. Although this is not a robust conclusion, it appears to be in reasonable agreement with both the sub-mm/radio redshift estimates (Table 3.3) and the unexceptional location of these galaxies in our scatter plots. Note however that N1-034 has the highest  $450\,\mu\text{m}$  detection of our sample which (coupled with the low  $850\,\mu\text{m}$  signal) we cannot easily explain with a single source.

### 3.5 SED fits

We now fit single grey-body SEDs to the  $170\,\mu\text{m}$ ,  $450\,\mu\text{m}$ , and  $850\,\mu\text{m}$  fluxes of each source (see Fig. 3.8). As discussed previously, we assume optically-thin sources. The effect of including a non-negligible  $\tau$  in the fits is (as described by Blain et al. [4]) to suppress the peak with respect to the Rayleigh-Jeans tail such that the best-fit dust temperature inferred will be 10–20% higher than otherwise. This is therefore not an important effect for sub-mm spectra dominated by single temperature dust emission (to the precision of our fits of three points). In order to avoid stretching that assumption too much, we only use the  $170\,\mu\text{m}$ ,  $450\,\mu\text{m}$ , and  $850\,\mu\text{m}$  points in the fits, where the SED

Table 3.4:  $\chi^2$ -range occupancy for various  $\beta$  fits.

$\beta$	$\chi^2=0-1$	$\chi^2=1-2$	$\chi^2 > 2$
1.3	15	6	10
1.5	20	5	6
1.7	22	4	5
1.9	18	2	11

is dominated by the coldest significant dust component.

We fit for two parameters ( $\beta$  is held constant) – the overall normalization, which gives the luminosity (if the redshift is known), and the wavelength shift, which is proportional to  $(1+z)/T_d$ . The best fit  $\chi^2$  and fit parameters were obtained with the PIKAIA genetic algorithm [12]. With only 3 points for each galaxy, we could not also fit for  $\beta$ . However, we are able to investigate how different values of  $\beta$  would affect the quality of fits for the sample as a whole. Table 3.4 shows the distribution of  $\chi^2$  values derived from fitting the SEDs with various  $\beta$  values. We can see that for the sample as a whole values of  $\beta = 1.5 - 1.7$  are far better than either smaller, or larger values. The sources, with a poor fit in all cases are: N1-001, N1-002, N1-015, N1-034, and N1-056. For the lowest  $\beta$  tested, 5 additional sources show a poor fit: N1-008, N1-009, N1-012, N1-013, N1-016 (note that these are all among the brighter ISO sources from our sample). On the other hand, the high  $\beta = 1.9$  value, provides a poor fit for all the sources we singled out in the previous section as potentially being at higher redshifts. For local ULIGs, previous studies [23, 44] already show this trend, with lower  $\beta$  providing a better fit when single temperature greybodies are used, whereas generally a  $\beta \sim 2$  is inferred for multi-temperature fits. Our sample is generally faint enough that apart from those significantly redshifted, none of our sources compare with local ULIGs. Thus they may be more comparable to the thermal spectrum characteristics of normal starforming galaxies.

In a previous section we showed that the best-fit  $\beta$  for our sample was around 1.5 (although with large uncertainties). We show the results for this  $\beta$  in Table 3.5, and show

the SEDs in Fig. 3.8. Notice in particular that indeed the sub-mm slopes are generally well fit, and the fits fail (when they do) at the  $170\ \mu\text{m}$  point which tends to be above the curve. Conversely, when a  $\beta$  of 1.9 is used, the failed fits generally have their sub-mm points above the curve, which is suggested by the best fit  $(\beta, T)$  from the  $170\ \mu\text{m}/850\ \mu\text{m}$  slope. This suggests that, even if more than one is present, a single dust component dominates the far-IR/sub-mm emission for these sources. Among the  $S_{850} < 3\sigma$  sources, the one which is not well fit by our simple model is N1-034, which has an anomalously high  $450\ \mu\text{m}$  flux. Besides this one, which does not appear to be easily fit even with a 2-component SED, there are a few sources with a somewhat higher  $\chi^2(2-3)$ , suggesting that a combination SED (i.e. one with a warm and a cold component) might provide a better fit, although this could not be reliably investigated with these data alone. Notice that, in Fig. 3.8, we overlay the IRAS  $100\ \mu\text{m}$  points are not in the fits. For about half the sources, the  $100\ \mu\text{m}$  fluxes are clearly lower than the fit. However they are all on or above the fit for those sources suspected to be at somewhat higher-redshift (i.e. above  $z \sim 0.2$  from Table. 3.5 using a generous temperature of 40 K).

### 3.6 Luminosity and SFR

In this section, we wish to examine some of the physical characteristics of our sample. Since, fundamentally, the dust properties/distance degeneracy is still present, all such derivations are highly uncertain. However, we will provide such physical parameters for what we consider to be reasonable ranges of redshifts (for the likely higher redshift sources only) in order to allow for some comparison with other studies, and some handle on the physical nature of our sources. We also calculate these for all sources with available spectroscopic redshifts.

We somewhat arbitrarily decide on the  $(\beta, T_d)$  combinations which both agree with the fit results presented in Fig. 3.5, with the redshift estimated from the sub-mm/radio, and sub-mm/near-IR relations, and are in general agreement with expectations from other studies (see Chapter 5). These are (1.7, 30 K), and (1.5, 40 K). Table 3.6 shows the considered

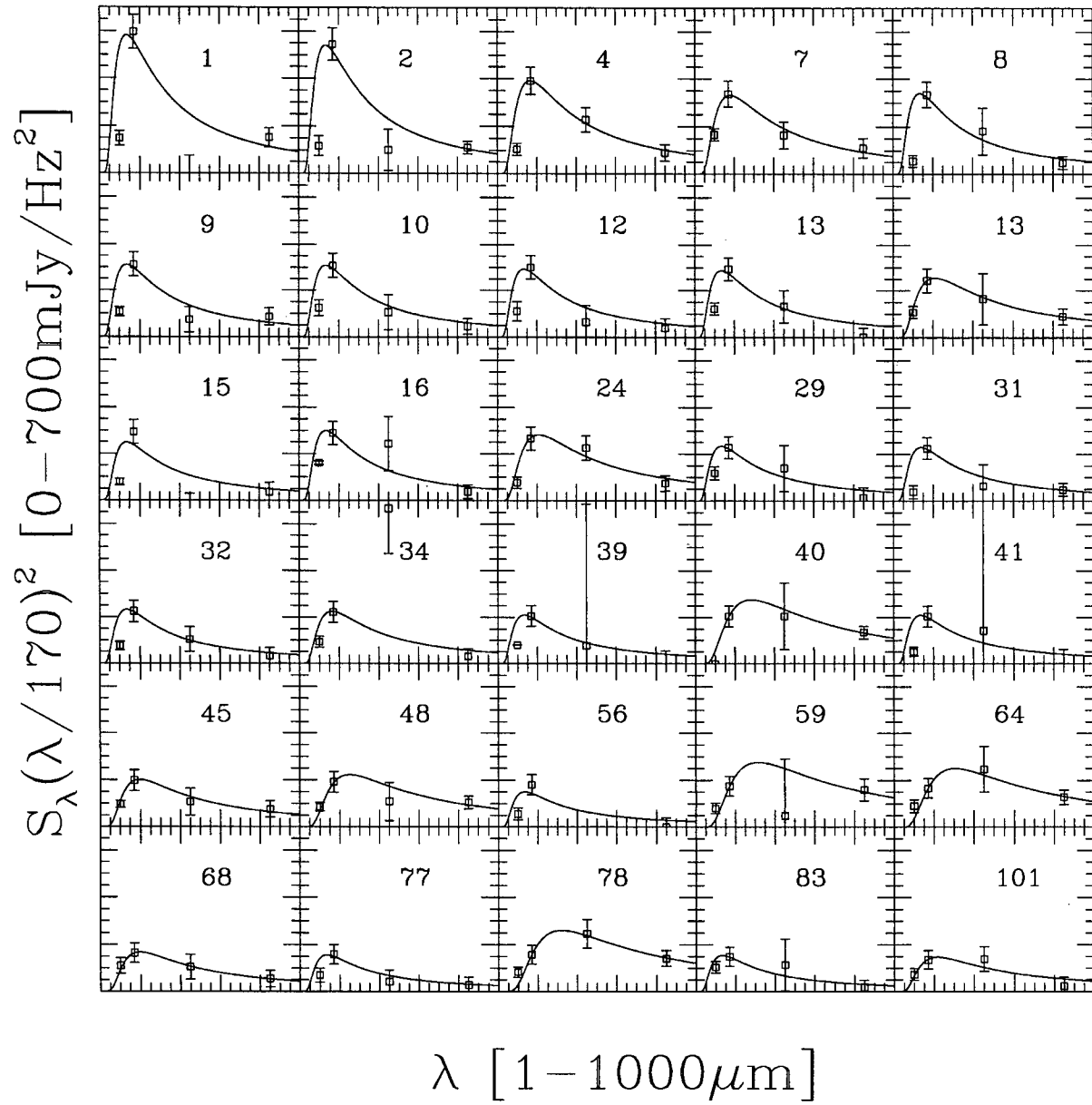


Figure 3.8: The SED fits for our sample with  $\beta = 1.5$ . The  $x,y$ -ranges in all panels are the same (shown in the labels), and the sources are arranged with decreasing 170  $\mu\text{m}$  flux. The IRAS 100  $\mu\text{m}$  point is not used in the fit. For the sake of clarity, we rescale the flux via  $(\lambda/170\mu\text{m})^2$ .

Table 3.5: Fit results for  $\beta = 1.5$ .

Source	$T_d/(1+z)$	$\chi^2$	$z(T_d = 30K)$	$z(T_d = 35K)$	$z(T_d = 40K)$
N1-001	47.96	8.84	0.00	0.00	0.00
N1-002	47.96	2.45	0.00	0.00	0.00
N1-004	38.47	0.20	0.00	0.00	0.04
N1-007	35.97	0.44	0.00	0.00	0.11
N1-008	47.96	0.63	0.00	0.00	0.00
N1-009	47.96	1.83	0.00	0.00	0.00
N1-010	47.96	0.38	0.00	0.00	0.00
N1-012	47.96	1.16	0.00	0.00	0.00
N1-013	47.96	2.35	0.00	0.00	0.00
N1-015	47.96	7.25	0.00	0.00	0.00
N1-016	47.96	1.50	0.00	0.00	0.00
N1-024	30.82	0.99	0.00	0.14	0.30
N1-029	47.96	0.75	0.00	0.00	0.00
N1-031	46.54	0.17	0.00	0.00	0.00
N1-032	47.96	0.14	0.00	0.00	0.00
N1-034	39.30	8.72	0.00	0.00	0.02
N1-039	47.96	0.57	0.00	0.00	0.00
N1-040	22.74	0.05	0.32	0.54	0.76
N1-041	47.96	0.47	0.00	0.00	0.00
N1-045	32.69	0.25	0.00	0.07	0.22
N1-048	25.72	0.80	0.17	0.36	0.56
N1-056	47.96	5.80	0.00	0.00	0.00
N1-059	20.40	0.74	0.47	0.72	0.96
N1-064	21.16	0.08	0.42	0.65	0.89

Table 3.5: *continued...*

Source	$T_d/(1+z)$	$\chi^2$	$z(T_d = 30K)$	$z(T_d = 35K)$	$z(T_d = 40K)$
N1-068	32.70	0.00	0.00	0.07	0.22
N1-077	47.96	0.31	0.00	0.00	0.00
N1-078	20.03	0.03	0.50	0.75	1.00
N1-083	47.96	0.34	0.00	0.00	0.00
N1-101	29.69	1.11	0.01	0.18	0.35
N2-013	30.69	0.01	0.00	0.14	0.30

redshift ranges, luminosities<sup>2</sup>, and distances for the sources in our sample which are likely at non-zero redshift (at the resolution of our fits). The ranges illustrate how the values vary with input parameters, and also the qualitative agreement over a range of parameters. The sources in the upper half of the table are our  $S_{850} > 3\sigma$  detections (excluding N1-001, and N1-002). They are consistent with  $z \sim 0.4 - 0.9$  ULIGs – based on the average luminosity of the sample in the given range being above  $10^{12}L_{\odot}$ . The likely lowest luminosity, and redshift source of this set is N1-048 which may even be only a Luminous Infrared Galaxy (LIG) depending on the exact dust parameters. The bottom half of Table 3.6 contains five LIG candidates (N1-101, N2-013, N1-024, N1-068, and N1-045) based on the considered range in dust parameters.

The only surprise here is N1-008 since, with its  $z_{\text{spec}} = 0.26$ , it should have been grouped with the above. Possible explanations for its omission are: 1) its dust properties are too far outside the considered range, and 2) it is affected by confusion. The second one is more likely as there are two radio sources within the ISO beam (see Fig.3.2). In an upcoming observing run, we plan to observe the second radio source with SCUBA which should allow us to disentangle the contribution of each radio source to the total far-IR flux, and thus, potentially, bring our photometric estimate in better agreement with the

---

<sup>2</sup>We solve for the luminosity simply by integrating our fitted SEDs. This is not entirely accurate, however, is sufficient given the far larger systematic uncertainties (such as the unknown  $T_d$ ). The key mathematical step is the integral  $\int_0^{\infty} x^{s-1}(e^x - 1)^{-1} dx = \Gamma(s)\zeta(s)$ .

Table 3.6: Fit results for the higher- $z$  sources<sup>a</sup>

Source	$z$	$\log(L)$ [ $L_{\odot}$ ]	$D_L$ [Mpc]
N1-078	0.66-1.00	12.14-12.63	3662-6121
N1-059	0.64-0.96	12.16-12.64	3526-5854
N1-064	0.58-0.89(0.91)	12.07-12.56	3180-5326
N1-040	0.49-0.76(0.45)	12.01-12.53	2580-4372
N1-048	0.33-0.56	11.65-12.26	1632-2989
N1-101	0.18-0.35	11.02-11.79	807-1711
N2-013	0.15-0.30	11.14-11.93	684-1462
N1-024	0.14-0.30	11.11-11.97	621-1434
N1-068	0.08-0.22	10.41-11.53	329-1031
N1-045	0.08-0.22	10.46-11.61	320-1031

<sup>a</sup> The ranges correspond to different  $(\beta, T_d)$  combinations the first being (1.7, 30 K) the second (1.5, 40 K). The redshifts in brackets are spectroscopic. The top half of the table has the  $> 3\sigma$  detections while the bottom half has the other sources from the sample with non-zero redshifts from our fits. The sources are arranged by decreasing redshift.

spectroscopic redshift.

Based on our available data we have two routes to estimating the SFR.

The first SFR estimator we consider is the based on the FIR luminosities. The idea behind this is that, the thermal dust emission is reprocessed stellar light which was absorbed primarily in the UV (i.e. where young stars are the primary contributors). For a review discussion of the uncertainties associated with this and other SFR estimators see Schaerer 1999 [56]. Essentially, the problem is to find a universal calibration given the vastly varying conditions (e.g. different dust properties, and contribution of cirrus, old stars, or AGN to the thermal spectrum) from galaxy to galaxy. One parametrization is  $SFR = \alpha \times 10^{-10} L_{FIR}/L_{\odot} [M_{\odot} yr^{-1}]$ , where  $\alpha = f(\text{IMF})$  if we neglect all the above uncertainties and calibrate the SFR based on stellar evolution models alone. Here we adopt the form of Charlot et al.[13], which is based on a Salpeter IMF and is as follows:

$$SFR = 1.7 \times 10^{-10} \frac{L_{FIR}}{L_{\odot}} [M_{\odot} yr^{-1}]. \quad (3.7)$$

The second is based on the radio continuum, where the idea is essentially the same as above and use is made of the well known far-IR/radio correlation (see discussion in Chapter 1). Here we largely follow Yun et al. [68] who derive the empirical relations based on IRAS galaxies with radio observations.

$$SFR(M_{\odot} yr^{-1}) = (5.9 \pm 1.8) 10^{-22} L_{1.4GHz} (WHz^{-1}) \quad (3.8)$$

The radio luminosity is obtained via

$$\log L_{1.4GHz} (WHz^{-1}) = 20.08 + 2 \log D + \log S_{1.4GHz} \quad (3.9)$$

where  $D$  is in Mpc and  $S_{1.4GHz}$  is in Jy. We use both these methods to estimate the SFRs for the non-zero redshift sources. The results are presented in Table 3.7. The two estimators agree with each other reasonably well (as can be expected). The strongest deviation is observed for N1-059, however that source has a greater radio flux by a factor of roughly  $\sim 2$  from its peers. In general estimates for lower luminosity sources are more affected by the various systematic uncertainties discussed above.



Table 3.7: Estimating the Star Formation Rates<sup>a</sup>.

Source	$z$	$\text{SFR}_{1.4\text{GHz}}[M_{\odot}\text{yr}^{-1}]$	$\text{SFR}_{\text{FIR}}[M_{\odot}\text{yr}^{-1}]$
N1-078	0.66-1.00	228-638	235-725
N1-059	0.64-0.96	529-1459	246-742
N1-064	0.58-0.89(0.91)	165-463	200-617
N1-040	0.49-0.76(0.45)	156-447	174-576
N1-048	0.33-0.56	70-235	76-309
N1-101	0.18-0.35	18-81	18-105
N2-013	0.15-0.30	10-45	23-145
N1-024	0.14-0.30	21-109	22-159
N1-068	0.08-0.22	3-33	4-58
N1-045	0.08-0.22	3-32	5-69

<sup>a</sup> This table is arranged in an analogous way to Table 3.6.

# CHAPTER 4

## A MODEL

In this chapter we present a simple phenomenological model that reproduces the main characteristics of the observed distribution of fluxes for our FIRBACK targets.

Our goal is a model for  $N(z)$  expected from our selection criteria. This involves determining the luminosity function (LF) as a function of  $z$ , and the limiting flux per  $(L, z)$  pair as determined from evolving reasonable SED templates. A specific cosmological model needs to be used to determine the distance and volume element (ie  $dV/dz$ ) variation with redshift. The cosmological relations leading to these are presented in Appendix B.

First, we start with the  $z$ -dependent LF. The main premise of the model involves the separation of the galaxy population into a quiescent component and a ULIG component, and then to evolve the two separately. This rather approximate treatment is inspired by the IRAS local LF where the previously unknown luminous dusty galaxies modify the shape to be more like a double power law rather than the exponentially declining (at high luminosities) Schechter function of normal galaxies [55]. On the other hand, at high- $z$ , no-evolution models completely fail to fit the observed number counts (e.g.[21]). Since less luminous, quiescent galaxies will likely not contribute much to higher- $z$  counts (due to selection), evolving the higher luminosity population is a reasonable approximation. A similar phenomenological model has been carried out by Lagache et al. [45].

We thus use a luminosity function of the combined form:

$$\phi = \phi_{\text{Schechter}} + \phi_{\text{ULIG}} \quad (4.1)$$

where the Schechter luminosity function has the form:

$$\phi_{\text{Schechter}} = \phi_s^* \left( \frac{L}{L_s^*} \right)^{\alpha_s} e^{-L/L_s^*}. \quad (4.2)$$

For the quiescent galaxies we use  $\alpha_s = -0.4$ ,  $\phi_s^* = 7 \times 10^{-4} \text{Mpc}^{-3} \text{Mbol}^{-1}$ , and  $L_s^* = 10^{11} L_{\odot}$ . The ULIG LF we use behaves in the opposite way – it cuts off exponentially at smaller

luminosities and is a power law at higher luminosities, where the Schechter function is exponentially cut off. Explicitly, the ULIG LF we use is:

$$\phi_{\text{ULIG}} = \phi_u^* \left( \frac{L}{gL_u^*} \right)^{\alpha_u} e^{-(L_u^*/L)f} \quad \text{with} \quad g = (1+z)^4, \quad (4.3)$$

where  $\alpha_u = -2.5$ ,  $\phi_u^* = 1 \times 10^{-4} \text{Mpc}^{-3} \text{Mbol}^{-1}$ ,  $L_u^* = 2 \times 10^{11} L_\odot$ , and  $f$  is a fudge factor to smooth over the gap of the two components due to the strong evolution. It has the form  $1/(1+z)^{0.3}$ . Thus the combination of the two essentially results in two power laws in the local Universe to match observations: typically, the knee is estimated at  $1 - 5 \times 10^{11} L_\odot$  [14], and the ULIG slope at  $-2.2$  [55]. Clearly, there are degeneracies between the various parameters in such phenomenological modelling. We chose the ensemble of values to be such as to make our particular parametrization fit the local LF. The luminosity evolution of  $(1+z)^4$  is assumed based on models in the literature [67].

We must break this evolution at some point (to avoid running into infinities). We do so by freezing the evolution at  $z=1$  (which is also our range of interest). This is similar to the step taken by Xu [67] who freeze the evolution at  $z = 1.5$ .

We do not explicitly consider number evolution (as from merging); however, note that the fudge factor above acts slightly as a luminosity-dependent density evolution (although with an awkward parameterization). In general, the observations can be fit also either by pure number evolution or a combination of number and luminosity evolution within a variety of parameterizations of the LF (e.g. [45], [14], [33], [67]). A more decisive test of the validity of a particular model is how well does it reproduce the observed intensity of the CIB for example. We have not performed such a test, thus the model at present lacks true robustness, but is sufficient to our purposes.

To obtain the flux at some wavelength for a given luminosity and redshift, we use a cold and a starburst galaxy templates (for each of the two components) [45] and evolve them with redshift. These are compared in Fig. 4.2 which also highlights the effect of cold dust on the SED shape. Fig. 4.3 shows an example of a  $L \approx 10^{12} L_\odot$  spectral template being evolved from  $z = 0.1 - 5$ . The templates are evolved with redshift using

$$S_{\nu_o} d\nu_o = \frac{L_{\nu_e}}{4\pi D_L^2} d\nu_e \quad (4.4)$$

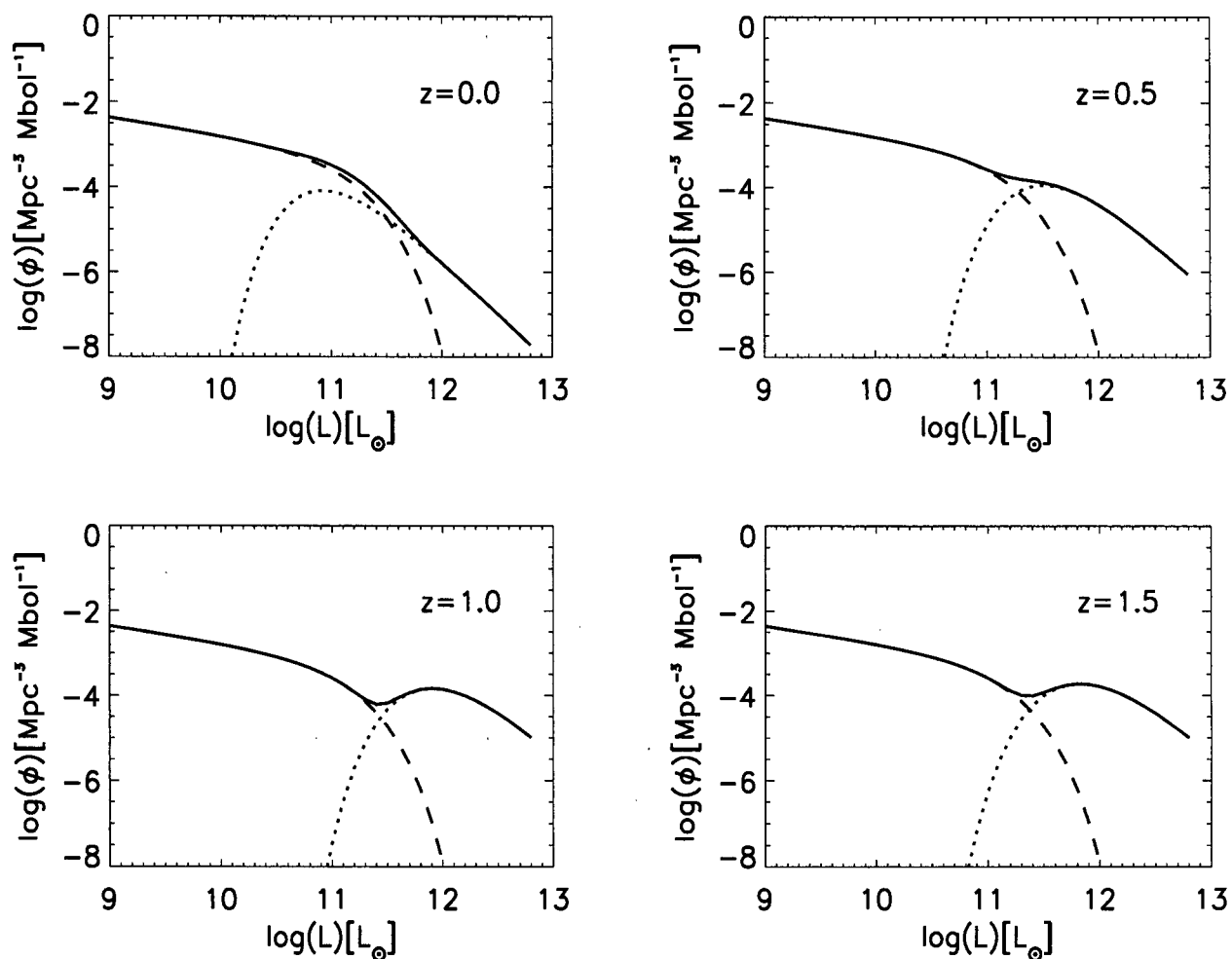


Figure 4.1: This is the luminosity function used for our models and its evolution with redshift. The dashed line is a non-evolving cold, dusty galaxy population, while the dotted line is an evolving ULIG population – the solid line is the sum of the two. See text for details.

where  $D_L$  is the conventional luminosity distance, and the subscripts “o” and “e” refer to “observed” and “emitted”, respectively (see Appendix B). This can be rewritten using the  $k$ -correction  $k = L_{\nu_e}/L_{\nu_o}$  and using  $d\nu_e/d\nu_o = (1+z)$  so that

$$S_{\nu_o} = (1+z) \frac{k L_{\nu_o}}{4\pi D_L^2}. \quad (4.5)$$

An instructive exercise is to plot the  $850\mu\text{m}$  flux as a function of redshift as an illustration of the effect of the negative  $k$ -correction at that wavelength. This is shown in Fig. 4.4 (for a typical galaxy out of our subsample of 5 higher- $z$  sources) – the  $850\mu\text{m}$  flux hardly changes beyond  $z \sim 1$ .

The number of galaxies in the range  $L$  to  $L + dL$  and  $z$  to  $z + dz$  is simply the product of the LF and volume element. Thus  $N(z)$  is the above integrated over all luminosities above a minimum  $L$  which, at the given redshift, corresponds to some observational flux limit (e.g. the FIRBACK  $3\sigma$  flux limit). Explicitly, this is as follows:

$$N(z, S > S_{\text{lim}}) = \int_{\log L(S > S_{\text{lim}}, z)} \phi(\log L, z) \frac{dV}{dz} d\log L. \quad (4.6)$$

Of particular interest to us are the number counts at  $170\mu\text{m}$ , from which population our sample is selected, and at  $850\mu\text{m}$  where we are making a connection with the “blank-sky” SCUBA sources. The results of these are presented in Fig. 4.5 and 4.6 respectively. Fig. 4.5 suggests that a bimodal redshift distribution might be expected, which is discussed in greater detail in Chapter 5.

Since redshifts are difficult to obtain for distant dusty galaxies (e.g. see Results section of this thesis), a more observationally testable distribution is  $\frac{dN}{dS}$ , which is:

$$\frac{dN}{dS} = \int_0^{z_{\text{max}}} \phi(\log L, z) \frac{d\log L}{dS} \frac{dV}{dz} dz. \quad (4.7)$$

We therefore plan to test this model (with better characterization of the high- $z$  evolution) against the observed  $N(> S)$  distribution<sup>1</sup>. At this stage, this model aims at illustrating

<sup>1</sup>The zeroth, first and second moments of the  $\frac{dN}{dS}$  distribution are, respectively, the counts  $N(> S) = \int \frac{dN}{dS} dS$ , the background intensity  $I_\nu = \int \frac{dN}{dS} S_\nu dS$ , and the background fluctuations  $\langle \delta(I_\nu)^2 \rangle = \int \frac{dN}{dS} S_\nu^2 dS$ , which are all observationally testable.

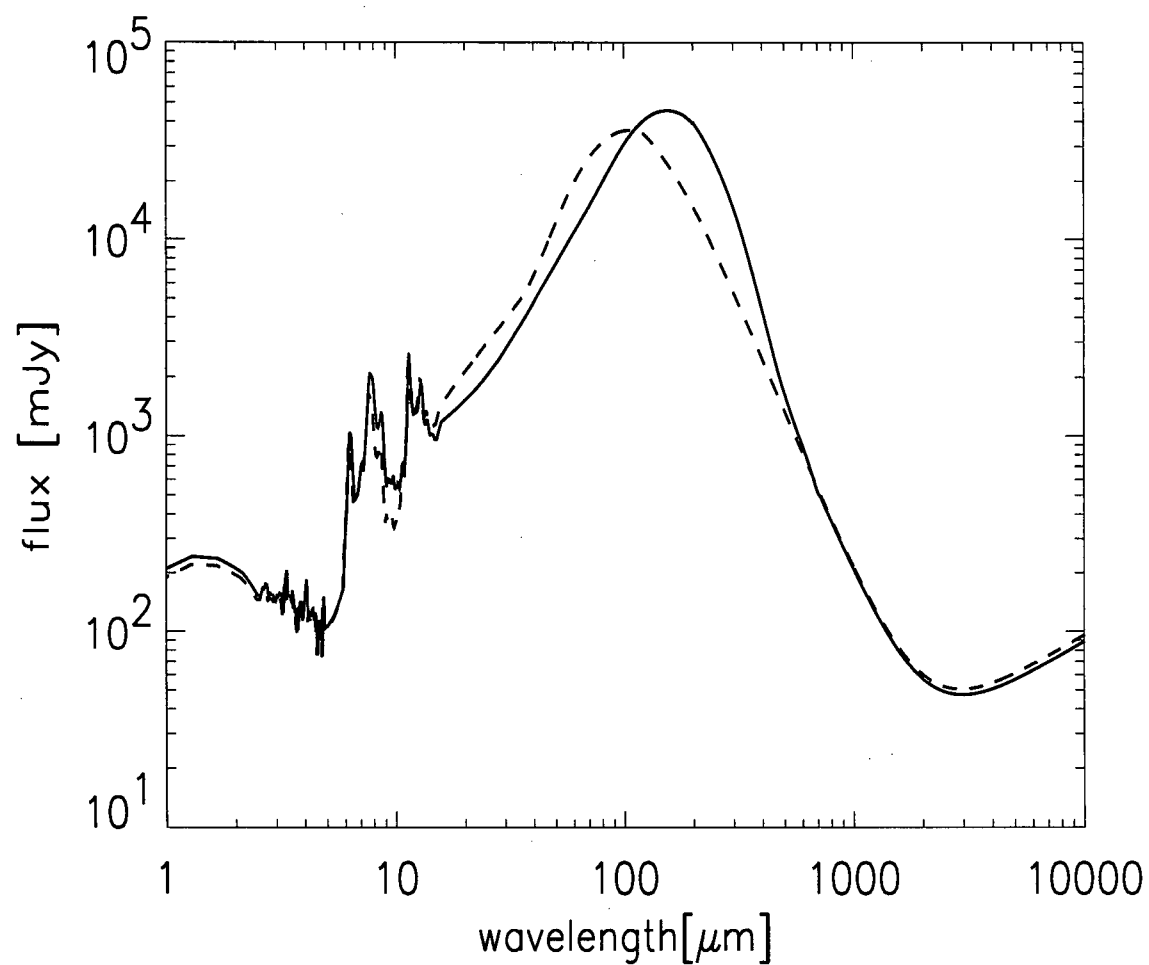


Figure 4.2: This shows the cold galaxy template (solid) compared with the starburst galaxy template (dashed) at the same luminosity ( $\sim 10^{11} L_{\odot}$ ). These were used in our model, but are shown here also as an illustration of the effect of cold dust on the SED shape. These templates are the work of Guilaine Lagache and are used in her model [45].

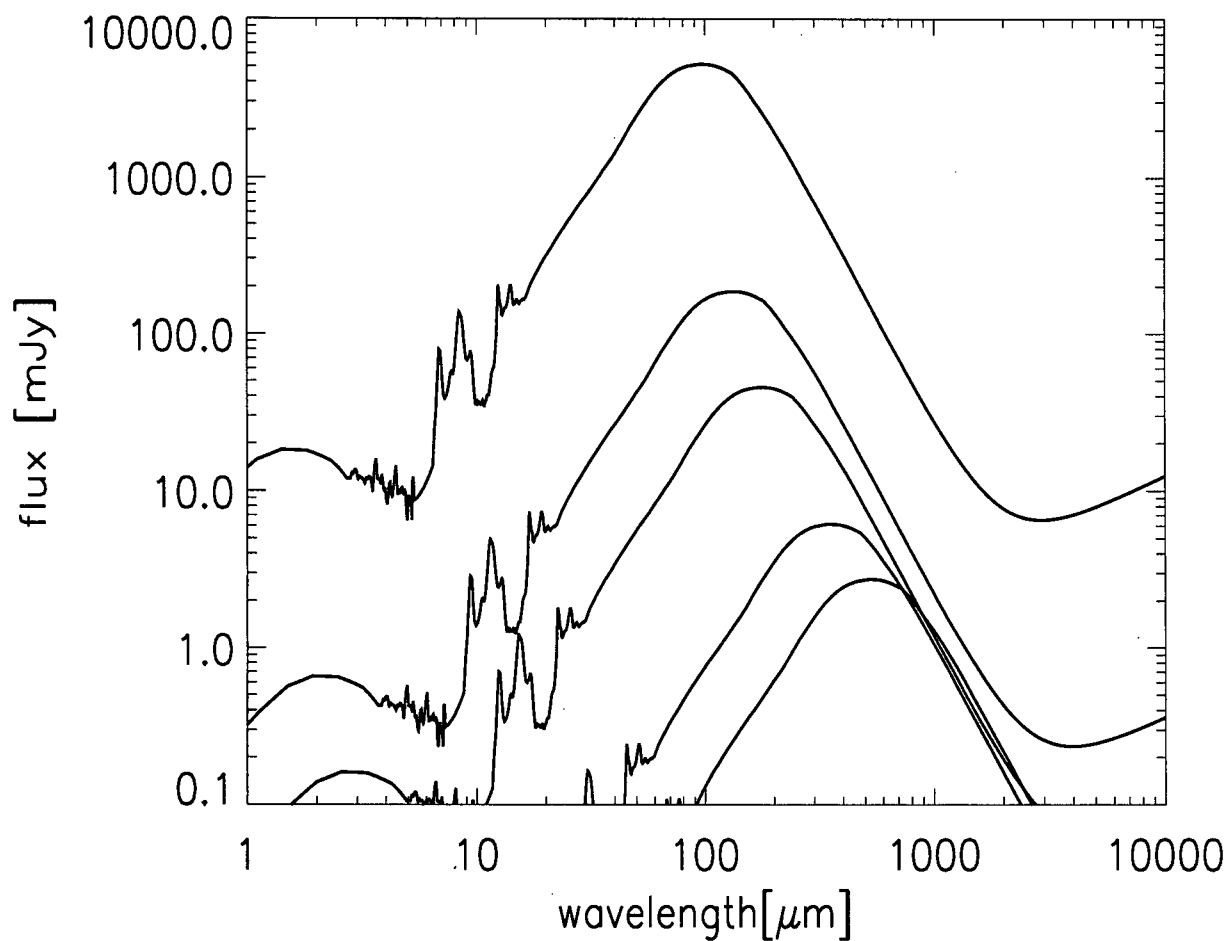


Figure 4.3: This shows the starburst galaxy template for a  $L \sim 10^{12}L_{\odot}$  galaxy. The template is evolved with redshift – from top to bottom  $z=0.1, 0.5, 1.0, 3.0$ , and  $5.0$ . Notice that this figure also illustrates the negative  $k$ -correction at  $850\,\mu\text{m}$  (see next figure).

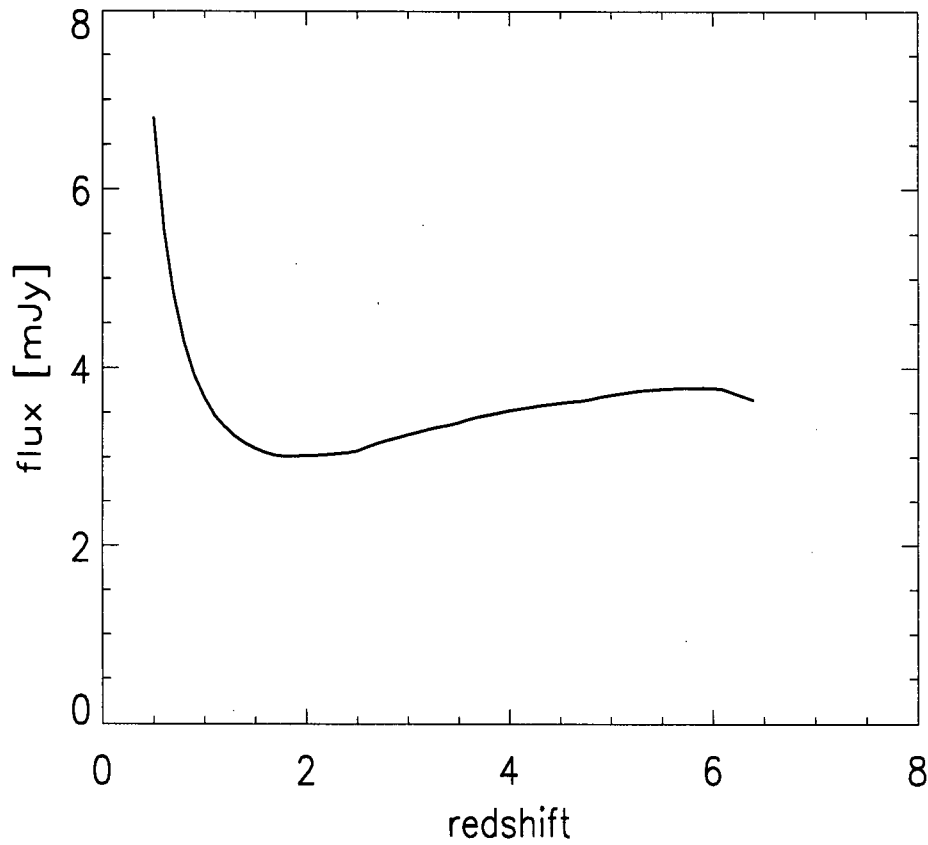


Figure 4.4: Here we plot the  $850\ \mu\text{m}$  flux vs. redshift for a  $4 \times 10^{12} L_{\odot}$  starburst (template) galaxy. This serves the double purpose of illustrating the effect of the negative  $k$ -correction at  $850\ \mu\text{m}$ , and predicting what our 5 higher- $z$  sources would look like at different redshifts. We cut the curve at  $z = 0.5$  for scaling purposes.



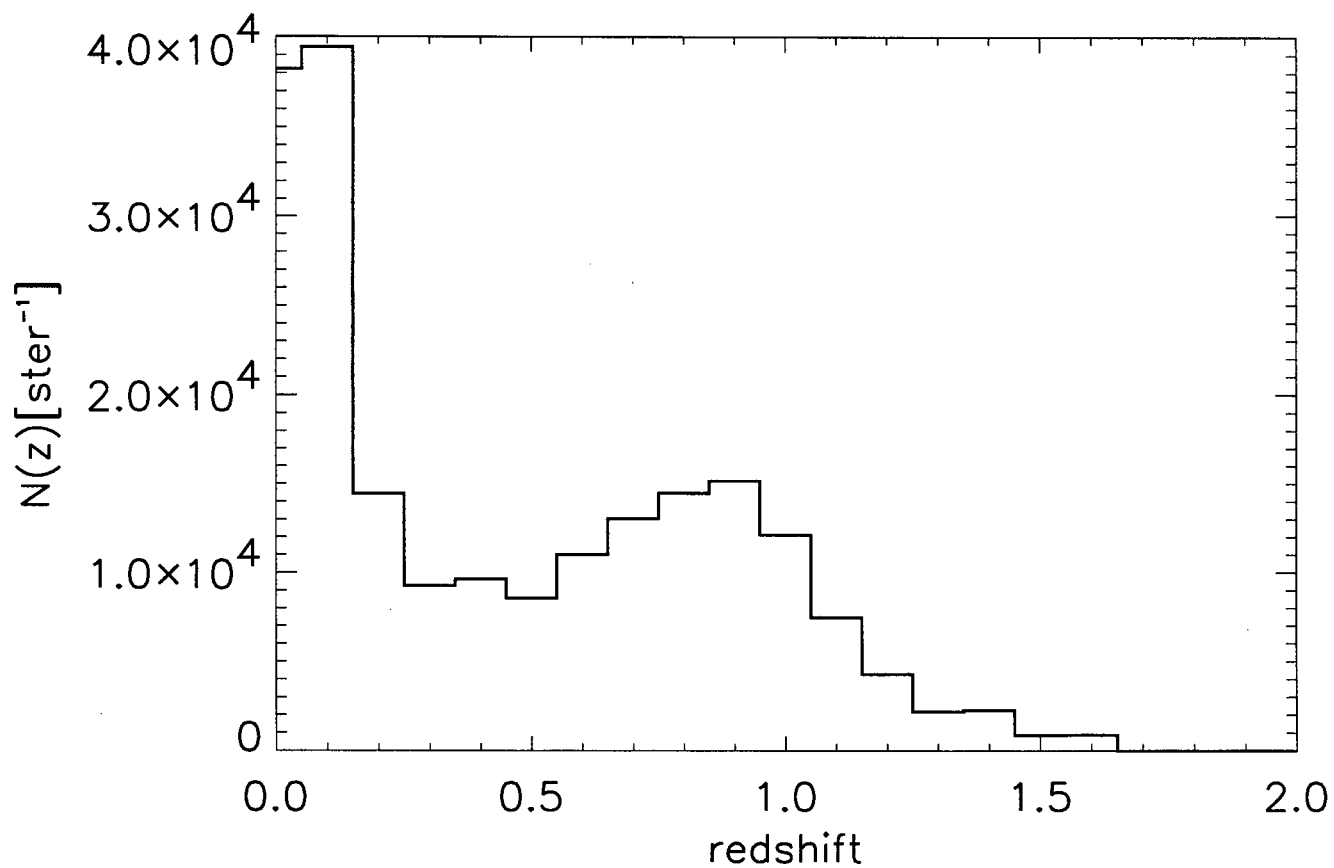


Figure 4.5: The result of our model for the predicted number counts at  $170\,\mu\text{m}$  with limiting flux of  $135\,\text{mJy}$  ( $=3\sigma$  for FIRBACK)

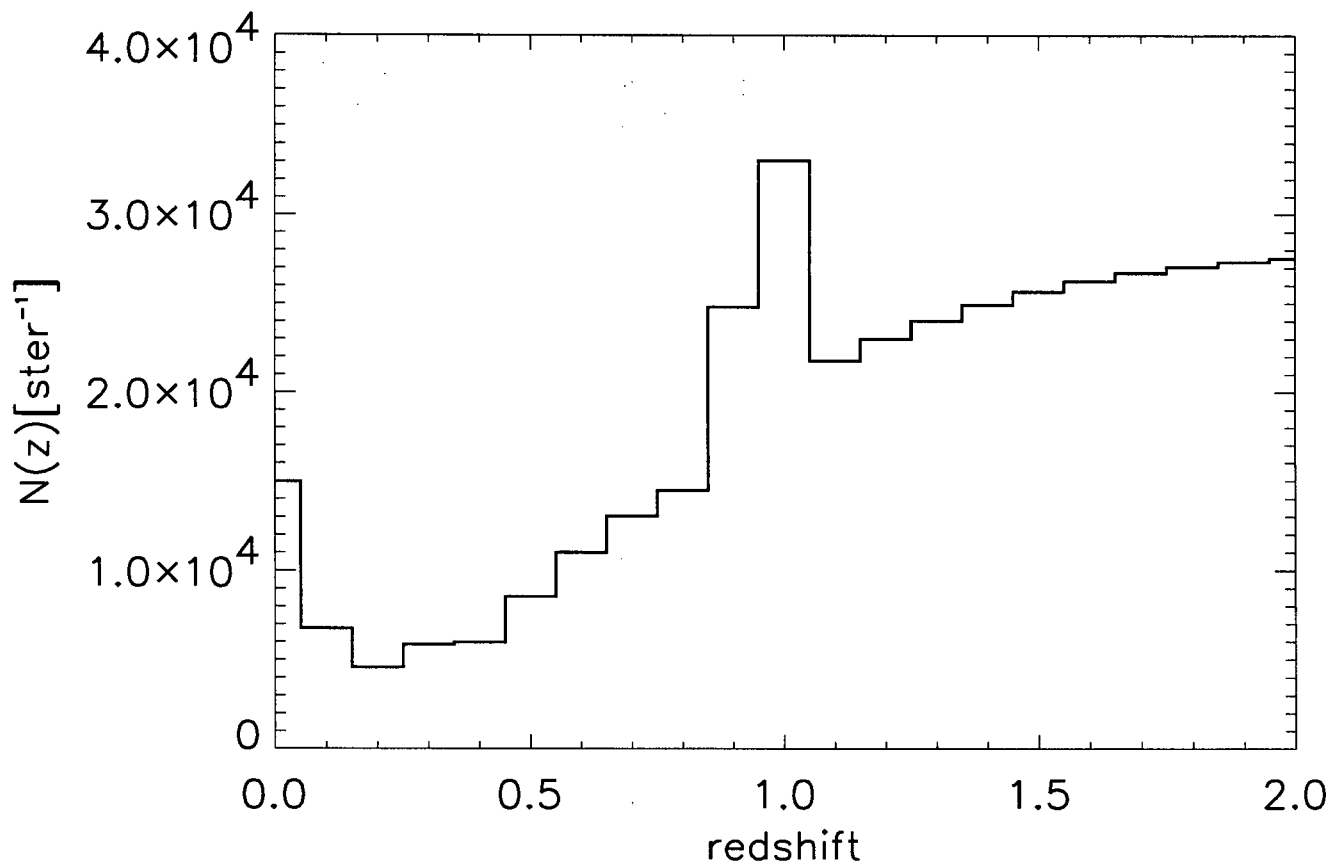


Figure 4.6: The result of our model for the predicted number counts at  $850\,\mu\text{m}$  with limiting flux of  $3.5\,\text{mJy}$  ( $=3\sigma$  for our sample)

some of the essential ingredients in phenomenological galaxy evolution modelling, as well as illustrating how a reasonable set of assumptions results in a redshift distribution which is reminiscent of what we observe for our sample. Similar models from the literature, and their results, are discussed in Chapter 5.

# CHAPTER 5

## SUMMARY & DISCUSSION

The multiwavelength photometric analysis of the sample of galaxies presented in the previous sections provides us with an insight into the brightest contributors to the CIB. This sample holds information on galaxy evolution roughly in the range  $z \sim 0 - 1$ . Here we discuss the results of this work, and place them in the context of similar or complementary observations as well as model predictions.

The first thing we looked at was the series of scatter plots in Fig. 3.3. We noticed that a group of 5 sources (N1-040, N1-048, N1-059, N1-064, N1-078) stand out from the rest in several of the plotted relations (particularly far-IR/sub-mm, and sub-mm/radio). Their position in the far-IR/sub-mm plot can be explained either by their being much colder, or at somewhat higher redshift than the rest of the sample (the  $T_d/(1+z)$  degeneracy). However, when the sub-mm slope ( $S_{450}/S_{850}$ ) alone is examined, these sources do not stand out as might be expected if their intrinsic SED shapes were substantially different from the rest of the sample. Thus, we assume an essentially constant SED shape across the sample, and arrive at a combined best-fit single grey-body (from the  $S_{170}/S_{450}$  and  $S_{450}/S_{850}$  slopes) with  $\beta \simeq 1.5$  and  $T_d/(1+z) \simeq 30$  K. See Fig. 3.5 for confidence levels. When the sub-mm/radio relation is examined, the group of 5 stands out again, with a number of redshift estimators agreeing as to their being at higher ( $\sim 0.4-1.0$ ) redshifts. These indicators have large intrinsic uncertainties ( $\Delta z \sim 0.5$ ), which, added to the large uncertainties in the spectral indices themselves, means that they do not give very reliable redshifts, although they do provide a useful qualitative way of distinguishing the higher redshift candidates. The DCE (Dunne, Clements & Eales [24]) relation seemed to provide the best-fit to the spectroscopic data, and thus is considered more reliable. The above five sources are the only ones for which this relation gives a redshift  $> 0.4$ . An exception is N2-013, but on the basis of the SED fits, we suspect this source of being a luminous

infrared galaxy at non-negligible redshift, perhaps  $\sim 0.3$ , which is consistent with the redshifts provided by the sub-mm/radio relations. On the whole, these redshift relations are based on samples of extremely luminous infrared and radio galaxies. This may not apply well to our local sample, since it is consistent with lower luminosity starforming galaxies (in particular N1-001, and N1-002 both have spectroscopic redshifts which are poorly fit by all considered relations).

A different way to look at the data is the sub-mm/near-IR relation (Fig. 3.7). Here, the segregation of the higher redshift candidates is most pronounced – more than  $2\sigma$  separate each of the above 5 sources from any of the rest of the sample (although the location of N1-032, and N1-034 is poorly understood at this point). This projection has the advantage of sampling two spectral regions with completely different emission mechanisms: thermal dust emission vs. stellar light plus dust attenuation (luminosity dependent). This means that the  $T_d/(1+z)$  degeneracy is largely broken. However, since no robust relation is known, at present, we can do little beyond obtaining a qualitative confirmation of the approximate redshift range of the sources.

From our sample, and the  $K$ - $z$  relation for radio galaxies, from Willot et al. [66], we construct a rough envelope in the  $K$ - $z$  diagram (see bottom of Fig. 3.7). It is possible that the  $850\mu\text{m}$  point could be used (as a luminosity gauge) in conjunction with the  $K$ -magnitude, leading to a redshift indicator encompassing the entire range of dusty, luminous, high-SFR galaxies. Although we attempt this here, with only 6 galaxies for which spectroscopic redshifts are available we cannot provide a robust relation. The situation will improve once our sample has more complete spectroscopic coverage. Since such a relation would suffer from a completely different set of systematic uncertainties than the radio/sub-mm photometric redshifts, the combination of both would be a good way to constrain the redshifts at the same time as distinguishing between the colder and warmer sources. This is difficult for the traditional sub-mm/radio relations alone for sources below 60 K. The potential of such an approach was already shown by Dannerbauer et al. [18] in the context of their mm-selected galaxies compared with the IRAS-selected galaxies of the SLUGS sample [23].

Finally, we used the knowledge of the general trends in our sample, inferred from the above steps, to attempt to constrain some of their individual properties. We thus fit single, optically-thin, grey-bodies to the  $170\,\mu\text{m}$ ,  $450\,\mu\text{m}$ , and  $850\,\mu\text{m}$  points. Since  $\beta$  was poorly constrained from fitting the slopes alone (see section 3.2), we investigated a number of representative values (1.3, 1.5, 1.7, and 1.9). We discovered that for the sample as a whole only  $\beta \simeq 1.5\text{--}1.7$  provides a good fit, while 1.3 is a poor fit to many of the probably local sources, and 1.9 is a poor fit to our higher- $z$  candidates. Since the fits only provide  $T/(1+z)$ , a dust temperature needs to be assumed in order to obtain a redshift. We estimate that an acceptable range is the  $[\beta, T]$  combinations  $[1.7, 30\,\text{K}] \rightarrow [1.5, 40\,\text{K}]$ . These give redshifts which are in reasonable agreement with all relations examined so far (including the DCE, and CY (Carilli & Yun [8]) redshift indicators). In Section 3.6, we use this range to estimate the luminosities, and SFRs of the 5 high- $z$  candidates, along with some sources which are possible LIGs at  $z \sim 0.3$ .

Our results, from near-IR to radio, are consistent with having a sample of mostly local galaxies, some slightly higher redshift LIGs and a handful of probable ULIGs at redshifts about  $0.4 < z < 1.0$ .

#### Merger Morphology:

We have selected a representative sample of ULIGs (possibly merger systems) at redshifts  $z \sim 0.5 - 1.0$ , which are likely to be the counterparts of faint ( $S_{850}=2\text{--}3\,\text{mJy}$ ) high- $z$  SCUBA sources (Fig. 4.4), which are usually modelled with local ULIGs as templates. By providing a longer baseline compared to local studies[64], our sample will allow for evolutionary effects in merger morphology to be investigated. This would perhaps also allow for more realistic local counterparts to the high- $z$  systems to be selected. A better understanding of mergers at various epochs has obvious implications for our understanding of galaxy formation, since mergers are crucial within the popular hierarchical structure formation picture. We discuss some of these issues below, in the context of the two spectroscopically confirmed ULIGs.

The physical size of an object is related to its angular size by  $d = D_M \Delta\theta / (1+z)$ , where  $D_M$  is the comoving radial distance defined in Appendix B, and  $\Delta\theta$  is the angular size.

Thus from our  $K$ -band images we infer for N1-064 a fairly compact size of  $\sim 3$  kpc (based on a half-light radius of  $\sim 0.4''$ ) for each of the interacting components, and a projected separation between them of  $\sim 18$  kpc. The J1 component of N1-040 (at  $z=0.45$ ) is also very compact ( $\sim 1.5$  kpc), and its separation from J2 is  $\sim 15$  kpc – assuming that J2 is interacting with it (which is not confirmed at this stage). Typical separations in local ULIGs are 1–2 kpc although some extend to  $> 10$  kpc [64], [55]. Higher redshift merger morphologies are hard to obtain as they are rarely resolved and often have no confirmed redshift. An example is a set of lens-amplified  $z \sim 2$  ULIGs which, in high-resolution near-IR imaging, show compact components at projected separations of 5–10 kpc (based on  $H_0=50$ ,  $q=0.5$  cosmology) [41]. This is quite similar to N1-064. This issue, in general, has not been addressed thoroughly enough to be able to claim that the average ULIG merger at higher- $z$  involves wider separations than locally. If true however, this has important implications as an indication of the inadequacy of using local systems as templates for high- $z$  systems of equal luminosity, since the SED shapes would differ. Pursuing such morphological studies of high- $z$  mergers has implications for our understanding of galaxy formation, especially the formation of spheroids which are believed to result directly from mergers at various epochs. For example, one possible mechanism for achieving ULIG-like luminosities at such early stages of the merger is to funnel more gas into the centre of the galaxies via bar instabilities which would be impeded by the presence of large bulges (such as are usually present in local ULIGs) [6][41]. It is clear that, as an alternative to mechanical dumping of more gas into the starforming region, the same effect can be achieved by allowing for easier propagation of photons through the ISM. This can be achieved either by different ISM (smaller dust grains, lower metallicity, ionization, etc.), or different ISRF (InterStellar Radiation Field) properties (e.g. an IMF leaning towards more massive stars). Exactly how our sample relates to merger sequences and local ULIGs will await more detailed observational follow-up.

## 5.1 Comparison with related studies

A survey similar to FIRBACK in depth (with  $3\sigma$  limit of  $S_{170}=150$  mJy) was carried out in the Lockman Hole region [43]. Optical/NIR and radio follow-up, including imaging and spectroscopy of 35 out of 45 detected sources, revealed 1 hyperluminous galaxy at  $z=1.6$ , 11 ULIGs at  $0.3 < z < 1.2$ , 12 LIRGs at  $z < 0.3$ , and the rest a mixture (in spectroscopic classification) of local starforming galaxies. This is in qualitative agreement with our results. However, we do seem to find fewer ULIGs relative to this study. It is not clear how the 35 were selected out of the 45 detections. Assuming that all their remaining detections are local sources, we still have  $\sim 10\%$  fewer higher- $z$  ULIGs candidates than they find. Our ULIG candidates were selected on the basis of their photometric properties with respect to the rest of the sample, but there are enough intermediate sources in our sample (e.g. N1-045, N1-068, N2-013) that could be at redshifts of  $\sim 0.3$  to bring the two surveys in even closer agreement. Until we have full spectroscopic coverage of our sample, we cannot confidently differentiate between redshift binning finer than  $\sim 0.5$ . However, our additional radio selection would exclude a hyperluminous galaxy such as found in this Lockman Hole survey.

A much shallower (detection limit  $\sim 600$  mJy) ISO  $170\mu\text{m}$  survey was the Serendipity Survey [63]. Their sample was found to be primarily composed of local,  $L \sim 10^{10}L_{\odot}$  spirals which were well fit by cold ( $\sim 20$  K) dust temperatures. Some fraction of our local sample are likely to overlap with this sample. A much better overlap can be achieved by deeper mid-IR surveys such as the  $12\mu\text{m}$  selected sources of Clements et al. [16]. Optical follow-up of this sample was found to be composed of mostly  $z \sim 0$  sources of low  $L \sim 10^{10}L_{\odot}$  with a higher- $z$  tail extending to  $z \sim 0.5$ . Notice that a  $12\mu\text{m}$  survey is insensitive to higher redshift objects due to the unfavourable  $k$ -correction. We are clearly observing the similar type of population with our low- $z$  sources.

Our higher-luminosity sources (LIRGs, and ULIGs) on the other hand are likely to be more similar to IRAS-bright galaxies. The SCUBA Local Universe Galaxy Survey (SLUGS) consists of 104 galaxies selected from the IRAS Bright Galaxy Catalogue



(BGC), and followed-up with SCUBA [23]. The single grey-body fits yield  $\beta = 1.3 \pm 0.2$  and  $T_d = 38 \pm 3$  K. However, including some  $450 \mu\text{m}$  data they fit two grey-bodies and find that although some galaxies continue to be well described by  $\sim 40$  K dust temperatures, some require an additional much lower  $T \sim 20$  K temperature component (and  $\beta = 2$ ) much more consistent with regular local starforming galaxies (e.g. the Milky Way). Klaas et al. [44] present a set of far-IR to mm SEDs for 41 local ULIG galaxies from which they infer a 3-component dust model. The warm one ( $T > 50$  K) is only important at mid-IR wavelengths, the far-IR/sub-mm being represented by a combination of a cool ( $30 < T < 50$  K) component, and a cold ( $T < 30$  K) component. In addition they infer  $\beta = 2$ , and low opacity. From their SEDs, it is clear that although the cold component is the best description for the sub-mm points, it is a negligible contribution around the peak. On the other hand, their cool component fits the peak well while somewhat underestimating the sub-mm fluxes (however a lower  $\beta$  than their value of 2 would account for that). Thus, since we can only fit single grey-bodies to the SEDs, over  $170 \mu\text{m} \rightarrow 850 \mu\text{m}$ , and a poor fit is provided for our higher-luminosity sources by  $\beta=1.9$ , it seems as though the best fit equivalent single grey-body corresponds most closely to the cool temperature component of Klaas et al.[44]. Whether this is simply a phenomenological fit parameter, or represents a true physical temperature for the dust will require further study.

## 5.2 Bimodality

Some of the scatter plots discussed above suggest a bimodality in our sample. Whether our particular observational selection effects result in bimodality in redshift, or just a higher- $z$  tail is an important point for distinguishing various galaxy evolution models (discussed in Section 5.3). Due to the small size of our high- $z$  candidates sample, it is difficult to test their distribution properties. A test which we can perform involves comparing the  $\chi^2$  resulting from fitting a single line ( $y = mx$ ), against that for fitting two lines, both with zero  $y$ -intercept, to the  $S_{170}$  vs.  $S_{850}$  projection. We chose this

particular projection as here the bimodality is implied, but is not as clean as in the sub-mm/near-IR relation. We show the result in Fig. 5.1. We performed this test with the 1D  $\chi^2$  simply assuming constant error for each source (since they are fairly uniformly distributed). The single line fit results in  $\chi^2$  of 108, while the two-line fit results in  $\chi^2$  of 37. By comparing the  $\chi^2$ s we conclude that the two line fit provides a much better fit to our data (where  $N=31$ ) than the single line fit.

This supports the idea that a handful of our sources lie at  $z \sim 0.5$ , while most of the sample are at  $z \sim 0$ .

### 5.3 Comparison with evolutionary models

The sources studied here are a representative sample of the brightest  $\sim 10\%$  of the CIB. They thus provide a test of the various evolutionary models abounding in the literature. Models which are consistent with both the CIB intensities observed, and the number counts obtained by various surveys, imply that the majority ( $\sim 80\%$ ) of the CIB near its peak ( $\sim 200 \mu\text{m}$ ) will be resolved by sources  $0 < z < 1.5$ . The same redshift range sources contribute only  $\sim 30\%$  of the  $850 \mu\text{m}$  background [28, 14]. The same models result in a peak of the SFR density at  $z \sim 1.0$ , which is essentially flat from there until  $z \sim 4$ . In general,  $> 70\%$  of the star formation takes place in galaxies with  $L_{\text{FIR}} > 10^{11} L_{\odot}$  [14]. From the redshifts we infer for our sample, it seems to span a crucial epoch over which the strongest evolution of the SFR density takes place. In general there is no way to fit the FIRBACK counts without strong far-IR evolution over at least this redshift range. With the starburst template we use in Chapter 4, we see that sources less luminous than about  $10^{12} L_{\odot}$  fall below the FIRBACK detectability beyond redshift  $\sim 0.4$ . Fig. 5.2 shows the relative contributions to the CIB of normal galaxies, LIRGs, and ULIGs as a function of redshift from the models of Chary & Elbaz [14]. It makes it clear why the FIRBACK survey resolved only a small fraction of the CIB. Since the FIRBACK selection excludes normal galaxies beyond  $z \sim 0.1$  and LIRGs beyond  $z \sim 0.3$ , but allows for higher-luminosity sources up to  $z \sim 1.0$ , our mix of normal, starforming galaxies, a

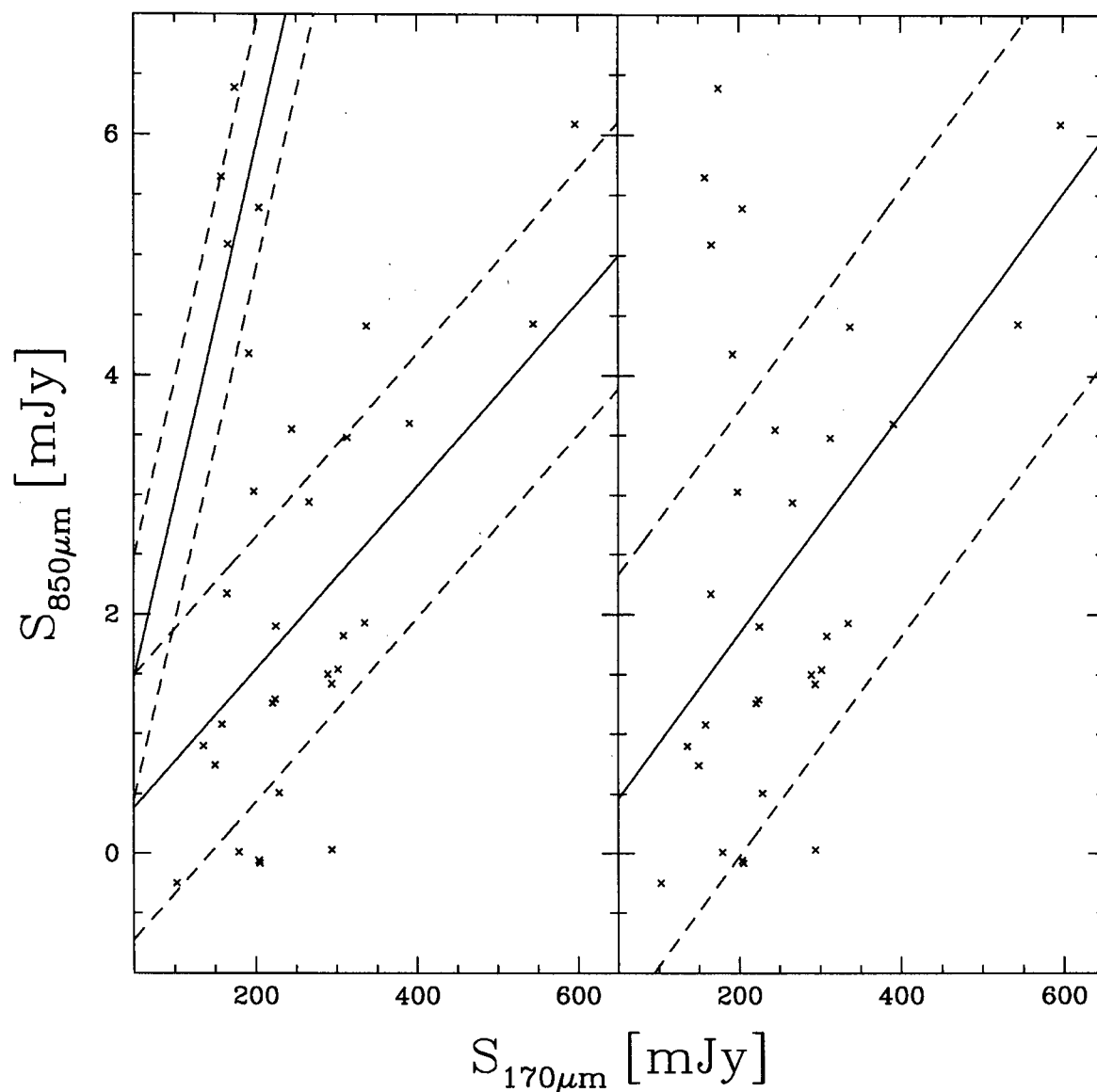


Figure 5.1: Here we test the hypothesis of our sample being bimodal by comparing the  $\chi^2$  of a single-line fit for the entire sample (right panel) to a two-line fit to each sub-sample (left panel). The dashed lines are  $\pm 1\sigma$  where  $\sigma$  is the rms scatter in the  $y$ -direction. Notice that, apart from N1-048, even with the single-line fit to the entire sample, our high- $z$  candidates are  $> 2\sigma$  away from the best-fit line.

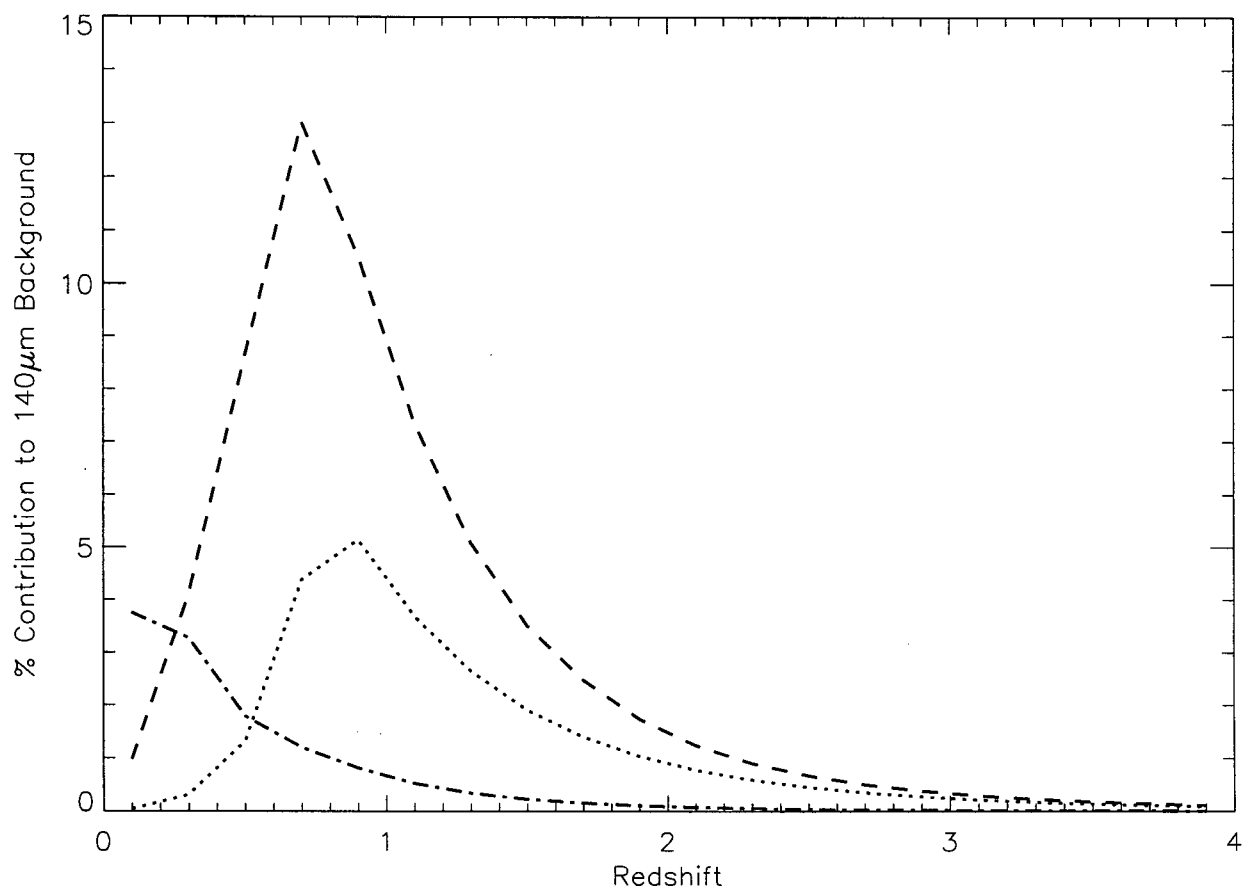


Figure 5.2: One example of redshift contributions to the CIB. Here the dot-dashed line represents normal, starforming galaxies, the dotted line is the ULIGs, and the dashed line is the LIRGs (reproduced from Chary & Elbaz 2001 [14]).

few possible LIRGs, and a handful of most likely higher- $z$  ULIGs is in good qualitative agreement with this model. The bimodality, which this hints at for our selection (and which we appear to observe), is more directly shown by other models [45, 10, 22, 65, 33]. The easiest way to achieve it is to build-in the discontinuity phenomenologically by decomposing the luminosity function into a component of normal, quiescent galaxies, and a much more luminous component of ULIGs (or AGN), and have the luminous component evolve more strongly than the quiescent one so that it dominates the luminosity function by  $z \sim 1$  [22, 65, 33]. This approach was exploited in the context of the FIRBACK

sources by Lagache et al. [45], confirming our results in that a double-peaked redshift distribution is predicted. Other models with the same feature amount to the same basic physics (rapid evolution of the far-IR bright population), although some may be more directly related to galaxy evolution models. One example is that of Chapman et al. [10]. It combines the colour (i.e. temperature) distribution of local galaxies with a strong luminosity evolution (such as in [67]), to produce a bi-variate distribution for the FIRBACK population (including cold luminous sources), as observed in our sample. Discriminating in detail between such models, including issues such as separating density evolution from luminosity evolution, will require the full redshift distribution.

The FIRBACK selection allows us to investigate the range  $0 < z < 1$ . On the other hand  $z \sim 1$  is the lower limit of sub-mm/mm selected surveys (e.g. [61, 18]). Thus samples such as ours should act as a bridge between the local Universe and the higher redshifts population detected in long-wavelength surveys. We show this explicitly in Fig. 3.7 where we overlay a number of SCUBA-selected sources, and show that they occupy essentially the same sub-mm/near-IR space as our high- $z$  candidates. Hence it should be possible, by investigating our higher- $z$  candidates in detail, to determine the properties of a subset of SCUBA-type galaxies, in a way which is next to impossible for the typical  $z \sim 3$  sources.

## 5.4 Future Direction

In conclusion, even though the majority of the sources are not individually detected: 1) the sample as a whole is strongly detected ( $\sim 10\sigma$  for both bands); and 2) there is a wealth of statistical information to be extracted about the nature of the sources comprising the sample. This highlights the importance of carefully obtaining a uniform sample, rather than an inhomogeneous collection of data. Such targetted photometry observations reveal some of the same fundamental trends as a more costly (observationally) full-imaging survey.

We have learned that the brightest 10% of the CIB is composed of two different types of

galaxy: about 1/6 is the low redshift tail of a rapidly evolving ULIG population; and the other 5/6 are mainly nearby quiescently star-forming galaxies like the Milky Way. Further progress on constraining models in detail will come from spectroscopic and morphological studies of the entire sample. Understanding what makes up the other  $\sim 90\%$  of the CIB will await future far-IR missions with smaller beamsizes, such as BLAST and Herschel, as well as high sensitivity mid-IR facilities such as SIRTf.

## BIBLIOGRAPHY

- [1] Archibald E., Wagg J.W., Jenness T., 2000, JAC, JCMT, <http://www.jach.hawaii.edu/JACdocs/JCMT/SCD/SN/002.2/>
- [2] Barger A.J., Cowie L.L., Mushotzky R., et al. 2001, AJ, 121, 662
- [3] Barger A.J., Cowie L.L., Sanders D.B., 1999, AJ, 518, L5
- [4] Blain A.W., Smail I., Ivison R.J., Kneib J.-P., Frayer D.T., 2002, astro-ph/0202228
- [5] Blain A.W., Kneib J.-P., Ivison R.J., Smail I., 1999, ApJ, 512, L87
- [6] Binney J., Merrifield M., 1998, "Galactic Astronomy", Princeton University Press
- [7] Bridger A., Wright G.S., Economou F., Tan M., Currie M., Pickup D., Adamson A., Rees N., Purves M., Kackley R., 2000, SPIE, 2009, 227
- [8] Carilli C.L., Yun M.S., 1999, ApJ, 530, 618
- [9] Carroll S.M., Press W.H., Turner E.L., 1992, ARAA, 30, 499
- [10] Chapman S.C., Helou G., Lewis G., Dale D., 2002, ApJ, to be submitted
- [11] Chapman S.C., Smail I., et al., 2001, submitted to ApJ
- [12] Charbonneau P., 1999, ApJ, 101, 309
- [13] Charlot et al., 2002, astro-ph/0111289
- [14] Chary R., Elbaz D., 2001, ApJ, 556, 562
- [15] Ciliegi P., et al., 1999, MNRAS, 302, 222

- [16] Clements D.L., Desert F-X, Fracescini A., 2001, accepted by MNRAS, astro-ph/0103242
- [17] Cowie L.L., Barger A.J., Kneib J.-P., 2002, AJ, in press
- [18] Dannerbauer H., Lehnert M.D., Lutz D. et al., 2002, astro-ph/0201104
- [19] Davis R., Burston A., Ward M., 2000, astro-ph/0012221
- [20] Devriendt J.E.G., Guiderdoni B., Sadat R., 1999, A&A, 350, 381
- [21] Dole H., Gispert R., Lagache G., et al., 2001, A&A, 372, 364
- [22] Dole H., et al., 1999, "ISO surveys a dusty Universe", Eds. D. Lemke, M. Stickel, K. Wilke, p.54
- [23] Dunne L., Eales S.A., 2001, MNRAS, 327, 697D
- [24] Dunne L., Clements D.L., Eales S.A., 2000, MNRAS, 319, 813D
- [25] Dunne L., 2000, PhD thesis, University of Wales
- [26] Dwek E., Arendt R., Hauser M., et al., 1998, ApJ, 508, 106
- [27] Elbaz D., Cesarsky C.J., Fadda D., et al., 1999, A&A Letters, 351, L37
- [28] Elbaz D., Cesarsky C.J., Chanial P., et al., 2002, astro-ph/0201328
- [29] Fabian A.C., Smail I., Iwasawa K., Allen S.W., Blain A.W., Crawford C.S., Ettori S., Ivison R.J., et al., 2000, MNRAS, 315L, 8F
- [30] Fadda D., Flores H., Hasinger G., Franceschini A., Altieri B., Cesarsky C.J., Elbaz D., Ferrando Ph., 2002, A&A, 383, 838F
- [31] Fixsen D.L., Dwek E., Mather J.C., Bennett C.L., Shafer R.A., 1998, ApJ, 508, 123
- [32] Finkbeiner D.P., Davis M., Schlegel D.J., 2000, ApJ, 524, 867



- [33] Franceschini A., Aussel H., Cesarsky C.J., et al., 2001, astro-ph/0108292
- [34] Gispert R., Lagache G., Puget J.-L., 2000, A&A, 360, 1
- [35] Hauser M.G., Arendt R.G., Kelsall T., et al., 1998, ApJ, 508, 25
- [36] Holland W., et al., 1999, MNRAS, 303, 659
- [37] Hornscheimer A.E., Brandt W.N., Garmire G.P., Schneider D.P., Barger A.J., Broos P.S., Cowie L.L., Townsley L.K., et al., 2000, HEAD, 32, 2613H
- [38] Hughes, Dunlop, & Rowlings, 1997, MNRAS, 289, 766H
- [39] Imanishi M., Dudley C.C., Maloney P.R., 2001, ApJ, 558, L93-L96
- [40] Ivison R.J., Greve T.R., Smail I., Dunlop J.S., Roche N.D., et al., 2002, MNRAS, astro-ph/0206432
- [41] Ivison R.J., Smail I., Barger A.J., Kneib J.-P., Blain A.W., Owen F.N., Kerr T.H., and Cowie L.L., 2000, MNRAS, 315, 209
- [42] Jenness T., Lightfoot J.F., 1998, in ASP Conf. Ser. 145, 216
- [43] Kakazu Y., Sanders D.B., Joseph R.D., Cowie L.L., Murayama T., et al., 2002, astro-ph/0201326
- [44] Klaas U., Haas M., Muller S.A.H., et al., 2001, A&A, submitted
- [45] Lagache G., Dole H., Puget J.-L., 2002, MNRAS, in press, astro-ph/0209115
- [46] Lagache G., Abergel A., Boulanger F., et al., 1999, A&A, 344, 322
- [47] Lagache G., Haffner L.M., Reynolds R.J., Tufte S.L., 2000, A&A, 354, L247
- [48] Lilly S., Eales S.A., Gear W.K., Webb T., et al., 1999, "The formation of galactic bulges", Eds. C.M. Carollo, H.C. Ferguson, R.F.G. Wyse, p.26
- [49] Longair M.S., 1984, "Theoretical concepts in physics", Cambridge University Press

- [50] Magliocchetti M., Maddox S.J., Wall J.V., Ben C.R., Cotter G., 2000, MNRAS, 318, 1047M
- [51] Meusinger H., Stecklum B., Theis C., Brunzendorf J., 2001, A&A, astro-ph/0111521
- [52] Particle Physics Booklet, 2002, Particle Data Group, Springer
- [53] Puget J-L., Abergel A., Bernard J.P., et al., 1996, A&A, 308, L5
- [54] Puget J-L., Lagache G., Clements D., et al., 1999, A&A, 345, 29
- [55] Saunders D.B., Mirabel I.F., 1996, ARA&A, 34, 749
- [56] Schaerer D., 1999, "Building galaxies", Eds. F. Hammer, T.X. Thuan, V. Cayette, B. Guiderdoni, J.T.T. Van., p.389
- [57] Scott D., Lagache G., Borys C., et al., 2000, A&A, 357, L5
- [58] Scott D., and the BLAST team, 2001, 'The Promise of FIRST', ESA SP-460, eds. G.L. Pilbratt et al
- [59] Scott S.E., Fox M.J., Dunlop J.S., et al., 2002, MNRAS, in press, astro-ph/017446
- [60] Slinglend K., Batuski D., Miller C., Haase S., Micaud K., 1998, ApJS, 115, 1S
- [61] Smail I., Ivison R.J., et al., 2001, astro-ph/0112100
- [62] Soifer B.T., Sanders D.B., Madore B.F., Neugebauer G., et al., 1987, ApJ, 320, 238
- [63] Stickel M., Lemke D., Klaas U., et al., 2000, A&A, 359:865
- [64] Veilleux S., Kim D.-C., Sanders D.B., 2002, astro-ph/0207401
- [65] Wang Y., Biermann P.L., 2000, A&A, 356, 808W
- [66] Willott C.J., Rowlings S., Jarvis M.J., Blundell K.M., 2002, MNRAS, astro-ph/0209439

[67] Xu C., 2000, ApJ, 541, 134X

[68] Yun M.S., Reddy N.A., Condon J.J., 2001, ApJ, 554, 803

# APPENDIX A

## PHOTOMETRY WITH SCUBA

Here we expand the discussion on reducing SCUBA photometry data, and give some of the details of the process.

In the following we demonstrate the process using the example of a single observation (taken on March 17, 2001 of N1-078, which is a detection). Fig. A.1 shows an example of the first stage of our code where the mean and variance of each bolometer are calculated by the following:

$$\mu = \frac{1}{N_J} \sum_{j=1}^{N_J} x_j, \quad \sigma = \frac{1}{\sqrt{N_J}} \sqrt{\left( \frac{1}{N_J - 1} \sum_{j=1}^{N_J} x_j^2 - \mu^2 \right)}, \quad N_J = \text{no. of jiggles} \quad (\text{A.1})$$

The noisier bolometers found using this procedure are excluded from the next stage in which the sky signature is removed. We also remove all jiggles which are  $> 5\sigma_{\text{array}}$ , where  $\sigma_{\text{array}}$  is the average  $\sigma$  for the array. This removes the very largest spikes (caused by cosmic rays or other artefacts). After these two cuts, we calculate a weighted mean for the sky (shown in Fig. A.2).

Then we perform a further despiking step by removing all jiggles  $3\sigma$  ( $\sigma$  now is for each sky-subtracted bolometer) away from the mean of the bolometer. Notice that with this cut-off, only the 405th jiggle in the plot at the bottom of Fig. A.2 was cut so this step removes only a very small fraction of the data.

The overall mean and variance can be estimated using the weighted values of the quantities estimates in bins containing some number of jiggles. We notice that there appears to be little advantage in using smaller bins in order to obtain the mean and error. We therefore estimate them using the entire observation rather than estimating the mean and error per integration (9 points) and coadding (SURF bins each integration, however does not use the obtained variances to weight each integration when coadding). We use

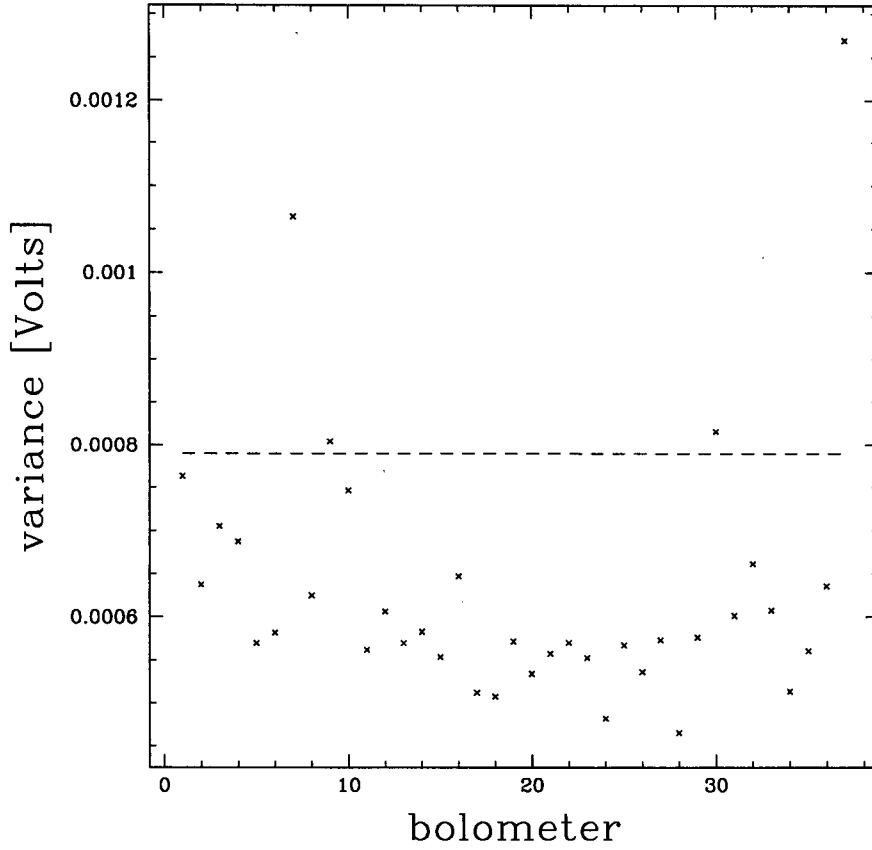


Figure A.1: This is an example of the raw bolometer variances which are used to select the bad bolometers. Here, any bolometer above the dashed line ( $=1.25\sigma_{\text{array}}$ ) is excluded from the sky calculation. Note that since, the sky level is later estimated as a weighted mean, the effect of the outliers is reduced.

the following:

$$\mu = \frac{1}{N_{\text{tot}}} \sum_{j=1}^{N_{\text{tot}}} x_j, \quad \sigma = \frac{1}{\sqrt{N_{\text{tot}}}} \sqrt{\left( \frac{1}{N_{\text{tot}} - 1} \sum_{j=1}^{N_{\text{tot}}} (x_j - \mu)^2 \right)} \quad (\text{A.2})$$

The above is the final answer when the entire observation is used, and in the case of binning the above for each bin are coadded in quadrature. Note that this has the further advantage of smoothing over some residual sky (such as smaller time scale gradients). In general, we did not proceed further with the refinement of the sky removal procedure since for the purposes of this project it is sufficient to remove features in the timestream that are larger than the scatter so the residual signal in Fig. A.2 is sufficiently clean.

Folding-In the Off-bolos: A non-standard aspect of the way our photometry data is taken and analyzed is that the chopping is done in array coordinates so that it lands on a specific off-centre bolometer. This allows for the negative beams to be folded-in increasing the signal-to-noise per observation compared to standard photometry where essentially the signal from half the observing time is lost. The folding is done as follows:

$$\mu_{\text{tot}} = \frac{\sum_{i=1}^3 \frac{w_i x_i}{\sigma_i^2}}{\sum_{i=1}^3 \frac{w_i^2}{\sigma_i^2}} \quad \text{and} \quad \sigma_{\text{tot}} = \frac{1}{\sqrt{\sum_{i=1}^3 \frac{w_i^2}{\sigma_i^2}}} \quad (\text{A.3})$$

We define  $w=1$  for the central bolometer and scale the other two accordingly. Since the source spends only half as much time in any of the off-centre positions as in the central one,  $w_{\text{off}}=-0.5$  (can also see this in that both quantities scale as  $N^{-1}$  from eq-n A.2). Note that this differs from the standard weighted mean since we are not coadding independent measurements of the same quantity – the negative beam is  $x_{\text{off}} = -0.5x_{\text{on}}$ . Due to the array assymetry, forcing one negative beam to align with an off-centre bolometer means the other one will be slightly misaligned. Assuming a Gaussian beam shape we thus have  $w_{\text{off}} = -0.5 \exp(-\frac{1}{2}(\frac{\Delta x}{2.34 \times \text{FWHM}})^2)$  where  $\Delta x$  means the distance between the beam and the bolometer centre in arcseconds. We can see that folding-in the off-beams improves the rms by roughly a factor of (setting  $\sigma$ 's as equal for simplicity)  $\frac{1}{\sqrt{0.5^2 + 1 + 0.5^2}} = \sqrt{2/3}$ , or  $\sim 20\%$  taking into account the Gaussian attenuation of the second off-beam.

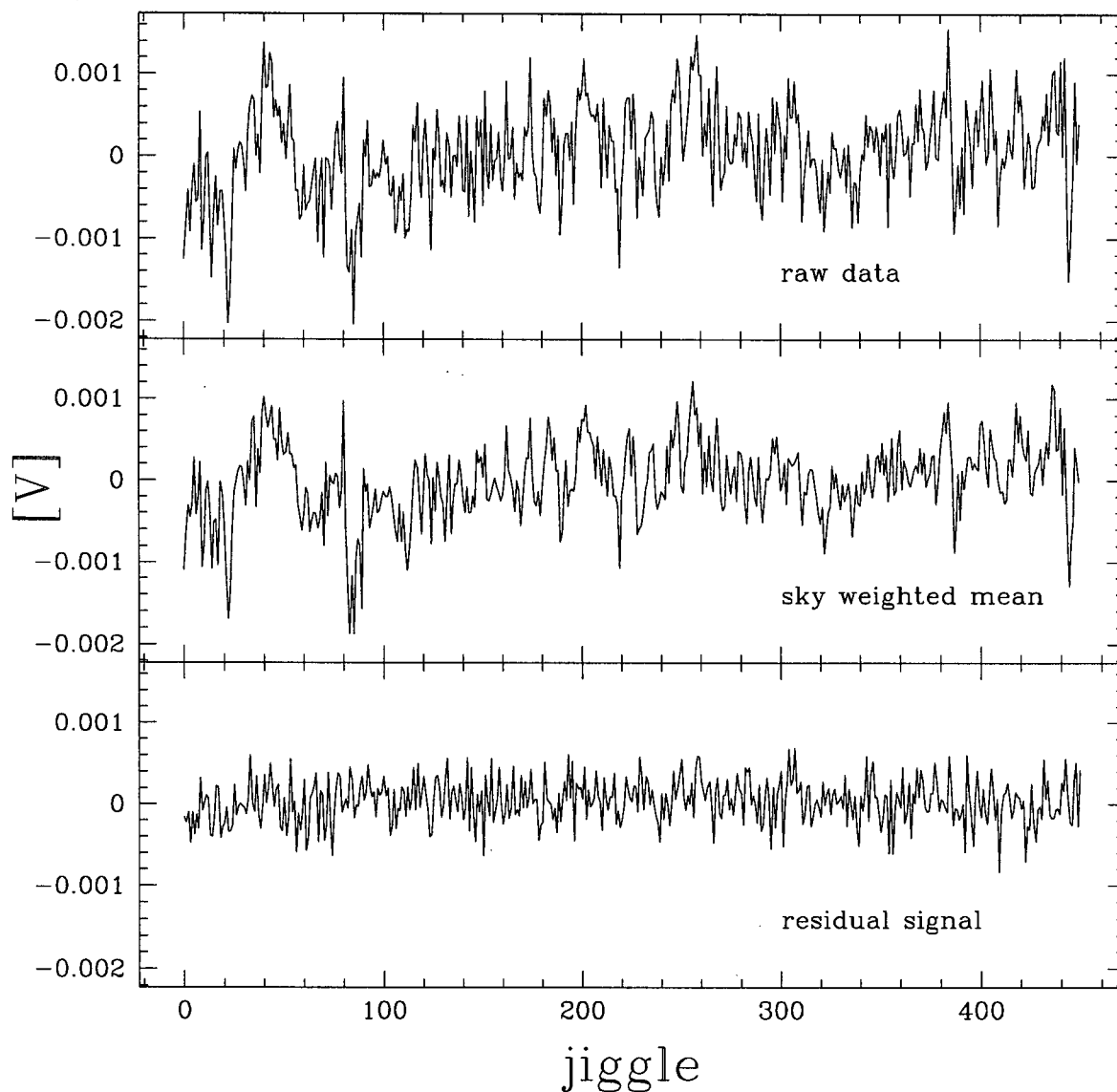


Figure A.2: The upper panel shows the extinction-corrected timestream of the central bolometer. The middle panel is the weighted mean of all the bolometers (excluding those containing signal or excessive variance). The lower panel is the residual after subtracting the middle from the top. Notice that the vertical scales are the same in each case.

# APPENDIX B

## COSMOLOGY

Here are presented some basic cosmological relations which serve as a basis for the models presented in Chapter 4. This appendix draws from several sources (where the material is covered in more depth)[49, 9].

The expansion of the Universe is Hubble's law:

$$\frac{dx}{dt} = H(t) \times x \quad (\text{B.1})$$

where  $H(t)$  is the Hubble constant ( $H_0$  today). However due to the effects of components such as matter, cosmological constant, and possibly curvature, the dynamics and geometry of the Universe can be complicated. Hence the scale factor  $R$  is introduced which relates the proper distance  $x$ , to a comoving radial distance  $r$ , such that  $x(t) = R(t)r$ , and  $R(t_0) = 1$ ). In curved space the radius of curvature is just  $R_c(t) = \mathcal{R}R(t)$ , with  $\mathcal{R}$  constant. The Friedmann-Robertson Walker (FRW) metric (general metric for isotropic curved spacetime) can be written<sup>1</sup> as:

$$ds^2 = dt^2 - \frac{R^2(t)}{c^2} (dr^2 + \mathcal{R}^2 \sin^2(r/\mathcal{R})(d\theta^2 + \sin^2\theta d\phi^2)). \quad (\text{B.2})$$

$r$  is given by  $r = \int_{t_1}^{t_2} \frac{cdt}{R(t)}$ . By the definition of  $r$  as comoving distance we have  $\frac{\Delta t_o}{R(t_o)} = \frac{\Delta t_e}{R(t_e)}$  (i.e. time dilation). The scale factor is a function of the specific model adopted, determined through the Friedmann equation (describing the dynamics of the Universe in the hot big bang model) which is as follows:

$$H^2 \equiv \left( \frac{\dot{R}}{R} \right)^2 = \frac{8\pi G}{3} \rho_M + \frac{\Lambda}{3} - \frac{kc^2}{R^2} \quad (\text{B.3})$$

where  $\Lambda$  is the cosmological constant, and  $k$  is the curvature parameter.

---

<sup>1</sup>For the closed case we have  $\sin$  in the radial line element, while for the open case  $\sin \rightarrow \sinh$ , and for the flat case it is linear (i.e.  $\sin(x) \rightarrow x$ )



At the present epoch, we can rewrite the above as:

$$1 = \Omega_M + \Omega_\Lambda + \Omega_k, \quad (\text{B.4})$$

where  $\Omega_\Lambda = \Lambda/3H_0^2$ ,  $\Omega_M = \frac{8\pi G}{3H_0^2}\rho_M$ , and  $\Omega_k = \frac{kc^2}{R^2H_0^2}$ . The currently favoured model has  $\Omega_M=0.3$ ,  $\Omega_\Lambda=0.7$  and  $\Omega_k=0$  [52].

To extract from the above some observables we step back a bit to recall that redshift is defined as

$$z \equiv \frac{\lambda_o - \lambda_e}{\lambda_e} = \frac{\nu_e}{\nu_o} - 1. \quad (\text{B.5})$$

From the time dilation expression above, the fact that  $R(t_o) = 1$  by definition, and  $\Delta t = \nu^{-1}$  we have

$$1 + z = \frac{1}{R(t)}. \quad (\text{B.6})$$

The basic parameter we need to estimate is the distance within the particular cosmological model. The definition of luminosity distance is

$$D_L = \left( \frac{L}{4\pi F} \right)^{1/2}, \quad (\text{B.7})$$

where  $L$  and  $F$  refer to bolometric quantities. On the other hand:

$$\begin{aligned} F &= L \times (\text{surface area})^{-1} \times (\text{frequency shift})^{-1} \times (\text{time dilation})^{-1} \\ &= \frac{L}{4\pi R^2(t)r^2(1+z)^2}. \end{aligned} \quad (\text{B.8})$$

This leads to the definition  $D_L = R(t)r(1+z)$  – which is very crudely  $\sim c(1+z)/H_0$ . To do this more precisely must go back to the integral for  $r$  and re-express it in terms of  $z$  as  $\frac{dr}{dz} = \frac{dr}{dt} \frac{dt}{dz}$  where  $\frac{dr}{dt} = -c(1+z)$  and  $\frac{dt}{dz}$  is the Friedmann equation rearranged (since  $\dot{R} = -\frac{1}{(1+z)^2} \frac{dz}{dt}$ ) so have  $\frac{dt}{dz} = \int \frac{dz}{H(z)}$ . For a flat Universe with no curvature we have  $H(z) = H_0[\Omega_M(1+z)^3 + \Omega_\Lambda]^{1/2}$  which leads to

$$D_L = \frac{c(1+z)}{H_0} \int_0^1 [(1+z)^3 \Omega_M + \Omega_\Lambda]^{-1/2} dz. \quad (\text{B.9})$$

Fig. A.1 shows the variation of the distance estimate for a matter-dominated, and a  $\Lambda$ -dominated flat Universe. For increasing redshift the later is larger than the former as expected due to  $\Lambda$ 's repulsive effect.

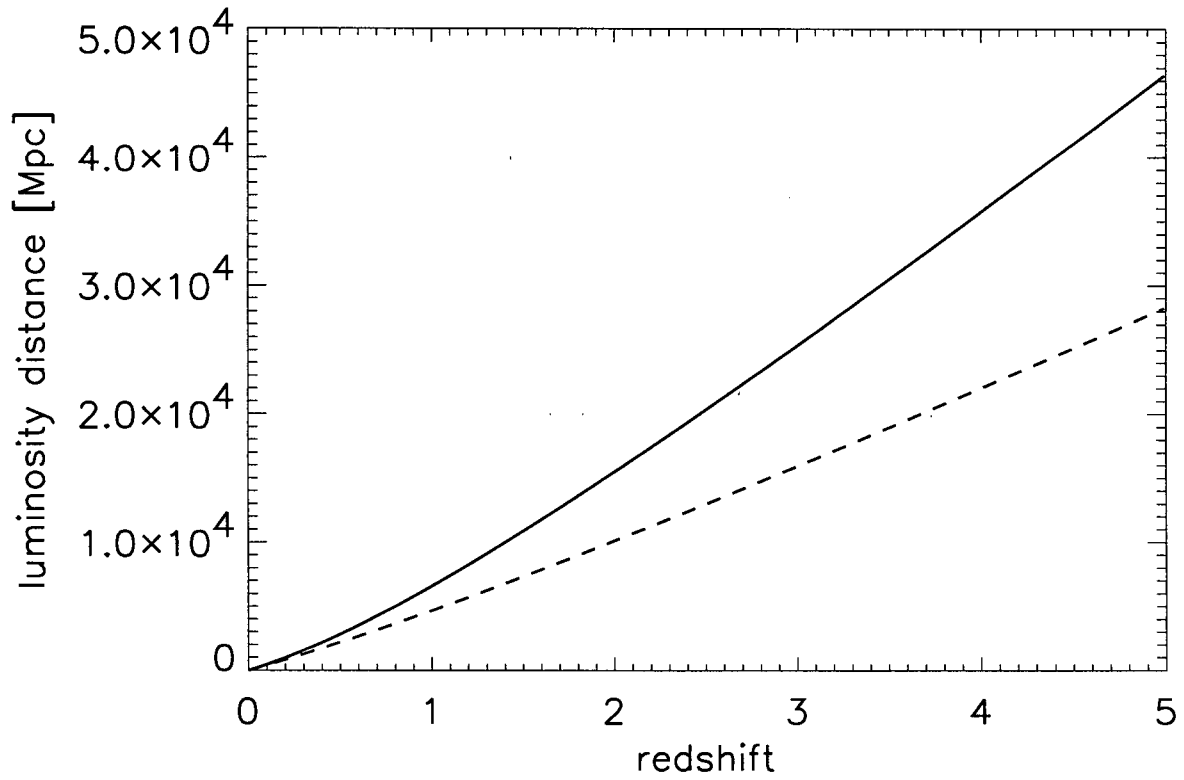


Figure B.1: The effects of different cosmological models on the luminosity distance estimation. In terms of  $[\Omega_{\text{tot}}, \Omega_{\Lambda}, \Omega_{\text{M}}]$ , the solid line is  $[1, 0.7, 0.3]$ , while the dashed line is  $[1, 0, 1]$ . Here  $H_0 = 75 \text{ km s}^{-1} \text{ Mpc}^{-1}$ .

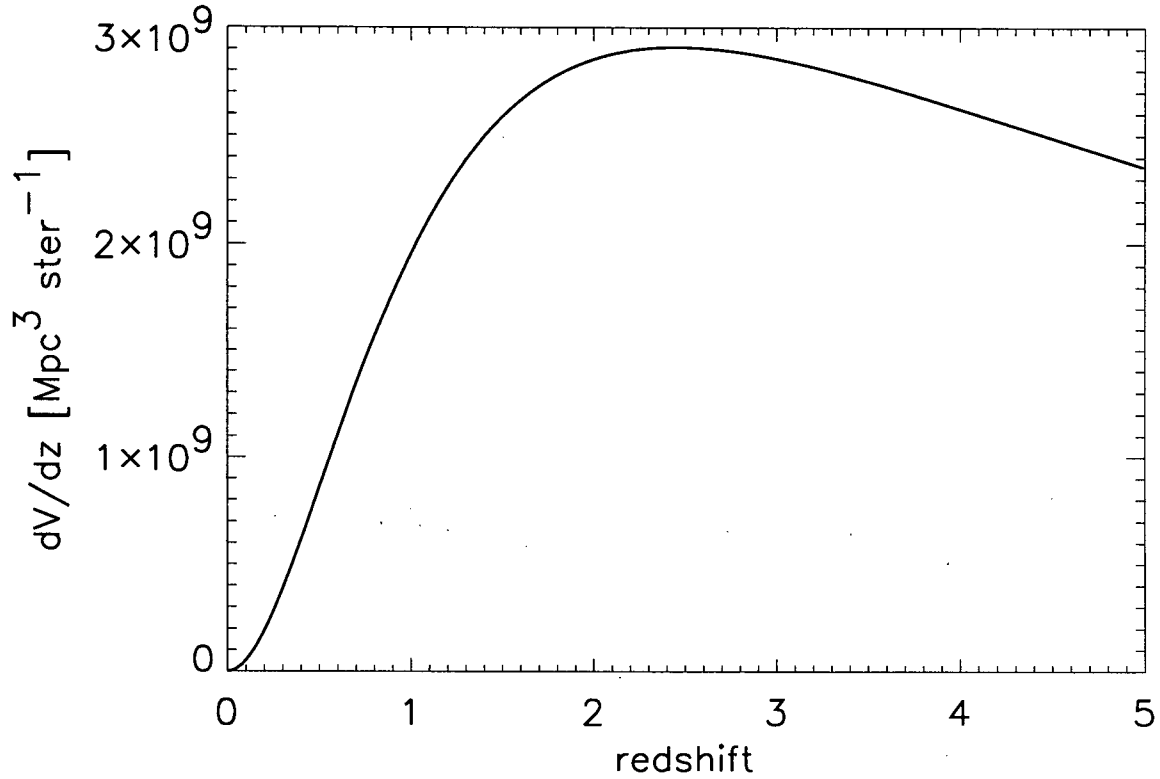


Figure B.2: The volume element.

The other quantity of interest here is the differential volume element  $\frac{dV}{dz}$  per unit solid angle<sup>2</sup>  $d\Omega$ , which represents the volume sampled in the shell  $z$  to  $z + dz$ . Since we only consider the simpler case of a flat Universe, it is essentially (over the whole sphere)  $\frac{dV}{dz} = \frac{4\pi}{3} \frac{d}{dz}(D_M^3) dz$  where  $D_M$  is the proper radial distance. It is related to the luminosity distance as  $D_L = D_M(1+z)$ . In terms of the later (and per unit solid angle), the volume element turns out to be:

$$\frac{dV}{dz d\Omega} = \frac{c}{H_0} \frac{D_L^2}{(1+z)^2 \sqrt{(1+z)^3 \Omega_M + \Omega_\Lambda}} \quad (\text{B.10})$$

<sup>2</sup>The total number of square degrees in a sphere is given by  $4\pi(\frac{180}{\pi})^2 = 41,253$ .